January 2012

Low Loss VHF and UHF Filters for Wireless Communications Based on Piezoelectrically-Transduced Micromechanical Resonators

Julio Mario Dewdney
University of South Florida, jdewdney@mail.usf.edu

Low Loss VHF and UHF Filters for Wireless Communications Based on Piezoelectrically-Transduced Micromechanical Resonators

by

Julio Mario Dewdney Montero

A dissertation submitted in partial fulfillment
of the requirements for the degree of
Doctor of Philosophy
Department of Electrical Engineering
College of Engineering
University of South Florida

Major Professor: Jing Wang, Ph.D.
Thomas M. Weller, Ph.D.
Andrew Hoff, Ph.D.
Xiaomei Jiang, Ph.D.
Craig Lusk, Ph.D.

Date of Approval:
July 31, 2012

Keywords: Bandwidth, Insertion Loss, MEMS,
Piezoelectric, Quality Factor

Dedication

To my Mother Mercedes Montero, my Father Delroy Dewdney and my brothers Delroy,

Andres and at least but not last to my fiancé Issa Ramirez

Acknowledgments

I like to express my gratitude to my Parents, Mercedes Montero and Delroy Dewdney, who have given me everything that a son may wish: *Love, Education and Support*. They have been my inspiration, strength and the role model all my life. I hope someday to be as good as them. I am what I am thanks to them.

I am especially grateful for the moral support received from my brothers, Andres Eduardo and Pepe. They are constantly in my mind and my heart providing me with the motivation to become a better person.

I want to state my appreciation to my major professor Dr. Jing Wang, for its academic guidance and support in making me a better scholar and professional in my field. Special thanks are given to my close friends and colleagues Dr. Cesar Morales and I-Tsang Wu, who help me in many aspects of my work. This work would not have been possible without them. I have enjoyed working with them for the past years, and hopefully our destiny may cross again in the future. I also want to thanks to Tianpeng Wu, Kosol Son, Paula Algarin, Jose Carballo and Vinicio Carias. They have always provided me a helping hand during the moments of need.

I would also like to extend my gratitude to the staff at the NREC, who organizes the micro-fabrication facility. I want specially thank to Rich Everly, who continuously provide to cleanroom users with his help and technical support. I cannot imagine the NREC without him. Especial thanks to Robert Tufts, for lead and organize the NREC. He

is and always was the true NREC director, despite that somebody usurped his position for a while.

Special thanks are given to Michael Konrad who has provided to the RF-MEMS group countless technical support. He along with Rich Everly, are so far the best engineers that I have met.

Last but definitely not least, I thank my fiancé, Issa Ramirez. She is the reason why I smile every day. I owe her for every bit of success and happiness that I have had from the moment that she came into my life. She is the most important motivation for me to move forward and to be a better person each day passes by.

Table of Contents

List of Tables

List of Figures

Abstract

For the past decade, a great deal of research has been focused towards developing a viable on-chip solution to replace the current state-of-the-art VHF and UHF filters based on SAW and FBAR technologies. Although filters based on SAW and FBAR devices are capable of fulfilling the basic requirements needed for IF and RF bandpass filtering and reference signal generation, an alternative solution that can enable the next generation of multi-frequency and multi-mode transceivers while enabling size and price reduction by allowing the manufacturing of single-chip monolithic RF transceivers is highly desired. In response to these new needs, piezoelectrically-transduced micromechanical filters have emerged as a plausible alternative to outperform current dominant technologies in size, cost, and IC manufacturing compatibility without compromising device performance in terms of insertion loss, rejection, power handling and linearity.

This dissertation presents the design, fabrication, characterization and experimental analysis of low-loss VHF and UHF filters for wireless communication applications, based on piezoelectrically-transduced micromechanical resonators. The resonators employed in this work for the implementation of microwave filters, resonate in contour-mode shapes, which differ from commercially available thickness-mode FBAR resonators, for which the thickness sets the resonance frequency. The employment of contour-mode designs facilitate simultaneous synthesis of multiple frequencies on the same substrate through CAD layout-defined lateral dimensions, thus avoiding the

complexity demanded by FBAR devices for the precise control of the piezoelectric layer thickness. Moreover, filters composed of acoustically-coupled piezoelectrically-transduced resonators operating at higher order modes with sizes up to 10 times smaller than their SAW counterparts operating at the same UHF range have been successfully implemented, without jeopardizing the key filter specifications.

Throughout this dissertation, piezoelectrically-transduced MEMS filters based on mechanically, electrically and acoustically coupled contour-mode resonator(s) or resonator arrays were designed and fabricated. Filters with insertion loss as low as 2.6 dB at IF frequencies and 4.0 dB at RF frequencies have been demonstrated. Moreover, synthesized filters with extremely narrow bandwidth of 0.1 % and 0.2 % at frequencies between 160 MHz and 215 MHz have been developed, which comply the specifications for IF filters for GSM handsets. This particular type of filters each consist of just one single high-*Q* resonator, which leverages single crystalline silicon as the major part of their structure to obtain the sufficient quality factor required for the implementation of such small bandwidth.

Among the most significant results, this dissertation presents two thin film piezoelectrically-transduced monolithic filters operating at 482 MHz and 536 MHz, which can be interfaced directly to a 377 Ω antenna without the need of external matching components. This dissertation also has conducted a systematic comparison between commercial available SAW filters and the MEMS filters synthesized using piezoelectrically-transduced resonators. Parameters such as group delay and third intermodulation (IP3) have been measured and carefully compared. Evidentially, most of

the fabricated piezoelectrically-transduced filters developed by this work have exhibited a similar or superior performance as compared to their commercial SAW counterparts.

Chapter 1

Introduction

1.1 Overview

Since the first long wireless transmission in 1895 by Guglielmo Marconi, wireless communications have become one of the areas that have revolutionized the form that human beings interact and changed forever the way that contemporary society communicate. Today, wireless communication enables a wide variety of applications such as satellite transmission, radio and television broadcasting, sensor networks, global positioning system (GPS), mobile communications, and a lot more of emerging applications that have led to a new generation of multifunctional, small size and low cost communications devices that cover a wide variety of wireless communications applications.

As the demand for these emerging multifunctional wireless communications devices increases, so does the demand for smaller, low cost and single-chip oscillators, mixers and RF front-end and intermediate frequency (IF) filters that can bring together in a single device multiple wireless standards operating at different frequencies, without compromising size, portability and cost. Currently, the majority of the modern transceiver systems are based on heterodyne architecture, which utilizes a number of discrete resonant components such as quartz crystals, SAW (Surface Acoustic Wave) and FBAR (Thin Film Bulk Acoustic Resonator) devices to implement oscillators with high quality factors (*Q's*) for frequency reference and band-pass filtering.

Despite the beneficial high-*Q* offered by quartz crystal and SAW devices, and the low motional resistance provided by FBAR's, they are relatively bulky off-chip components that must be integrated with electronics at the board level, thus hindering the ultimate miniaturization and portability of wireless transceivers. Very promising alternatives to overcome the aforementioned issues have been demonstrated by on-chip micromechanical resonators with electrostatic and piezoelectric transduction mechanisms along with small size, high quality factor (*Q*'s >10,000) and low insertion loss. Nevertheless, there is still room for improvement, further reduction of the motional resistance to allow matching to 50 Ω electronics, while retaining simple IC-compatible and mass-producible manufacturing process.

1.2 Modern Wireless Transceiver Architecture

A transceiver is a wireless device that consists of both a transmitter and a receiver sharing electronic circuitry for transmission and reception of radio frequency signals. The main function of the transmitter is to modulate and up-convert the baseband data to a carrier frequency to achieve high transmission efficiency with a reasonably sized antenna. The transmitter also provides the power amplification needed for the transmission in the medium, which for a wireless system is the free space. The receiver amplifies, filters, and down-converts the incoming signal to a lower frequency and demodulates it in the presence of undesired interference and noise. One of the most popular receiver configurations is the super-heterodyne architecture, which has been used in the majority of wireless system since its invention by Edwin Armstrong in 1917. A simplified schematic of a modern communication transceiver is shown in Figure 1.1. In general, the function blocks of the receiver and the transmitter can divide into three main tasks:

frequency generation, amplification and spectral shaping. The first two, have been successfully implemented with integrated circuit (IC) technologies, whereas the spectral shaping still demands off-chip mechanically vibrating components such quartz crystals, surface acoustic wave (SAW) and bulk acoustic wave (BAW) devices. Although oscillators and filters implemented with such technologies outperform their counterparts implemented using conventional transistor technologies in terms of insertion loss, percent bandwidth, achievable out-of band rejection, and dynamic range; they are bulky off-chip components that need to be interfaced with IC electronics at the board level, thus hindering the miniaturization of the transceiver size.

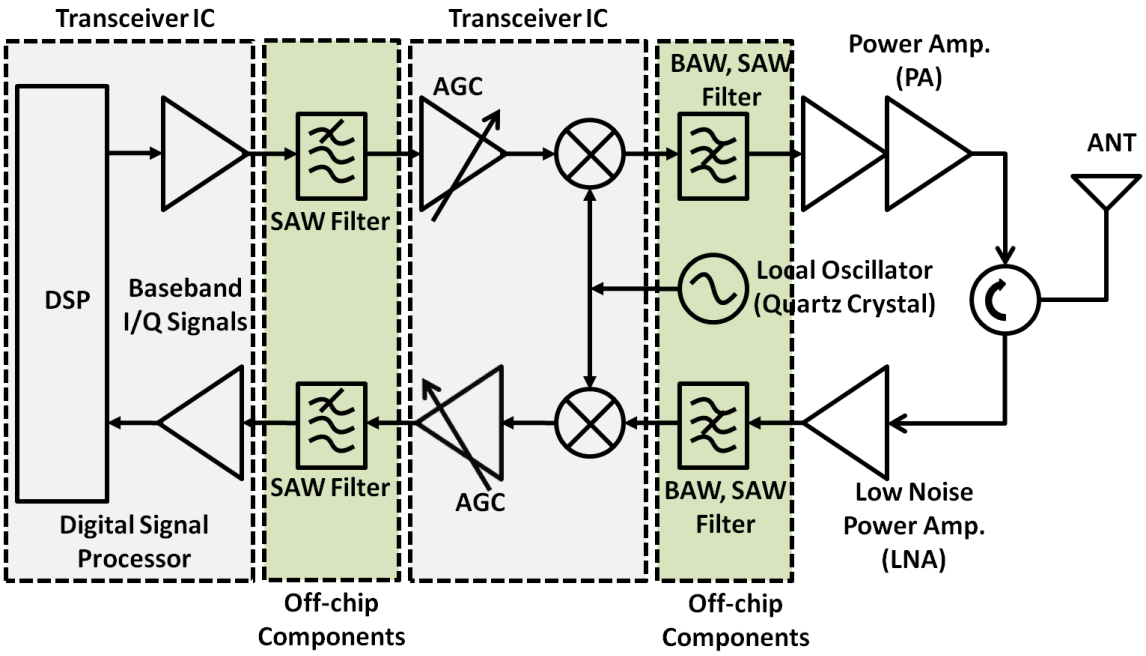

Figure 1.1 – Block diagram for a typical super-heterodyne transceiver

Although super-heterodyne transceiver architectures fulfill all the requirement for current wireless communication systems, (e.g., cellular phones, tablets, monitoring systems, bluetooth devices, etc) efforts have been focused on developing alternative

transceiver architectures such as direct conversion [2], low-IF [3], and RF sampling down-conversion [4]. While these alternatives that decrease the number of off-chip components have shown some level of success [5], they trade the performance of discrete passive devices for on-chip active devices, which increase the power consumption and complexity of the transceiver.

1.3 Transceiver Architecture Based on RF-MEMS

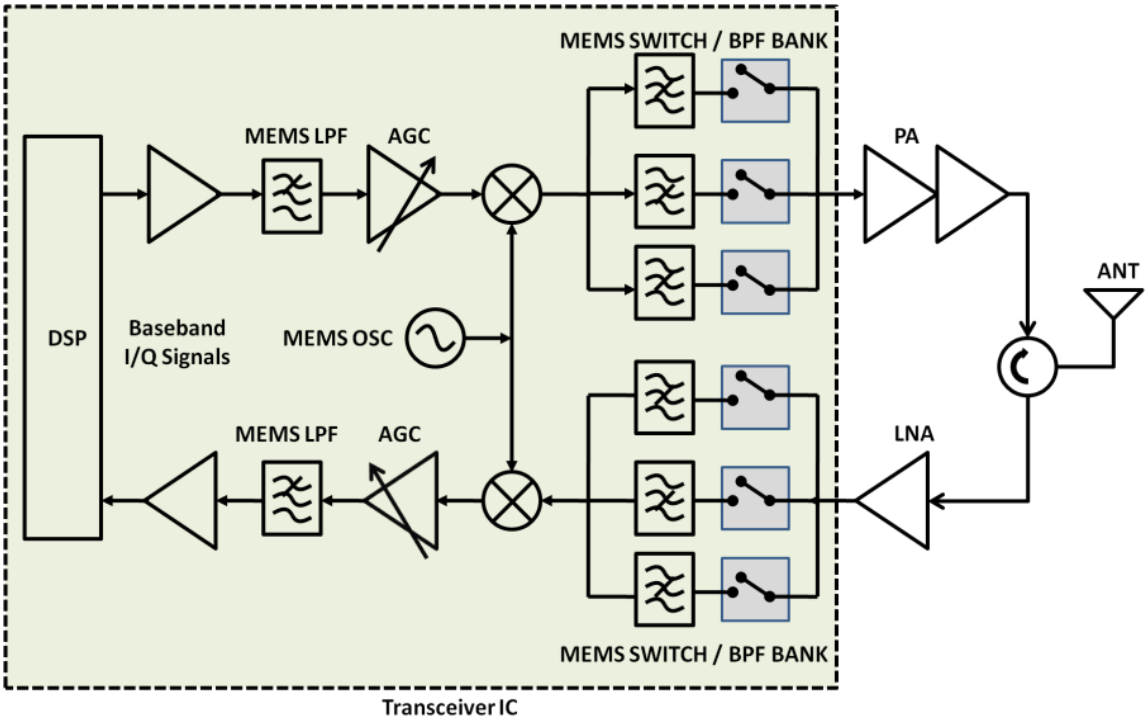

Figure 1.2 – Simplified architecture of RF-MEMS resonator-based channel select transceiver

One of the most extensively pursued topics of RFIC designers is the miniaturization of communication electronic devices, while improving performance, reducing size, power consumption and weight, and moreover, minimizing the fabrication cost. Consequently, a technology that can fulfill all these coveted requirements is highly desirable. Recent advances of CMOS-compatible micro-electro-mechanical-systems

(MEMS) technology have made possible the fabrication of on-chip RF-MEMS components, such as intergraded inductors, tunable capacitors, RF-MEMS switches [6], and more recently voltage controlled oscillators (VCO) based on capacitively-transduced micromechanical resonators [7][8]. The transceiver architecture presented in Figure 1.2 is a clear example of how MEMS technology can be integrated into monolithic integrated circuits, by replacing all the external passive components, such as SAW and BAW filters, and the quartz crystals oscillators. Besides the obvious size and power consumption reduction, new transceivers architectures based on RF-MEMS technologies can enable a new generation of reconfigurable multi-band telecommunication systems, in which one single transceiver IC can cover several services operating over a wide frequency range, therefore eliminating the need for multiple transceivers when additional functionalities and services are required.

1.4 Current State of the Art of Micromechanical Resonators and Filters

The concept of Microelectromechanical resonator was first introduced by Harvey C. Nathanson in 1965, through the implementation of the resonant gate transistor as a frequency selective device [1]. Although such a pioneering device was constructed through a batch fabrication method similar to present-day MEMS manufacturing, it was not until the 1980's when the advancement in materials and microfabrication technologies rekindled the interest in micromechanical resonant structures. Since then, several types of microresonators have been successfully demonstrated operating as the building blocks for frequency reference oscillators and filters.

1.4.1 Previous Work on Capacitively-Transduced Resonators

With the advances in the polysilicon surface micromachining technology, the initial effort of micromechanical resonant structures was initially led by R.T Howe at UC Berkley [10]. Howe conceived a capacitively actuated resonant polysilicon microbridge for vapor sensing applications. Following this research, William C. Tang [11] and Clark Nguyen [12] popularized the electrostatic comb-drive resonator for signal processing in the medium-frequency range (i.e., 300 kHz to 3 MHz), through the implementation of micromechanical band-pass filters, exhibiting insertion loss as small as 0.1 dB at 340 KHz [13]. To increase the operational frequency of these micromechanical resonators to the high-frequency range (i.e., 3 to 30 MHz) and very high frequency range (i.e., 30 to 300 MHz), flexural-mode free-free-beam polysilicon resonators were demonstrated operating at frequencies from 30 MHz to 100 MHz with quality factors as high as 8,400 in vacuum [14]. Bandpass filters composed of mechanically-coupled free-free beam resonators were also implemented [15] with a center frequency of 37 MHz and an insertion loss less than 4 dB at of 1.7% as shown in Figure 1.3.

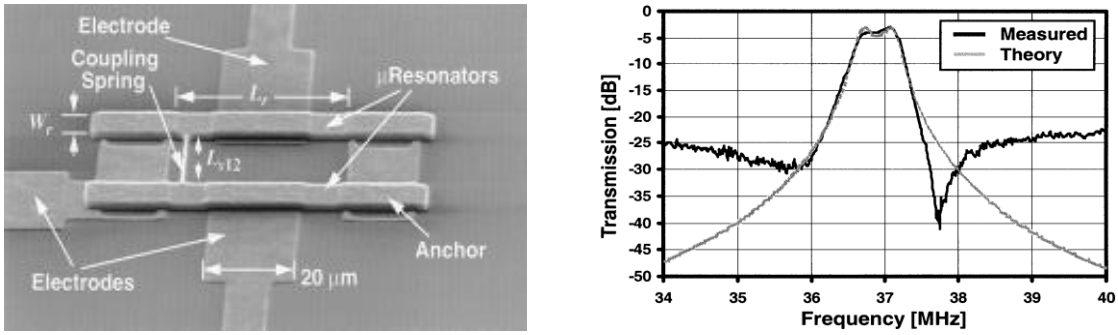

(a) (b)

Figure 1.3 – (a) SEM micrograph of a 37 MHz mechanically-coupled free-free beam micromechanical filter; (b) Its frequency characteristic measured under 50 μTorr of pressure along with the theoretical prediction. (From A. Wong *et al.* [15] © IEEE 2000)

Although the performance of the free-free beam resonators is attractive for the implementation of bandpass filters in the low MHz range, they are not well-suited for applications in the ultra-high frequency (UHF) range (i.e., 300 MHz to 3 GHz) as excessive scale-down of the device geometry approach the actual tolerance of MEMS fabrication process. Even if such scale down were feasible with current fabrications techniques, it would introduce several problems such as mass loading and low device quality factor. As a promising approach to circumvent these issues, John R. Clark *et al.* [16] implemented a lateral vibrating micromechanical contour-mode disk resonator to obtain higher resonance frequencies, as shown in Figure 1.4. As opposed to the free-free beam resonators, the electrostatic force acts laterally on the resonating disk, producing expansion and contraction of the structure along its radius. Using this design, devices operating at 156 MHz with *Q*'s exceeding 9,400 were demonstrated, with dimensions significantly larger as compared to those of free-free beam resonators, which is better suited for operation at the UFH range [16].

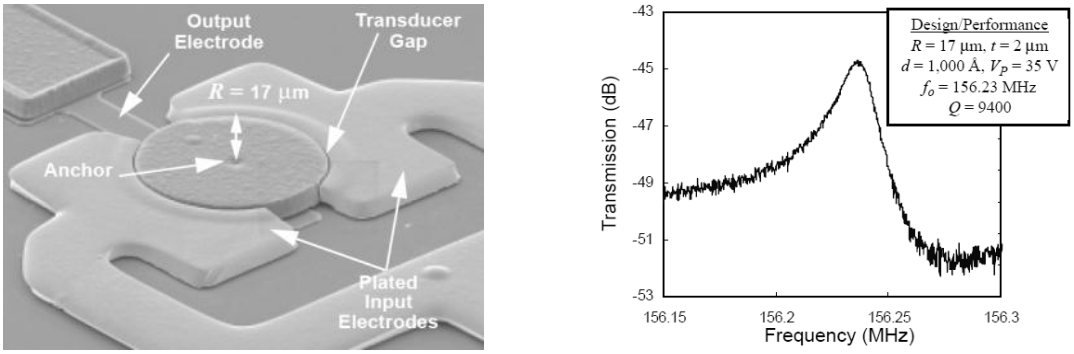

(a) (b)

Figure 1.4 – (a) SEM micrograph of a 17 μm-radius micromechanical contour-mode disk resonator; (b) and the frequency response at its fundamental resonance mode (From Clark *et al.* [16] © IEEE 2000)

Wang *et al.* [17] implemented a self-aligned fabrication technique to develop a radial-contour mode micromechanical disk resonator with resonant frequencies up to 1.156 GHz and measured *Q*'s at this frequency close to 3,000 in both vacuum and air [17]. The major breakthrough of this design can be ascribed to the self-alignment of the supporting anchors to the exact center of the resonator, thus allowing excitation of the higher order modes. This novel design allows high quality factors at gigahertz frequencies while retaining similar dimensions and power handling ability on par with the previous version of the contour-mode disk resonator. Other extensional mode devices, such as wine-glass mode disk resonators [18] and hollow-disk resonators [19] were also implemented. The wine-glass disk resonator operating at 74 MHz exhibited high *Q*'s of 98,000 in vacuum and 8,600 in air, while the hollow-disk resonator with 1.2 GHz resonance frequency achieved a *Q*-factor exceeding 10,000.

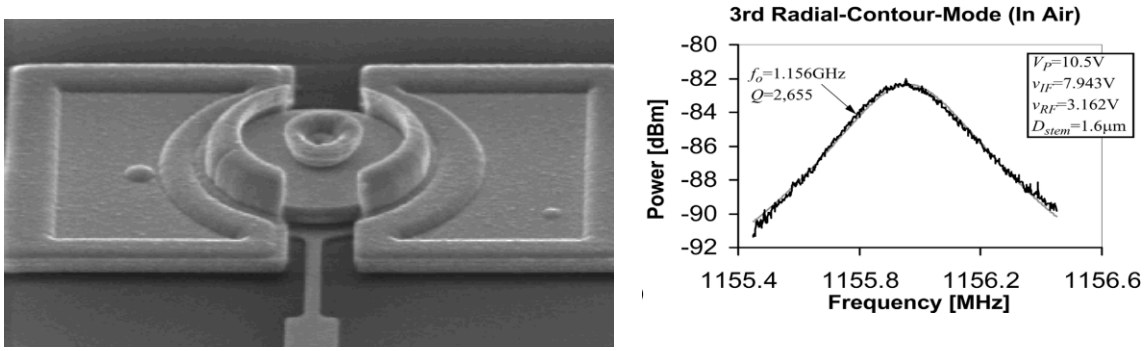

(a) (b)

Figure 1.5 – (a) SEM micrograph of the stem self-aligned, radial-contour-mode disk resonator; (b) Frequency characteristics for a 1.156 GHz, 3rd radial-contour mode, 20 μm diameter, disk resonator measured in air. (From Wang *et al.* [17] © IEEE 2004)

Despite the high *Q* and wide frequency range achieved by radial contour disk resonators, their large motional resistance (> 1 MΩ) is too high to match with the standard 50 Ω impedance of today's RF components. Several strategies have been proposed such as replacing the capacitive air gap by a solid gap filled with a high-k dielectric or reducing the air gap to sub-100 nm range. Capacitively-transduced resonators with sub-100 nm air gaps and with solid high-k dielectric gaps have achieved VHF and UHF frequencies with quality factors as high as 20,000 in air and motional impedances less than 10 kΩ [21][22][23].

Aside from the efforts for increasing the operational frequency of capacitively transduced micromechanical resonators, research towards lowering the motional impedance of such devices was also in progress. Demirci *et al.* implemented a novel technique using a parallel array of corner coupled square plate resonators for reduction of the effective motional impedance [20].Using this technique with several corner-coupled resonators, an effective motional resistance of 480 Ω has been demonstrated at 70 MHz, which is 5.9 times smaller than that exhibited by a stand-alone single square resonator.

In 2009, Weinstein *et al.* [24] investigated the electrostatic transduction of a longitudinal-mode silicon acoustic resonator with internal dielectric films. With this configuration, a dielectrically-transduced silicon bar-shaped resonator with a 15 nm nitride solid gap has been demonstrated with the highest resonance frequency of 6.2 GHz and quality factor of 4,277 as shown in Figure 1.6. A frequency-*Q* product of 3.1×10^{13} at 4.7 GHz is the highest in polysilicon resonators reported to date [14]. However, the motional impedance is not improved with this design and also the quality factor is lower as compared to devices operating with air gaps.

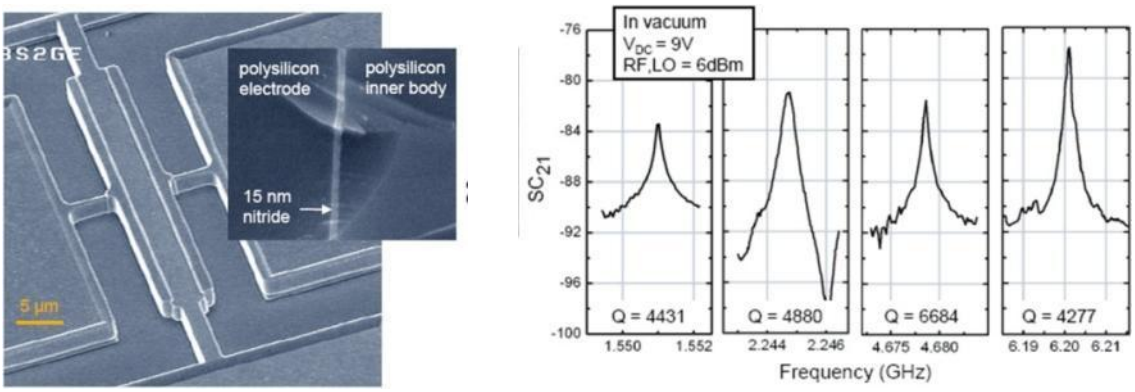

(a) (b)

Figure 1.6 – (a) SEM micrograph of a bulk-mode resonator dielectrically-transduced resonator; (b) Frequency response at different resonant frequencies (From Weinstein *et al.* [24] © IEEE 2009)

1.4.2 Previous Work on Piezoelectrically-Transduced Resonators

Piezoelectric transduction offers orders of magnitude higher coupling coefficients than capacitive transducers for similar resonator geometry. Therefore, the low motional impedance enabled by the more efficient electromechanical transduction makes piezoelectric resonators the dominant technology in the current mobile communication market. On the contrary to capacitive devices, in which any conductive material can be used as device layer (e.g., Polysilicon, Silicon, Diamond, Nickel, etc.), piezoelectric devices rely on the piezoelectric effect that only exists in piezoelectric materials. Common materials for MEMS piezoelectric resonators are quartz, Zinc Oxide (ZnO), Aluminum Nitride (AlN), Barium Titanate and Lead-Zirconate-Titanate (PZT).

Currently, the two most important classes of piezoelectric resonators are the Surface Acoustic Wave (SAW) and the Bulk Acoustic Wave (BAW). SAW resonators are widely employed to implement filters at frequencies lower than 2 GHz. However, for wireless communications standards that require frequencies higher than 2 GHz, it becomes very difficult to implement low-loss and sharp-cut off filters using SAW

technology. The quality factor for a SAW resonator decreases at higher frequencies and the size of the electrodes start to approach sub-micron scale, thus forcing the employment of nonstandard photolithography fabrication techniques (i.e., electron-beam lithography).

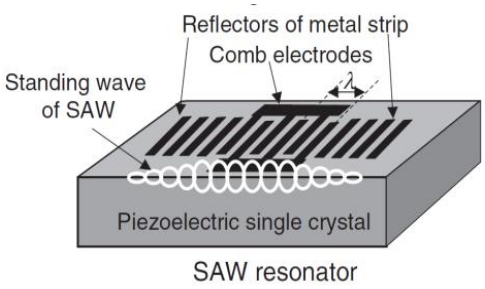

Figure 1.7 – Schematic of a typical SAW resonator

Filters based on BAW resonators have attracted attention since its introduction by Lakin *et al.* [25], due its simple electrode design, higher quality factor, sharp cut-off shape, high frequency range and moreover the possibility of implementing monolithic filters alongside of active RF components (i.e., amplifiers, mixers, etc). At the moment, two main variants of BAW filters have been successful commercialized on the wireless market: Thin film bulk acoustic resonator also known as FBAR [26] in which the resonant structure isolated from the carrier substrate via air cavity suspension and solid mounted resonators or SMR which use Bragg's acoustic reflectors as isolation from the carrier substrate [27].

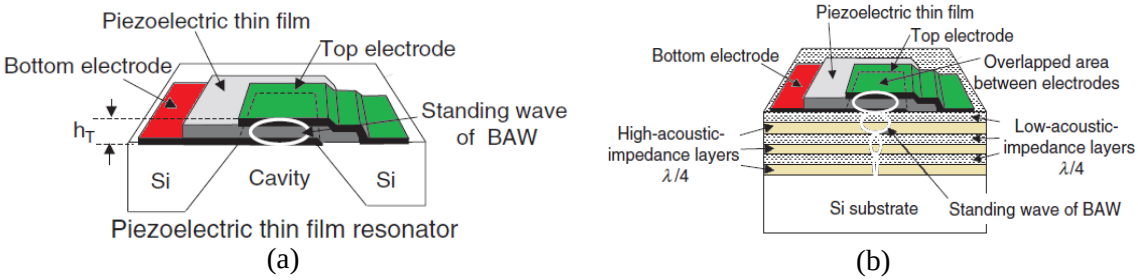

Figure 1.8 – Device implementation for the two types of bulk acoustic wave (BAW) resonators with two different types of acoustic isolation methods: (a) Film bulk acoustic resonator (FBAR) sits on top of air cavity; and (b) solid mounted resonator (SMR) employs Bragg's reflector

Despite the current dominance of FBAR devices in the RF filter market, they suffer from a major limitation as their resonance frequency is set by the thickness of the piezoelectric film. Therefore, in order to achieve precise frequencies, the thickness of the piezoelectric film must be accurately controlled. Moreover, only devices operating at one specific frequency can be fabricated in one process run. Nevertheless, the present-day wireless technology calls for multi-functional single-chip transceivers that operate at different frequencies as opposed to several discrete components integrated on board level. In order to solve this problem, Piazza *et al.* [28] proposed a feasible solution to expand the major advantage of FBAR (i.e., low motional resistance, high-*Q*, and high resonance frequency) to a single chip implementation of multiple frequencies using piezoelectrically transduced contour-mode aluminum nitride (AlN) micromechanical resonators. The resonance frequency for the contour-mode resonator is determined by the lithography-defined lateral dimensions, rather than the thickness of the piezoelectric layer. AlN resonators with resonance frequencies from 23 MHz to 230 MHz with quality factors up to 4,300 in air and low motional impedance (50~700 Ω) have been demonstrated [28]. These devices have been electrically cascaded in ladder configuration to yield high performance, low insertion loss (as low as 4 dB at 93 MHz), and large rejection (27 dB out of band rejection for a 236 MHz micromechanical band pass filter [29][30] as shown in Figure 1.9.

Abdolvand *et al.* [31] introduced a new generation of piezoelectric resonators called thin-film piezoelectric-on-substrate (TPoS) resonators. These devices benefit from the high electromechanical coupling of piezoelectric transduction, and the superior acoustic properties of a low acoustic loss substrate such as single crystal silicon.

Therefore, the motional impedance of these resonators is significantly smaller as compared to typical capacitively-transduced counterparts while they exhibit relatively high quality factor at atmospheric pressure. The TPoS resonator has been utilized to fabricate multi-frequency UHF filters within a single substrate. Using the same technology, thickness-mode filters have also been demonstrated at frequencies ranging from 600 MHz to 3.5 GHz with motional resistance less than 700 Ω [32][33].

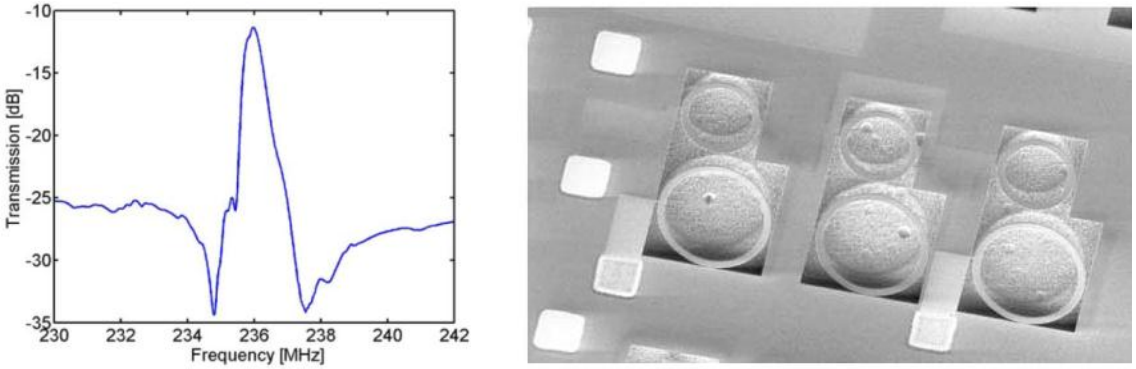

Figure 1.9 – Frequency response and SEM micrograph of a 236 MHz ladder filter realized using different size rings in the series and shunt branches. (From Piazza *et al.*[30] © IEEE 2007)

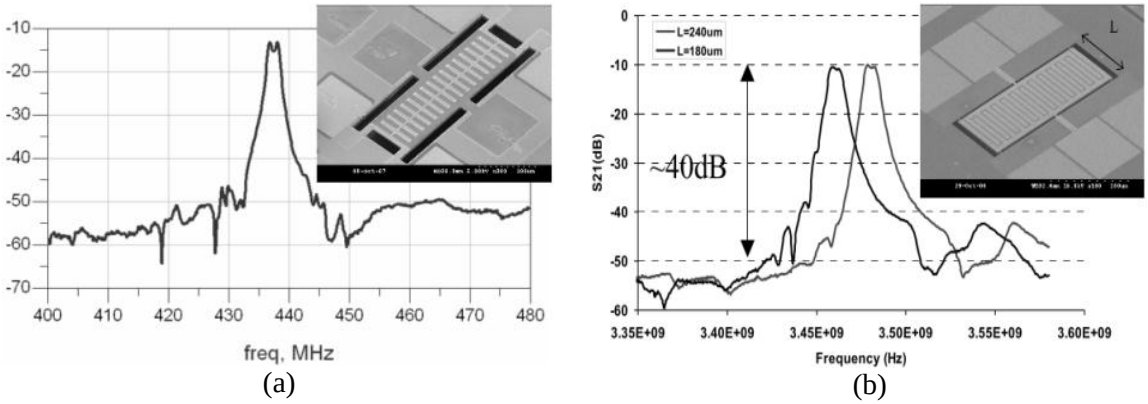

Figure 1.10 – (a) Electrical response and SEM micrograph of a 435 MHz of lateral monolithic filter; (b) Measured frequency response plots and the SEM micrograph of 3.5 GHz thickness mode monolithic TPoS filters. (Abdolvand *et. al.* [32] © Cambridge University 2009)

1.5 Summary of Issues for the Current State of the Art in Resonator Technologies

Capacitively-transduced resonators and filters based on radial contour-mode disk resonators have been demonstrated with the ability to achieve high quality factors and resonance frequencies. Unfortunately, these devices usually suffer from high insertion loss if terminated with 50 Ω due its high motional impedance. Even though capacitively transduced resonators with sub-100 nm air gaps have been demonstrated at VHF range with high quality factors and relatively low motional impedances (i.e., 1 kΩ), reliable and high yield fabrication of these devices with sub-100 nm air gaps is still challenging. Otherwise, capacitively-transduced resonators with solid gaps have been demonstrated with the highest resonance frequency of 6.2 GHz in a silicon resonator, their motional impedance is still quite higher than 50Ω (i.e., >1 MΩ) and their quality factors are lower as compared to the devices implemented with air gaps.

FBAR and SAW technologies have already reached a phase of maturity, as they have been produced in large volumes through industrial manufacturing processes for more than one decade. Less performance demanding applications such as RF front-end duplexers are the preferred target of such technologies. Filters based on contour-mode AlN resonators have been demonstrated at UHF frequencies. These electrically-coupled (ladder) filters exhibited moderate insertion loss and quality factors. However, their performance still relies highly on the mechanical and electrical properties of the piezoelectric layer.

1.6 Dissertation Organization

This dissertation is organized into six chapters. The first chapter presents an overview of the current state of the art of micromechanical resonators and filters

technologies and describes the goals of this dissertation research. Chapter 2 reviews the fundamentals and basic formulations for piezoelectric materials. Additionally, the equivalent mechanical and electrical lumped circuit representation for piezoelectric resonators and filters are also described.

The fabrication processes for the piezoelectric resonators and filters implemented in this work are detailed in Chapter 3. The experimental results obtained for the novel contour mode resonators and bandpass filters developed in this research are presented in chapter 4. Chapter 5 presents a study of the effect of the substrate in the performance of the fabricated piezoelectric filters and resonators as well as the experimental results of three different coupling schemes used to implement low loss micromechanical filters based on piezoelectrically-transduced resonators operating in the VHF and UHF bands.

Chapter 6 summarized the accomplishments of this work and the viable directions for future research work.

1.7 Contributions

The main contribution from this dissertation work is the successful design and implementation of low loss piezoelectric micromechanical filters for VHF and UHF applications. The fabricated MEMS filters have greatly reduced sizes up to 10 times smaller than the commercial devices implemented with SAW resonators operating at the same frequency range.

Thin-film piezoelectrically-transduced and piezo-on-silicon resonators were developed to construct higher-order micromechanical filters via capacitive, mechanical and acoustic coupling schemes. The MEMS filters investigated in this work are mainly composed of contour-mode micromechanical resonators whose resonance frequencies are

determined by their lateral dimensions defined by CAD layout. In other terms, filters operating at multiple different frequencies can jointly fabricated on the same substrate with strategically designed device lateral dimensions, without the need of thickness alternation and post-processing trimming which is one of the costly but necessary processing steps for film bulk acoustic resonators (FBAR) operating in thickness-mode.

In this work, the implementation of filters based on arrays of mechanically-coupled piezoelectrically-transduced resonators to lower the filter termination impedance has also been investigated. A two-pole filter based on a 10×2 array of micromechanically-coupled resonators has been demonstrated with a center frequency of 73 MHz. Given its lower characteristic motional impedance achieved via the arraying technique, this filter has shown a satisfactory insertion loss of 5 dB when it is terminated with a 300 Ω resistor. This type of filters use arrays of mechanically-coupled resonators as two individual composite resonators to provide two key advantages such as the reduction of the filter termination impedance and improvement of power handling capabilities, without sacrificing the device performance in terms of insertion loss and out-of-band rejection.

In order to raise the operational frequencies of micromechanical filters to meet the required RF front-end frequencies of the present-day wireless systems, piezoelectrically-transduced plate resonators vibrating in higher order length-extensional modes have been adopted for the synthesis of UHF micromechanical filters. Among the most significant results, this dissertation presets two thin film piezoelectrically-transduced monolithic filters operating at 482 MHz and 536 MHz, which can be interfaced directly to an

antenna with a 377 Ω of characteristic impedance, without the need of external impedance-matching components.

Another achievement of this dissertation is the successfully implementation of single-resonator filters that use two distinctive contour-mode resonances of a single structure instead of two separate resonators to define the filter passband frequency characteristics. This design, which is also known as monolithic filter, reduces the number of resonators required to implement a filter, thus leading to a simpler and compact design. Furthermore, the use of a material such as single crystalline silicon with low acoustic loss as the major part of the resonator body in such filters, allows the implementation of two-pole filters with a bandwidth as narrow as 200 kHz with an insertion loss of 8 dB, which fulfill the requirements for GSM/EDGE applications at frequencies close to 200 MHz. In addition, it was also demonstrated that the inclusion of silicon as the major part of structural material, not only improves the linearity of the piezoelectrically-transduced filters in terms of third-order intermodulation products, but also significantly increases the quality factors of piezoelectrically-transduced resonators.

In addition, a robust and high-yield microfabrication process for thin-film ZnO and ZnO-on-SOI resonators and filters have been successfully developed. The process is entirely compatible with standard CMOS foundry processing with a low thermal budget with temperature well under 400ºC, which facilitates future monolithic integration between MEMS filters and CMOS electronics on the same substrate to fulfill single chip transceivers.

Chapter 2

Background

2.1 Piezoelectric Effect

The piezoelectric effect is understood as the linear electromechanical interaction between the mechanical and the electrical state in crystalline materials with no inversion symmetry [35]. A piezoelectric material is able to generate an electrical charge when a mechanical stress (force) is applied. The amount of charge generated is directly proportional to the strength of the applied mechanical stress. This behavior is known as direct piezoelectric effect. Piezoelectricity is also a reversible and bidirectional energy conversion mechanism, where mechanical deformation is generated in a piezoelectric material when an electrical field is applied. This is behavior is known as reverse piezoelectric effect.

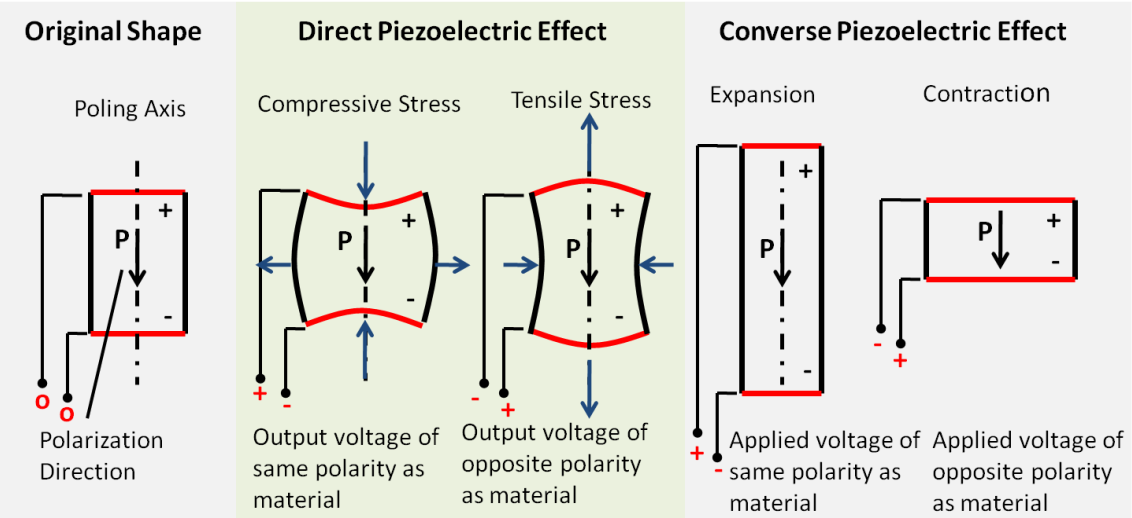

Figure 2.1 – Illustration of the direct and reverse piezoelectric effects

Since the discovery of piezoelectricity in 1880 by the brothers Pierre Curie and Jacques Curie, the first step towards an engineering application was taken in 1916 by Paul Langevin, who constructed an ultrasonic sensor for submarine detection using a piezoelectric quartz element. This first practical application started the experimentation of the mechanically vibrating crystal and its piezoelectric behavior, leading to the invention of timing and frequency control devices using quartz crystals. Since then, several engineering applications based on the piezoelectric effect have been widely implemented, such as microphones, sensors, transducers and frequency control devices such as oscillators, the latest became the milestone for the continuously growing radio-telecommunication industry.

2.2 Piezoelectric Materials

Piezoelectric materials can be divided in two major categories, piezoelectric crystals and piezoelectric ceramics. Only few of the single crystals are actually used as piezoelectric elements. Quartz, a natural piezoelectric crystal, is widely used because of its mechanical strength, small dielectric loss, chemically stability and low thermal coefficient expansion, which translates to an excellent dimensional stability under temperature variations. However, its piezoelectric effect is relatively weak as compared to other piezoelectric ceramic materials. Therefore, quartz is used mainly in piezoelectric filters, timing and frequency reference devices such as oscillators, which do not require a high piezoelectric effect.

Although there are several ceramic materials that exhibit piezoelectric behavior, the most widely used in transducers and MEMS applications are Aluminum nitride (AlN), Zinc oxide (ZnO), Barium titanate ($BaTiO_3$) and Lead-Zirconate-Titanate (PZT).

Barium titanate is an excellent material for electromechanical transducers because of its high electromechanical coupling coefficient and ease of fabrication. However, two major drawbacks have limited its further development: high thermal expansion coefficient and low Curie point. Contrarily, PZT has rapidly taken the places of barium titanate in most of piezoelectric applications due to its high electromechanical coupling factor, and low thermal expansion coefficient. PZT ceramics are ferroelectric and do not require a specific deposition processing in order to obtain high piezoelectric coefficients.

AlN and ZnO are the most used piezoelectric thin film material for MEMS applications. High quality AlN and ZnO films can be obtained by sputtering at a relatively low temperature (below 400 °C) offering compatibility with CMOS processing. The low processing temperatures of these materials also enables post-CMOS integration process while retaining aluminum as the metallization layer. However, these materials are not ferroelectric. Consequently, in order to obtain high piezoelectric coefficients, particular deposition conditions are required.

Table 2.1 – Properties of most common piezoelectric materials [35][36][37]

Material	Density (kg/m^3)	Dielectric Constant	Acoustic Velocity [m/s]	Piezoelectric Coefficient d_{31} [pC/N]	Temperature Expansion Coefficient
Quartz	2650	3.8-4.5	3158	2	0.6×10^{-6}/°C
BaTiO3	6020	1500	4800	33.4	0.5×10^{-6}/°C
PZT	7600	400 – 1000	3300	180	-6.0×10^{-6}/°C
ALN	3270	8	11400	1.8	4.5×10^{-6}/°C
ZnO	5766	8.8	6330	4.7	4.0×10^{-6}/°C

2.3 Mathematical Model of the Piezoelectric Effect

As mentioned in the last section, the charge generated in a piezoelectric material is directly proportional to the strength of the applied mechanical stress. Since piezoelectric materials are anisotropic, their physical properties (e.g., permittivity, elasticity, and piezoelectricity coefficients) are vector quantities. The electrical behavior of a piezoelectric material can be expressed as:

$$D_{3x1} = \varepsilon_{3x3} E_{3x1} \tag{2.1}$$

where D is the electric density displacement, ε is the dielectric constant and E represents the electric field. Equivalently, the mechanical behavior of piezoelectric materials is modeled using the Hooke's law which describes the stress-strain relationship of material which is given by:

$$S_{6x1} = c_{6x6} T_{6x1} \tag{2.2}$$

where S represents the strain, c is the compliance, and T is the stress. These Equations can be combined into a coupled equation, which relate the mechanical and electrical variables and completely described the behavior of piezoelectric materials. The fundamental electro-mechanical coupled equation is given by:

$$T_{6x1} = c_{6x6} \cdot S_{6x1} - e_{6x3} \cdot E_{3x1} \tag{2.3}$$

$$D_{3x1} = e_{3x6} \cdot S_{6x1} - \varepsilon_{3x3} \cdot E_{3x1} \tag{2.4}$$

where e represents the piezoelectric constants. These sets of equations are known as the stress-charge form of the piezoelectric equations or d-form piezoelectric equations.

2.4 Piezoelectrically-Transduced MEMS Resonator

A piezoelectrically transduced MEMS resonator consists of a piezoelectric substrate suspended from the edge and embedded between two thin film metal electrodes, which are patterned on the two major surfaces of the substrate as shown in Figure 2.2.

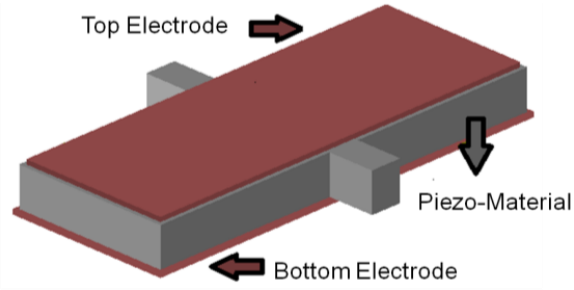

Figure 2.2 – Schematic-view diagram of a piezoelectric square-plate resonator

An alternative design known as piezoelectric-on-substrate resonator is shown in Figure 2.3. A piezoelectric-on-substrate resonator consists of a thin-film piezoelectric layer embedded between two metallic electrodes stacked on top of a relatively thick mechanical structural layer. The structural layer which usually comprises a large portion of the resonant structure is chosen from a low acoustic loss material such as single crystal silicon. For both designs, when an AC electric field is applied across the piezoelectric film between the top and bottom electrodes at the natural resonance frequency of the structure, the device is excited into its resonance mode. The applied electrical field across the piezo-film will drive the resonator body to expand and contract through the reverse piezoelectric effect. In return, the resonance mode deformation induces periodic piezoelectric charges on the surface of the output electrodes.

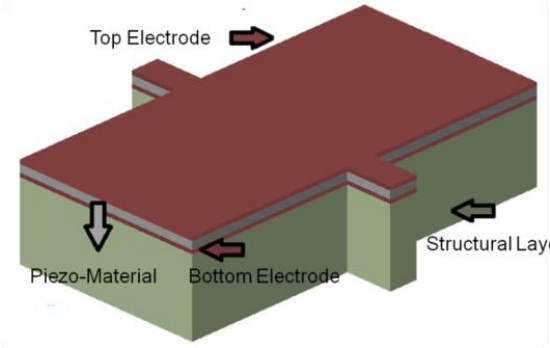

Figure 2.3 – Piezoelectric on substrate resonator

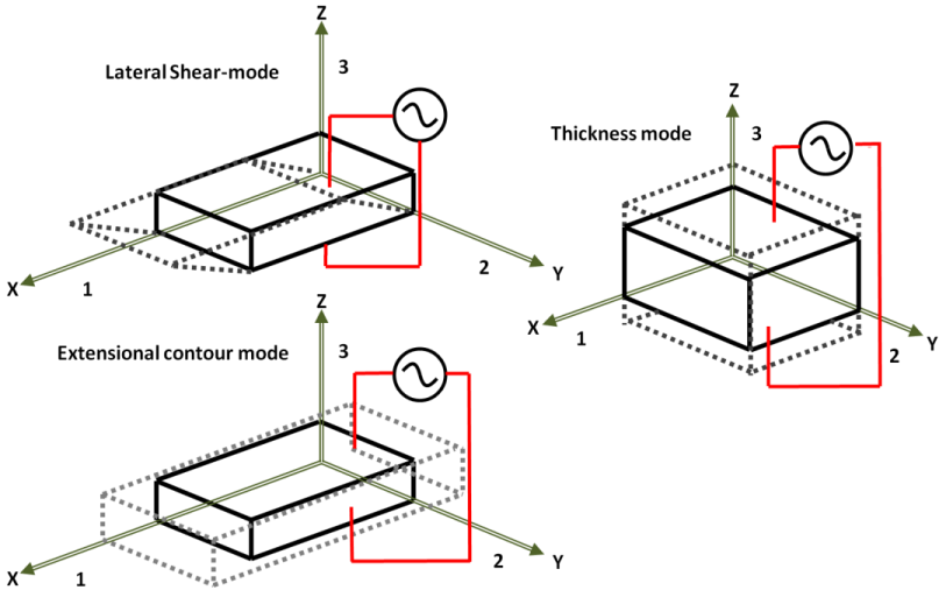

Figure 2.4 – Vibration modes of a piezoelectric rectangular plate resonator [40]

Depending on how the plate is polarized to excite the resonance and the geometrical dimensions that set its resonance frequency, a device with a square-plate shape can be either actuated in thickness-mode (by means of d_{33} piezoelectric coefficient), lateral shear-mode (by means of d_{15} piezoelectric coefficient) or contour-mode (by means of d_{31} piezoelectric coefficient). Thickness-mode is employed in FBAR resonators, which the resonance frequency is set by the thickness of the piezoelectric

transducer material, preventing multiple frequency operation on a single substrate. For devices operating in shear-modes, the electrical field must be applied perpendicular to edges of the plate in order to drive the structure in resonance, thus complicating the fabrication process. Moreover, as in the case of thickness-mode, the fundamental resonance frequency is set by the film thickness, therefore allowing one operation frequency on a single substrate. Lastly, the resonance frequency in a plate vibrating in a contour-mode shape is set by the lateral dimension of the structure. Such dimensions can be precisely defined by the device CAD layout, facilitating the design and fabrication of this kind of structures. Figure 2.4 illustrates the vibration modes for piezoelectric resonators mention above.

2.5 Contour-Modes in Rectangular Plates

For a plate with the length of l and width of w, resonating in its extensional contour-mode along the length of the bar as shown in Figure 2.5, the resonance frequency can be calculated from the analysis of a set of differential equations knows as the wave equations [42], which describe the modal vibration of the resonator. It is worthwhile mentioning that this example is taken for its simplicity, but the analysis can be extended to different geometries and mode shapes. A more detailed analysis of several shapes and modes is presented by R. A. Johnson *et al.* [42]. The analysis for structure in question starts with the wave equation given by:

$$\frac{E}{\rho}\frac{\partial^2 u}{\partial x^2} = -\omega^2 u \tag{2.5}$$

where E is the Young's modulus, ρ is the density of the structural material and u is the displacement.

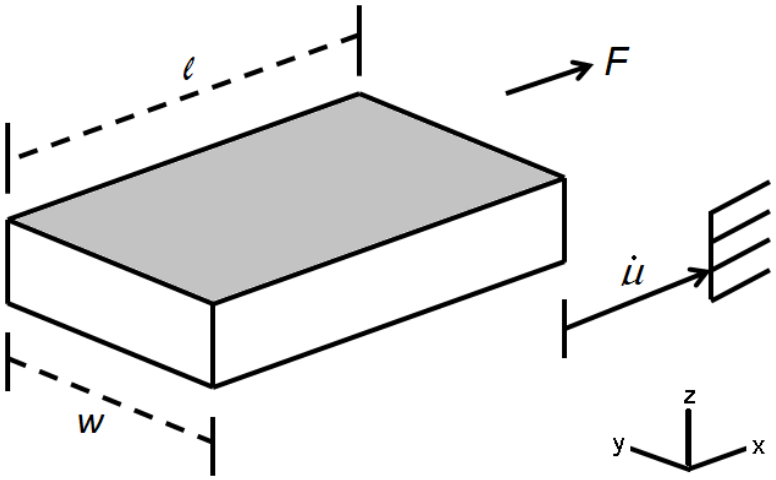

Figure 2.5 – Longitudinal-mode rectangular plate resonator

Equation (2.5) can be solved using the theory of liner differential equations. The general solution is expressed as follows:

$$u(x) = A \sin kx + B \cos kx \tag{2.6}$$

where x is the distance from the end of the plate, and k is the propagation constant. By differentiating Equation (2.6) while applying the boundary condition $x = 0$, the value of A can be found as:

$$\frac{\partial u}{\partial x}\Big]_{x=l}^{x=0} = Ak \cos kx - Bk \cos kx = 0 \tag{2.7}$$

At $x = 0$; since $\sin kx = 0$,

$$Ak \cos kx - 0 = 0, \text{ or } A = 0 \tag{2.8}$$

$$u(x) = B \cos kx \tag{2.9}$$

Applying the boundary condition at $x = l$ to Equation (2.7), this results in:

$$\sin kl = 0, \text{ for } k_n l = n\pi, n = 1,2,3, \ldots\ldots \tag{2.10}$$

Now by substituting Equation (2.9) in the wave Equation (2.5) and differentiating the left hand side. After cancelling the $\cos kx$ term in the equation, we obtain:

$$k = \omega\sqrt{\frac{\rho}{E}} \tag{2.11}$$

Next we substitute the values of k_n from Equation (2.10) into Equation (2.11) that derive the governing expression for the resonance frequency of a rectangular plate vibrating along its length in the nth mode:

$$f_n = \frac{n}{2l}\sqrt{\frac{E}{\rho}} \tag{2.12}$$

As example, Figure 2.6 shows the first length-extensional mode for a thin-film ZnO plate resonator with dimesions of 140 µm x 40 µm. the resonance frequency for this resonator is 15.43 MHz, which can be calculated analytically using Equation (2.12).

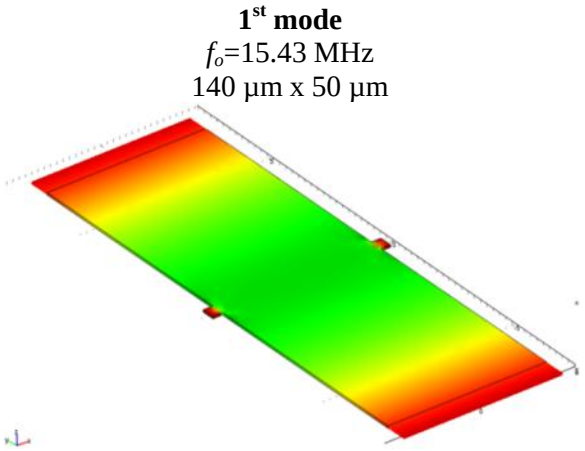

Figure 2.6 – COMSOL simulation of a longitudinal-mode ZnO rectangular plate resonator operating in the 1st length-extensional mode

2.6 Mechanical Resonator Modeling

The mechanical behavior of a resonator at the resonance frequency depends on the inertia, elastic compliance of the resonator body, and the energy dissipation. Similarly, the electrical behavior of the resonator can be described by an equivalent electrical

circuit, consisting of an inductor, capacitor and resistor connected in series, corresponding respectively to the inertia, compliance and damping of the mechanical system. Regardless of the resonator shape (e.g., beam, disk, ring, plate, etc.) and the transduction mechanism (i.e., electrostatic, piezoelectric) the aforementioned mechanical and electrical equivalent circuit models are always applicable. Table 2.2 summarizes the analogy between the mechanical and electrical domain, where mechanical parameters such as force and velocity are equivalent to corresponding electrical variables such as voltage and current.

Table 2.2 – Direct analogy between electrical and mechanical domain

Mechanical Domain		↔	**Electrical Domain**	
Force	F	↔	Voltage	V
Velocity	$\dot{u}$	↔	Current	I
Mass	M_{eq}	↔	Inductance	L_m
Compliance	$1/K_{eq}$	↔	Capacitance	C_m
Damping	C_{eq}	↔	Resistance	R_m

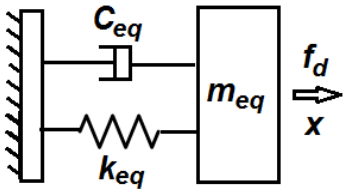

(a)

(b)

Figure 2.7 – Equivalent lumped-element model of a micromechanical resonator. (a) Equivalent mass-spring-damper model; (b) Equivalent LCR circuit model

The lumped-element mechanical model representation of a micromechanical resonator is shown in Figure 2.7(a). Where k_{eq},m_{eq} and C_{eq}, represents its equivalent stiffness, mass and damping, respectively. Although this mechanical model describes the mechanical behavior of the resonator, an electrical model is most appropriate for electronic filter design and frequency reference devices. Figure 2.7(b) presents the electrical equivalent circuit model based on the electromechanical analogy shown in Table 2.2. This equivalent electrical circuit consists of a series LCR tank, two transformers, and a port capacitance at the input and output terminals. The transformers in the model represent the input and output transducers, which can be either piezoelectric or capacitive.

2.7 Model Parameters for Equivalent Electrical Circuit

The equivalent electromechanical parameters of a resonator can be extracted with the use of the fundamental equations of piezoelectricity and rigid body dynamics. A second approach is based on an energy method that relates the electrical and mechanical domains [28]. For the case of a rectangular piezoelectric plate vibrating along its length the electrical parameters can be calculated by:

$$M_{eq} = \frac{\rho l w T}{2} = \frac{M_{static}}{2} \tag{2.13}$$

$$C_{eq} = \frac{\omega_n M_{eq}}{Q} \tag{2.14}$$

$$K_{eq} = \omega_n^2 M_{eq} \tag{2.15}$$

where w, l and T are the width, length and thickness of the resonator body, Q is the quality factor, ω_n is the frequency for the nth resonance mode. Subsequently, the electromechanical coupling factor can be determined as follows:

$$\eta = \frac{Q_T}{u_{max}} \tag{2.16}$$

where Q_T is the total charge induced on the electrodes and u_{max} is the maximum displacement. Now we can convert these mechanical variables into electrical parameters using the electromechanical analogy presented in Table 2.2 as follows:

$$R_m = \frac{C_{eq}}{\eta^2} \tag{2.17}$$

$$C_m = \frac{\eta^2}{k_{eq}} \tag{2.18}$$

$$L_m = \frac{M_{eq}}{\eta^2} \tag{2.19}$$

2.8 Mechanical Filters Fundamentals

A mechanical filter is a signal processing device constructed of mechanical components (i.e., resonators) instead of the typical electrical components (i.e., resistors, inductors and capacitors) used in electronic filters. Its purpose is the same as that of an electronic filter: to pass signals with frequencies within a certain range that is called the passband while blocking and attenuating signals outside the targeted passband. A mechanical filter leverages its highly frequency selective modal vibration to process the signals in the mechanical domain. The transducers at the input and output terminals of the filter convert the electrical input signal into mechanical modal vibration and then transform the mechanical vibration to an electrical output signal.

A symbolic representation (block diagram) of a single input and single output filter is shown in Figure 2.8, where $x(t)$ is the input signal, and $y(t)$ is the output signal. The behavior of a filter can be expressed as:

$$H(s) = \frac{Y(s)}{X(s)} \tag{2.20}$$

The quantities $X(s)$ and $Y(s)$ are the Laplace transformations of $x(t)$ and $y(t)$ respectively, and $H(s)$ is the transfer function, which is the ratio between the transmitted output and delivered input signals in the frequency domain.

Figure 2.8 – Block diagram of a filter with one input and one output

2.9 Bandpass Filter Specifications

Several different types of filters can be found in wireless communication systems. Based on their frequency transmission characteristics, they are generally classified as lowpass, highpass, bandpass, and stopband filters. However, in the majority of modern communication systems, the primary need is for band pass filters.

Figure 2.9(a) shows the frequency response of an ideal bandpass filter. This filter has a linear phase response in its passband, no attenuation for the signals in the passband and complete rejection for out of the band signals. Unfortunately, this ideal filter characteristic cannot be realized with a finite number of elements, and therefore the behavior of a real bandpass filter is specified by a set of specifications on its frequency transmission characteristic in the pass-band and stop-band as shown in Figure 2.9(b).

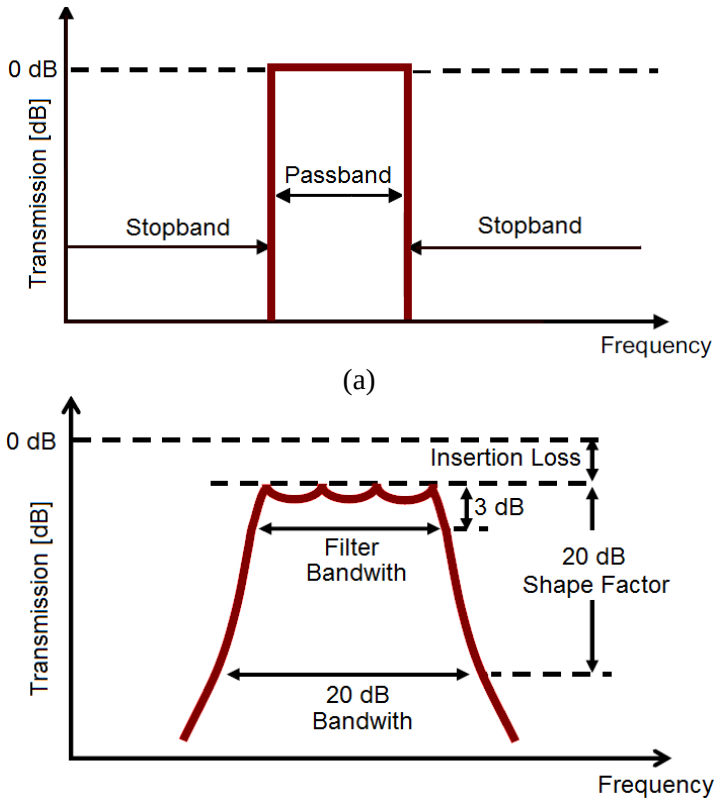

Figure 2.9 – (a) Ideal band-pass filter response; (b) Specification of a real filter

The insertion loss (IL) is a key figure of merit for a filter, which represents the loss of signal power within the filter passband measured in decibel level. The filter bandwidth (BW) is defined as the set of frequencies between the half power points or at 3 dB attenuation from the minimum loss point in the passband. The frequency at the center of the passband is defined as the center frequency (f_c). In general, the quality factor (Q) is defined as the ratio between energy stored in the system to the energy dissipated per cycle. For the case of the filter, the quality factor can be expressed as the ratio between the center frequency and the bandwidth.

$$Q = \frac{f_c}{BW} \tag{2.21}$$

The shape factor at a certain level of attenuation is defined as the ratio of the frequency span at that attenuation to the 3 dB bandwidth as shown in Figure 2.9(b). For instance, a 20 dB shape factor is given by the ratio between the 20 dB bandwidth and 3 dB bandwidth:

$$SF = \frac{\text{20 dB Bandwith}}{\text{3 dB Bandwidth}} \tag{2.22}$$

Chapter 3

Fabrication Technology

There is a rapidly increasing demand for MEMS technology as the RF field embarks on a new generation of microsystems capable of direct monolithic integration with CMOS circuitry on the same substrate. Applications include RF switch arrays, phase shifters, impedance tuners, micromechanical filters and oscillators, among others. Currently, the majority of the MEMS devices available on the market still use a hybrid approach for the integration of MEMS devices and CMOS circuitry. Such hybrid modular approach increases the manufacturing cost, and ultimately delays the maturity and widespread commercialization of MEMS technologies on the market. One promising alternative approach to accomplish a low-cost integration of MEMS and CMOS electronics is to start with a conventional CMOS foundry process followed by the fabrication of MEMS devices alongside or even directly on top of CMOS IC's through a compatible process. This approach is known as Post-CMOS integration. Since CMOS circuitry can be designed and processed at any commercial foundry without compromising the cost, reliability and repeatability, the Post-CMOS integration is more advantageous as compared to Pre-CMOS, Intra-CMOS and hybrid integration strategies.

One of the major advantages of piezoelectrically-transduced micromechanical resonators is their potential to be monolithically integrated with CMOS circuits through post-CMOS processes. The major challenge of Post-CMOS integration of these devices is that the process temperature for the deposition of the piezoelectric materials has to be

kept below 400 °C under the constraint of the allowable thermal budget of CMOS circuitry. Some piezoelectric materials, such as Lead Zirconate Titanate (PZT), suffer from compatibility issues with the state of the art CMOS foundry processes. On the contrary, Zinc Oxide (ZnO) and Aluminum Nitride (AlN) that have been widely used in the past decade for FBAR and SAW devices, hold great promise for mass production through CMOS-compatible processing steps. Moreover, reproducible sputtering deposition of these materials is commercially available, allowing the fabrication of piezoelectric devices on silicon or silicon-on-insulator (SOI) substrates using surface micromachining techniques compatible with Post-CMOS integration.

In this chapter the fabrication process employed to manufacture the piezoelectrically-transduced resonators and filters of this work is presented. Two main fabrication processes are presented in detail. The first correspond to the process employed in the fabrication of resonators and filters which employ ZnO film as both piezoelectric transducer and resonant structure. The second process describes the modified ZnO-on-SOI fabrication process, where silicon is used as the major part of the resonant structure, and ZnO film is used as the piezoelectric transducer.

3.1 Piezoelectric Material Selection

In this work the suitable selection for piezoelectric film was made after considering device performance, available tools and ease of processing in the Nanotechnology and Research Education Center (NREC) at the University of South Florida. Three materials were initially considered: ZnO, PZT, and AlN. Among those three, PZT provides the highest transverse piezoelectric coefficient (d_{31}), but it also has the highest acoustic losses. Otherwise, AlN has the highest acoustic velocity among the

three and also exhibits relatively low acoustic losses. However, it requires Cl_2-based reactive ion etching, a process rarely found in R&D labs or even IC foundries, to pattern the AlN layer to define the shape of the resonator body. Another potential problem with AlN is the low deposition rate using conventional RF-magnetron sputtering. Deposition rates obtained in several performed experiments did not exceed 30 nm/hr at the maximum RF power provided by the sputtering system in our lab. This low deposition rate translates to an exceedingly long deposition process for the piezo film thickness needed in the present work (i.e., 500 – 800 nm).

Despite its moderate acoustic velocity and electrical resistivity, ZnO was selected mostly for its ease of processing. Deposition rates in range of 100 nm/hr and available CH_4/Ar dry etching recipe through deep reactive ion etching (DRIE) process were the most convenient reasons for selection of this material. Table 3.1 summarizes the most important properties of the three piezoelectric materials that have been considered.

Table 3.1 – Properties of piezoelectric materials

Material Properties		**ZnO** [35]	**PZT** [36]	**AlN** [36]
Density [kg/m^3]	ρ	5676	7600	3260
Elastic Modulus [GPA]	E	123	53	330
Acoustic Velocity [m/s]	ϑ	6630	3300	10400
Poisson Ratio	μ	0.18 − 0.36	0.25 − 0.31	~0.24
Piezoelectric Strain Coefficient [pC/N]	d_{31}	-4.7	-130	-1.8
Relative Permittivity	ε_r	9 − 11	400 − 1900	8 − 10
Electrical Resistivity [Ω·cm]	ρ_e	$10^8 - 10^9$	$10^7 - 10^9$	$10^{10} - 10^{14}$

3.2 ZnO Characterization

The quality of the ZnO film is critical for obtaining a high transverse piezoelectric coefficient (d_{31}). There is a strong correlation between the degree of c-axis orientation and the value of d_{31} piezoelectric coefficient. Given that the contour-mode resonators

vibrate with in-plane motions through orthogonally applied electrical field through the piezoelectric transducer layer, highly c-axis orientated ZnO films are desirable for the piezoelectrically-transduced contour-mode resonators and filters fabricated in the present work. For this reason, a systematic study examining the quality of the ZnO films as a function of deposition conditions was performed. Several ZnO films were deposited at different oxygen concentrations and substrate temperatures. The quality of the films was examined by x-ray diffraction (XRD). For all these samples, the target-to-substrate distance was held constant and the RF power was kept at 100 W.

3.2.1 Oxygen Concentration

Several other research groups [44][45] have found that extra oxygen is needed as a reactant gas in the sputtering chamber during ZnO deposition. The presence of extra oxygen is required to compensate for the depletion of oxygen in the ZnO film. The ZnO molecule will dissociate after leaving the sputtering target thus creating free zinc and oxygen atoms. Occasionally, the free Zn atoms will not recombine with oxygen before reaching and incorporating into the film leaving excess of Zn in the film, thus lowering the quality of the film.

We studied the effects of four different argon-to-oxygen gas flow ratios including 20%, 30%, 50%, and 70%. The rest of deposition parameters were retained for each of the films. The temperature was set to 300 °C, the chamber pressure was set to 5 mTorr and the RF power was held to 100 W. Figure 3.1 shows the XRD spectra for the ZnO films grown with different oxygen concentrations. All of them exhibit (002) orientation, though the film deposited at 50% oxygen shows the highest intensity peak implying that

this process condition lead to the better c-axis orientation as compared with the other conditions.

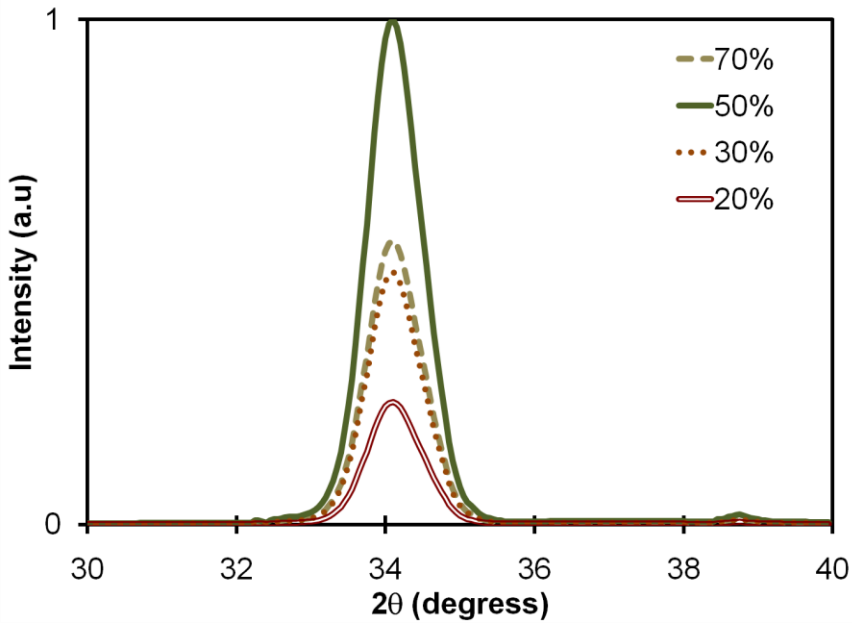

Figure 3.1 – XRD curves for ZnO samples deposited at different oxygen concentrations

3.2.2 Substrate Temperature

The substrate temperature plays an important role in determining the quality of the sputtering deposited ZnO films. Figure 3.2 presents XRD spectra for ZnO films deposited at a variety of substrate temperatures ranging from room temperature to 300 °C. The films deposited at 300 °C exhibited (002) peak intensity higher than ones deposited at lower temperatures. At even higher temperatures, the intensity decreases gradually but remains within the same order of magnitude.

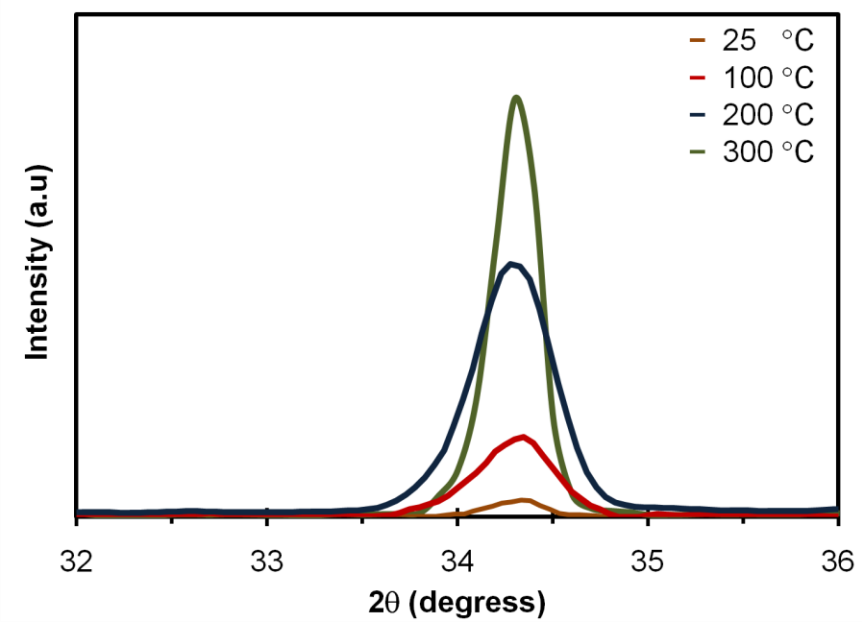

Figure 3.2 – XRD curves for ZnO samples deposited at different substrate temperatures

3.3 Fabrication Process for Thin Film Piezoelectric ZnO Resonators and Filters

Figure 3.3 shows the cross-sectional process flow for ZnO piezoelectric resonators that concurrently employs the ZnO film as both piezoelectric transducer and resonator body. A four mask low temperature process (T_{max} < 400 °C) process has been used to fabricate thin film piezoelectric ZnO resonators and filters. The fabrication process starts by depositing a thin (~50 nm) ZnO buffer layer on high resistivity silicon wafer to provide an electrical isolation to decrease the feedthrough parasitic through the substrate. The fabrication process is followed by patterning the platinum (Pt) bottom electrode by lift-off. It is worth mentioning that Molybdenum (Mo) was initially chosen due its low acoustic loss and high acoustic velocity. Moreover, it is also a suitable seed layer for deposition of piezoelectric materials such as ZnO and AlN. However, Molybdenum has two major drawbacks. Mo can be easily oxidized at relatively low temperature in an oxygen environment, and its conductivity is lower than other metals

such as gold, aluminum and platinum. Provided ZnO thin films are deposited by reactive RF sputtering using oxygen and argon, therefore molybdenum was not a good choice. Additionally, the dry release process by fluorine chemistry (SF_6) also attacks molybdenum.

For the aforementioned reasons, molybdenum was dismissed as the material for both bottom and top electrodes. Instead, platinum and aluminum have been selected as the bottom and top electrode. Platinum is a noble metal that can withstand high annealing temperatures up to 800 °C, would not easily oxidize in oxygen environment and could endure the dry release process with fluorine chemistry. Thus, Pt is a desirable candidate for the bottom electrode. Similarly, Aluminum is an attractive choice for the top electrode since it has a relatively low acoustic attenuation coefficient and it is also able to survive the dry release process. However, Platinum was later on utilized for both top and bottom electrodes as aluminum top electrode tend to introduce residual stress to cause the released resonator structure to buckle up.

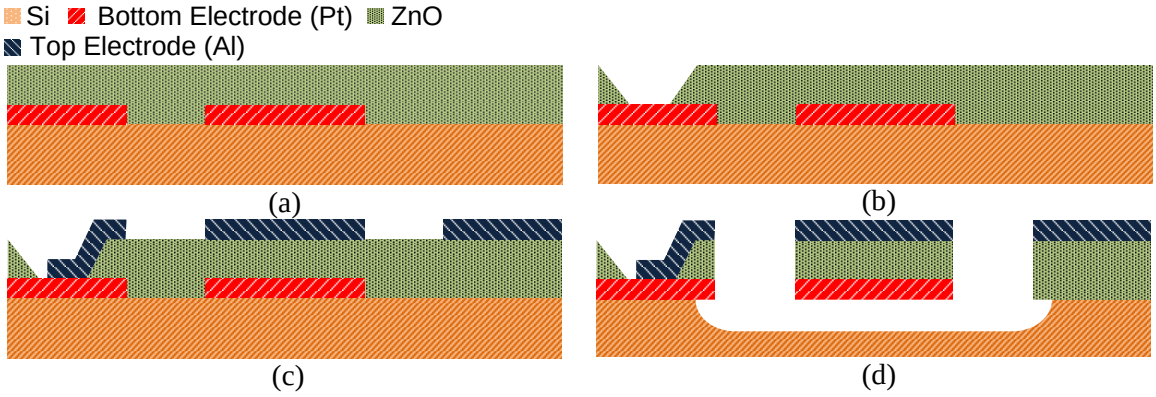

Figure 3.3 – Four-mask post-CMOS compatible fabrication process: (a) patterning of the bottom electrode (Pt) by lift-off and sputtering deposition of the piezoelectric film (ZnO), (b) open vias in ZnO to access the bottom electrode,(c) patterning of the top electrode (Pt) by lift-off,(d) dry etching of ZnO in CH_4-Ar chemistry and SF_6 dry release of the structure

As shown in Figure 3.3(a), formation of the bottom electrodes is followed by the ZnO RF sputtering deposition with the optimized process parameters (i.e., 300°C substrate temperature, 5 mTorr plasma pressure, 1:1 Ar:O_2 ratio, and 100 W RF power). With these parameters, films between 500 nm - 800 nm with a preferential c-axis (002) orientation were deposited with a deposition rate of 100 nm/hr. Openings to contact the bottom electrode are wet etched through ZnO in a mixture of 1: 200 HCl: H_2O. The top platinum electrode is patterned using lift-off followed by pattering of ZnO via CH_4-Ar reactive ion etching (RIE) process. Finally, the device is released by isotropic dry etching of the silicon handle layer with fluorine based chemistry, thereby avoiding stiction between the released microstructures and substrate to significantly increase the yield of the process. As compared with Xenon Difluoride (XeF_2), which is another popular dry release process used for other groups [38][39] for releasing AlN microstructures, the dry release process based on SF_6 chemistry is less amenable to contamination and much safer to operate. The SF_6-based isotropic dry release process can release suspended beams and plates made of piezoelectric materials (i.e., AlN, ZnO and PZT) and metals, while offering much higher etch rate (up to 15 μm/min), superb Si:SiO_2 selectivity (3000:1) and great Post-CMOS process compatible [41]. Table 3.2 summarizes the process parameters used for the SF_6-based isotropic dry release process using the AMS 100 Inductively coupled plasma (ICP) etcher. As seen in Figure 3.4, a 30 μm-diameter and 500 nm-thick piezoelectric ZnO disk resonator with split top electrodes have been successfully released through the SF_6-based dry release process. 500 nm-thick ZnO microstructures embedded between top and bottom Pt electrodes with sizes as large as 100 μm × 300 μm were successfully released without noticeable residual stress.

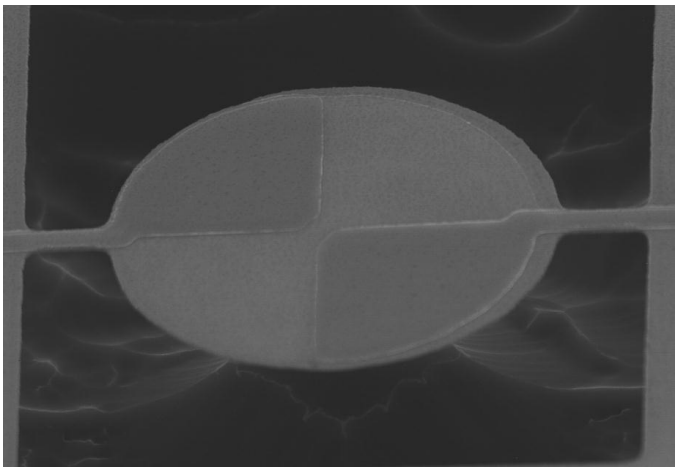

Figure 3.4 – SEM micrograph of a 30 µm-diameter and 500 nm-thick piezoelectric ZnO disk resonator with split top electrodes released using SF_6-based dry release process

Table 3.2 – Parameters for the implemented dry release processes

SF_6 Flow rate	300 sccm
Chamber Pressure	40 mTorr
Chamber Temperature	25 °C
ICP Power	1500 Watts
Etch Rate	~ 5 µm/min

3.4 Fabrication Process for ZnO-on-SOI Resonators and Filters

The devices were fabricated using a low-temperature process composed of five photolithography steps. SOI wafers with device layer thickness of 20 µm and 5 µm are used as the selected substrate for this process. The fabrication process is presented in Figure 3.5. A novel solution has been implemented and successfully demonstrated for releasing devices with silicon as primary part of the resonator body and ZnO as the piezoelectric transducer layer. Since both HF and buffered oxide etchant (BOE) attacks ZnO aggressively, the release process for removing the buried oxide in SOI substrate to suspend the Si resonator body have to be done before the ZnO deposition. Therefore, the modified ZnO-on-SOI resonator fabrication process begins with a HF release process to

entirely remove the buried oxide under the resonator body without compromising the structural integrity of the device layer and the simplicity of the fabrication processes.

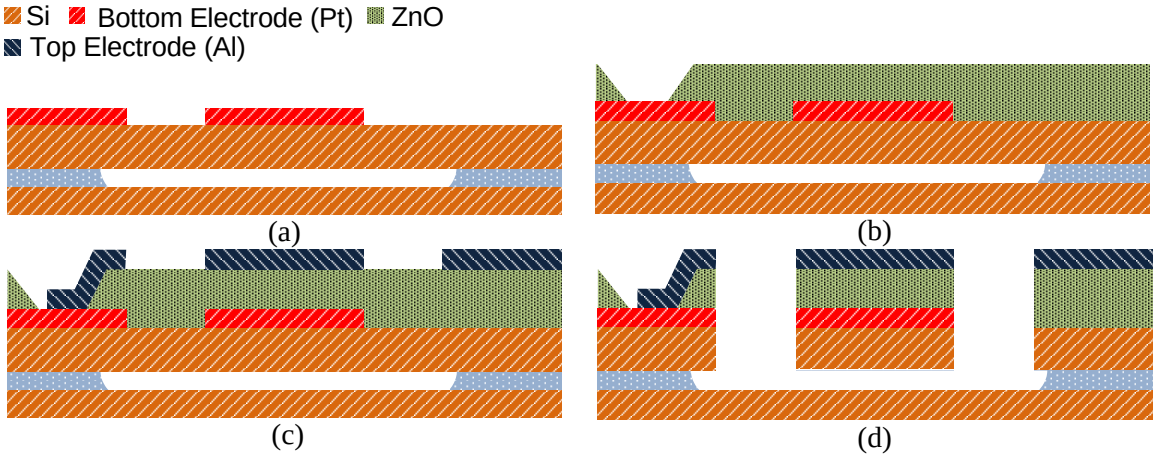

Figure 3.5 – Five-mask post-CMOS compatible fabrication process: (a) Pre-release of the device and patterning of the bottom electrode (Pt) by lift-off, followed by sputtering deposition of the piezoelectric film (ZnO), (b) open vias in ZnO to access the bottom electrode, (c) patterning of the top electrode (Al) by lift-off;(d) dry etching of ZnO in CH_4-Ar chemistry and dry etching of the silicon structural layer with fluorine chemistry

The release process is done by etching a series of release holes in the device layer as the first fabrication step before defining the resonator body. The SOI wafer with the release holes is then submerged in HF 49% solution for 75 minutes. As illustrated in Figure 3.6, the pre-release holes are strategically placed alongside of each device in order to avoid over etch for the smaller devices.

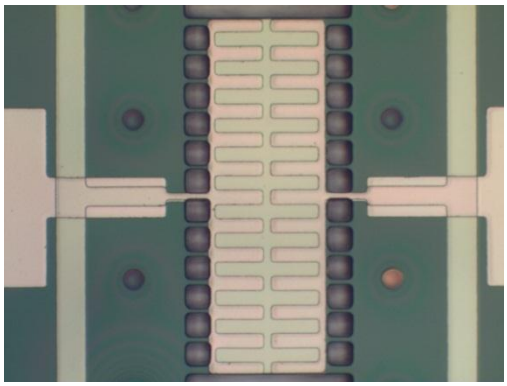

Figure 3.6 – Optical micrograph of a released MEMS filter with strategically positioned pre-release holes along the side of the suspended resonator microstructures.

The fabrication is continued by patterning the bottom electrode by lift-off and followed by ZnO sputtering deposition with optimized parameters (i.e., 300 °C substrate temperature, 5 mTorr plasma pressure, 1:1 Ar:O_2 ratio, 100 W RF power) and deposition time of 5 hr. With these parameters, a 500 nm-thick ZnO film with a preferential c-axis (002) orientation was deposited. Openings to contact the bottom electrode are subsequently wet etched through ZnO in a mixture of 1: 200 HCl: H_2O. The top Al electrode is patterned using lift-off followed by pattering of ZnO via CH_4/Ar RIE process. Finally, the device composed of single or multiple coupled resonator structure(s) is defined by a deep reactive ion etching (DRIE) that penetrate through the pre-released silicon structure layer of the SOI wafer.

Figure 3.7 shows a SEM micrograph of a ZnO-on-SOI filter displaying the interdigitated top electrodes and the release holes fabricated with the process described above. Figure 3.8 shows a close-up view SEM micrograph of the etched profile of a typical microfabricated ZnO-on-SOI device. The scalloping profile along the sidewall can be ascribed to the characteristics of the DRIE Bosch process used to etch the silicon device layer. It is believed that this profile could potentially affect the mechanical quality factor of the fabricated microresonators as demonstrated by [28]. Given the goal of this work is to demonstrate a fabrication process amenable for high volume production that can be readily transferred to a commercial CMOS or MEMS foundry, it is much more sensible to use a widely-adopted standard DRIE silicon dry etching process rather than creating a highly-specialized but rarely used technique.

It is important to mention that Platinum metallization should be probably changed because is not directly compatible with standard CMOS materials. Nevertheless, the process described in the previous sections can be considered as Post-CMOS compatible. The Platinum electrodes can be substituted by Molybdenum electrodes if AlN is used as piezoelectric material instead of ZnO. Molybdenum is a metal that lately has been used more frequently for the gate metallization in the state of the art CMOS transistors.

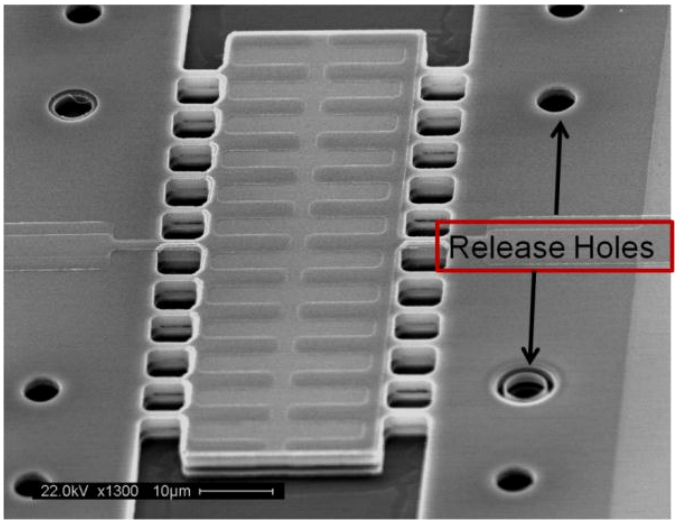

Figure 3.7 – SEM micrograph of a ZnO-on-SOI resonator fabricated in a 5 µm SOI substrate using the process described above

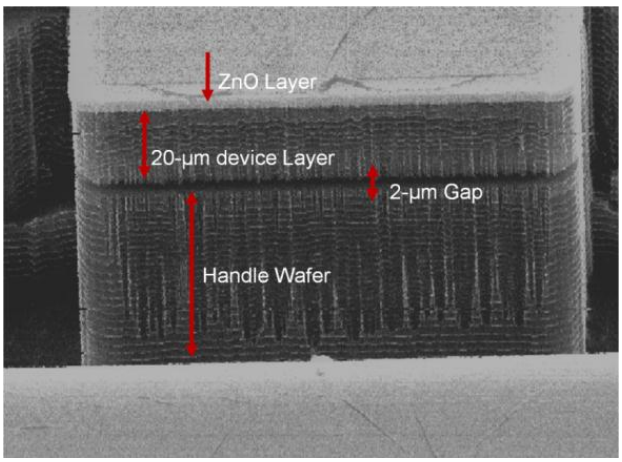

Figure 3.8 – SEM micrograph with a close view of a ZnO-on-SOI device resonator fabricated in a 20 µm SOI substrate

Chapter 4

Piezoelectrically-Transduced Contour Mode Resonators

This chapter presents the equivalent circuit models and measurements results of the microfabricated two-port contour-mode thin-film piezoelectric resonators and ZnO-on-silicon resonators studied by this work. Thin film piezoelectric resonators have been fabricated using ZnO layers with thickness varying between 500 nm and 800 nm; whereas piezo-on-silicon resonators have been fabricated using SOI wafers with 5 µm or 20 µm-thick silicon device layers. Piezoelectrically-transduced contour-mode resonators with different geometries and designs are presented along with their corresponding equivalent circuit models.

4.1 Contour Modes in Circular Disks

Figure 4.1 presents the finite element modal analysis of a 30 µm-diameter ZnO-on-silicon disk resonator that consists of 20µm-thick silicon device layer and a 500 nm-thick ZnO piezoelectric transducer layer embedded between the top and bottom metal electrodes. This configuration permits the excitation of the radial contour mode and the wine glass mode that operates at different resonance frequency. Only two support tethers with strategically-designed dimensions are introduced in order to minimize the acoustic energy losses leaked through the anchors. In order to excite the wine glass mode while minimizing the anchor related losses, the supporting tethers were located at the quasi-nodal locations (the blue are of the wine glass mode shape shown in Figure 4.1(b)),where

the circular plate does not have any radial displacement. A simplified frequency equation for a disk resonator vibrating in a radial contour mode is given by [42]:

$$f_o = \frac{\alpha}{R}\sqrt{\frac{E_p}{\rho_p(1-\mu^2)}} \tag{4.1}$$

where E_p , ρ_p and μ represent the Young's modulus, density and Poisson's ratio of the structural material, R is the radius of the disk, and α is a frequency constant related to the vibration mode and the Poisson's ratio. For the case of $\mu = 0.3$, α takes the value of 0.342 and 0.272 for the first radial contour mode, and the fundamental wine glass mode, respectively. For other values of the Poisson's ratio (μ), a ten percent increase in μ would result in a two percent increase in the value of α for the radial modes and one percent decrease in its value for the wine glass modes.

(a) (b)

Figure 4.1 – Comparison of the finite-element simulated mode shapes for a 30 µm-diameter ZnO-on-silicon disk resonator with a 20 µm-thick device layer and a 500 nm-thick ZnO layer operating in its radial-contour mode at 88.43 MHz and wine-glass mode at 65.28 MHz

In order to model the mass loading effect of the electrodes, the resonance frequency Equation (4.1) is modified as follows:

$$P_{eq} = \frac{\rho_{top}T_{top} + T_{bottom}\rho_{bottom} + \rho_p T_p}{T_{top} + T_{bottom} + T_{piezo}} \tag{4.2}$$

$$v_{eq} = \left[\frac{E_p T_p + E_{top} T_{top} + E_{bottom} T_{bottom}}{\left(\rho_{top} T_{top} + T_{bottom} \rho_{bottom} + \rho_p T_p \right) (1 - \mu^2)} \right]^{1/2} \tag{4.3}$$

$$f_o = \frac{\alpha}{R} v_{eq} \tag{4.4}$$

where v_{eq} represents the equivalent acoustic velocity, and P_{eq} is equivalent density of the resonator. This approximation is only valid for a resonator vibrating in a contour-mode. However, a similar expression can be derived for devices vibrating in a thickness-mode. The same analysis can be modified for the case of piezo-on-silicon resonator, where a major part of the resonator body is made of non-piezoelectric material such as single crystalline silicon. The piezoelectric layer introduces a mass loading effect aside from acting as the piezoelectric transducer. The equivalent density and acoustic wave velocity can be modeled as follows:

$$P_{eq} = \frac{\rho_{top} T_{top} + T_{bott} \rho_{bott} + \rho_p T_p + \rho_{dev} T_{dev}}{T_{top} + T_{bott} + T_p + T_{dev}} \tag{4.5}$$

$$v_{eq} = \left[\frac{E_p T_p + E_{top} T_{top} + E_{bott} T_{bott} + E_{dev} T_{dev}}{\left(\rho_{top} T_{top} + T_{bott} \rho_{bott} + \rho_p T_p + \rho_{dev} T_{dev} \right) (1 - \mu^2)} \right]^{1/2} \tag{4.6}$$

A similar analysis could be carried out to calculate the equivalent Poisson's Ratio of a multilayer structure. However, for simplicity, a Poisson's ratio of $\mu = 0.3$ has been selected for all the subsequent model derivations. The mechanical properties of the materials used for the piezoelectrically-transduced resonators and filters in the present work are listed in Table 4.1.

Table 4.1 – Mechanical properties of the materials used for the fabrication of piezoelectrically-transduced resonators and filters

Material	Young's Modulus (GPa)	Density (Kg/m^3)	Poisson's ratio
Si	170	2329	0.226
ZnO	123	5676	0.330
Al	70	2700	0.350
Pt	168	21450	0.380

The equivalent mass for a micromechanical resonator at any location can be obtained by dividing the total kinetic energy by one half of the square of the velocity at that location [42]. The mass at a location on the disk perimeter can then be obtained using the relation:

$$M_{eq} = \frac{2\pi\rho_{eq}T_{eq}\int_0^R J_1^2\left(\frac{\omega_n}{v_{eq}}r\right)dr}{J_1^2\left(\frac{\omega_n}{v_{eq}}r\right)} \tag{4.7}$$

where J_1 is the Bessel function of the first kind and R is the radius of the resonator disk. The electromechanical coupling coefficient can be calculated as follows:

$$\eta = \frac{Q_{Total}}{u_{max}} = \frac{2E_p}{1-\mu}\iint\left(\frac{\partial u_r}{\partial r} + \left(\frac{u_r}{r} + \frac{1}{r}\frac{\partial u_\theta}{\partial \theta}\right)\right)dA \approx E_p d_{31}\pi\frac{R}{2} \tag{4.8}$$

This expression for the electromechanical coupling coefficient is derived for the disk resonator with two split top electrodes that cover only half of the resonator body. The electrical equivalent parameters for a disk resonator in a two-port configuration are defined by the set of equations detailed in Section 2.7.

4.2 Experimental Results

The fabricated micromechanical resonators were tested by on-wafer probing using a Cascade RF probe station in air at atmospheric pressure and ambient temperature. The scattering parameters (S-Parameters) of the devices are extracted directly using an Agilent E5071B vector network analyzer. A Short-Open-Load-Thru (SOLT) calibration procedure using a CS-5 calibration substrate from GGB Industries Inc was conducted to de-embed the effects of connectors, the carrier substrate and errors related to the vector network analyzer. The schematic of the experimental setup used for testing the micromechanical resonators and filters of the present work is presented in Figure 4.2.

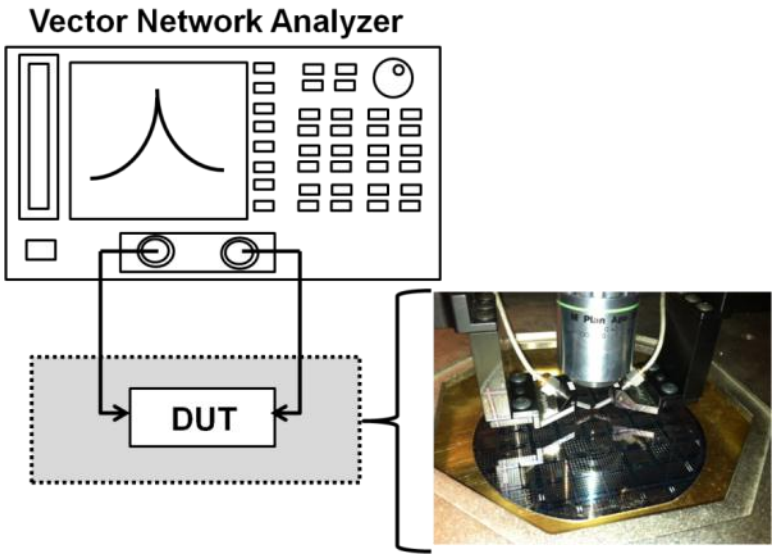

Figure 4.2 – Experimental set up for on-wafer probing of the microresonators and filters

4.2.1 Contour Modes in Thin Film Piezoelectrically-Transduced Disk Resonators

Thin film ZnO piezoelectric resonators were tested in their radial contour and the wineglass modes. Devices with radius of 20 μm, 30 μm and 40 μm were fabricated in a two port configuration. Figure 4.3 shows the frequency response for 30 μm-radius ZnO piezoelectric disk resonator operating in the fundamental and the 2nd radial-contour

modes, shown in Figure 4.3 (a) and Figure 4.3 (b), respectively. The device in its fundamental radial-contour mode exhibits a quality factor of 1,053 with a motional resistance of 11.57 kΩ. The same device when operating in its 2nd radial-contour mode exhibits a lower *Q* of 590 with a motional resistance of 18.87 kΩ. The top electrode was designed to excite and detect both the radial contour and wineglass modes, which limits the achievable excitation and detection efficiency through the piezoelectric transducer. If the top electrode is divided into two symmetrical halves instead of covering only a quarter of the top surface, the motional resistance of this device in its radial contour mode will be reduced by 4 times.

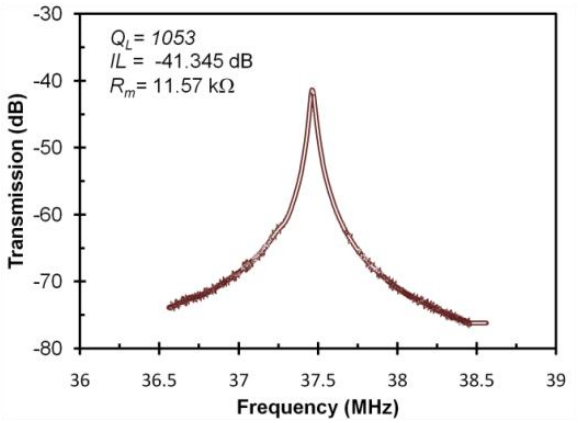

(a)

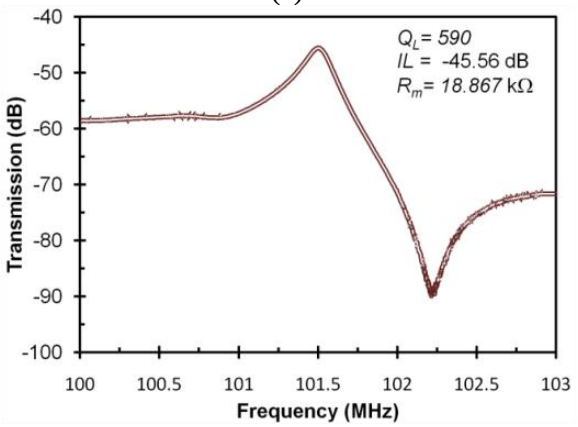

(b)

Figure 4.3 – Frequency responses of 30 μm-radius piezoelectric disk resonator (a) operating in the fundamental radial contour mode; and (b) the 2nd radial-contour mode

Figure 4.4 shows the measured frequency response of a 30 μm-radius ZnO piezoelectric disk resonator operating in its fundamental wineglass mode. The resonator has a pair of 3 μm-wide tethers which is located at its quasi-nodal points thus resulting in a high-*Q* as compared with the radial modes. However, despite its high *Q*, the resonator exhibited a motional resistance (86 kΩ) much higher than those of ZnO piezoelectric rectangular plates and other piezo-on-silicon contour-mode resonators (c.f. Section 4.2.2).

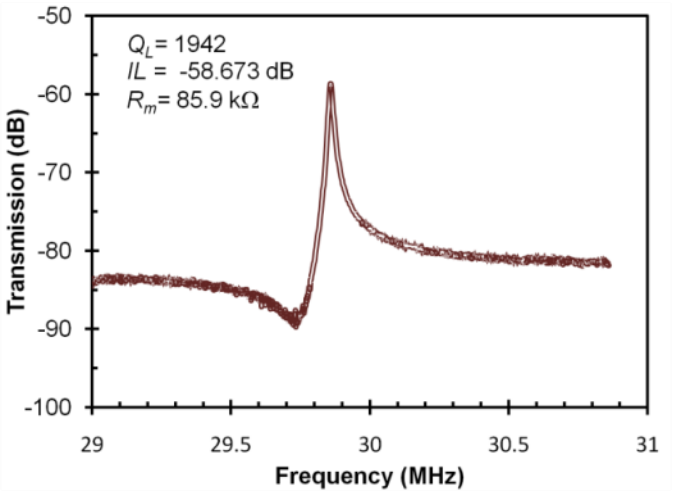

Figure 4.4 – Frequency response for a 30 μm-radius ZnO piezoelectric disk resonator operating in its fundamental wineglass mode

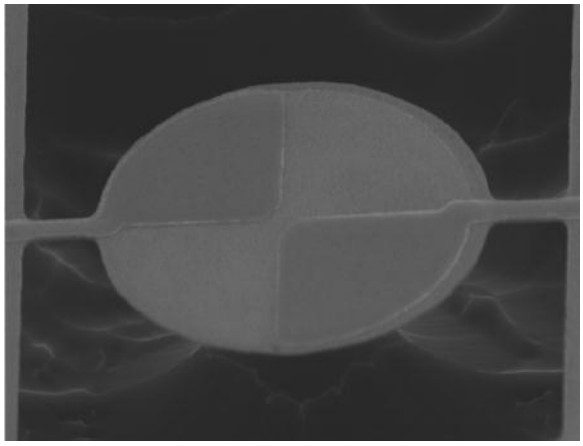

Figure 4.5 – SEM micrograph of a 30 μm-radius ZnO piezoelectric disk resonator

Although both 20 μm and 40 μm-radius disk resonators also have been fabricated, the measured results are quite similar. The average quality factors for the fundamental and 2nd radial contour modes are around 2,000 and 600, respectively. These devices also suffer from large motional impedance. Similar results have been reported for piezoelectrically-transduced disk resonators made of AlN [46], where resonators vibrating in contour modes with *Q's* on order of 3,000 and high motional impedance (>100 kΩ) have been demonstrated previously.

At this point, it is worth mentioning that measured quality factor of the fabricated resonators correspond to the loaded *Q* or Q_L, however the real figure of merit for this parameter correspond to the unloaded *Q* or Q_u. The unloaded *Q* is the ratio of stored energy to the dissipated energy in a LC circuit or tank. The loaded *Q* is the measured quality factor which includes the loading from the external circuit. Only the loaded *Q* of a resonator can be measured experimentally, and the unloaded *Q* has to be extrapolated. From the S-parameter measurements, the correlation between Q_L and Q_U for a resonator is expressed as:

$$Q_U = \frac{Q_L}{1 - 10^{\frac{S_{21}(dB)}{20}}} \tag{4.9}$$

where S_{21} is the transmission coefficient between the input and the output of the resonator. For the 30 μm-radius disk resonator shown in Figure 4.3(a) the value of unloaded *Q* is 1062, which is quite similar to the value of the loaded *Q* (i.e., Q_L=1,053). However, this will not be always the case, especially when the motional resistance of the resonator tank approaches to the value of the termination resistance, which for most communication systems is 50 Ω.

4.2.2 Contour Modes in ZnO-on-SOI Disk Resonators

Pursuant to obtain devices with higher quality factor and lower motional resistance, piezoelectric-on-silicon (ZnO-on-SOI) resonators that employ single crystal silicon as its primary structural layer were design and fabricated. The operation principle of these devices is the same as the one reported in Section 4.1. In piezo-on-silicon contour-mode resonators, the acoustic energy is mostly contained in the low acoustic loss single crystalline silicon that lead to improved quality factor as compared to a counterpart device made of thin-film ZnO piezoelectric material with higher acoustic losses. In this work, contour mode disk resonators with 20 µm, 30 µm and 40 µm radius were fabricated using SOI substrates with 5 µm and 20 µm-thick silicon device layer, to investigate the effect of the thickness of the stacked resonator structural materials (i.e., ZnO and single crystalline silicon) on the quality factor of the device.

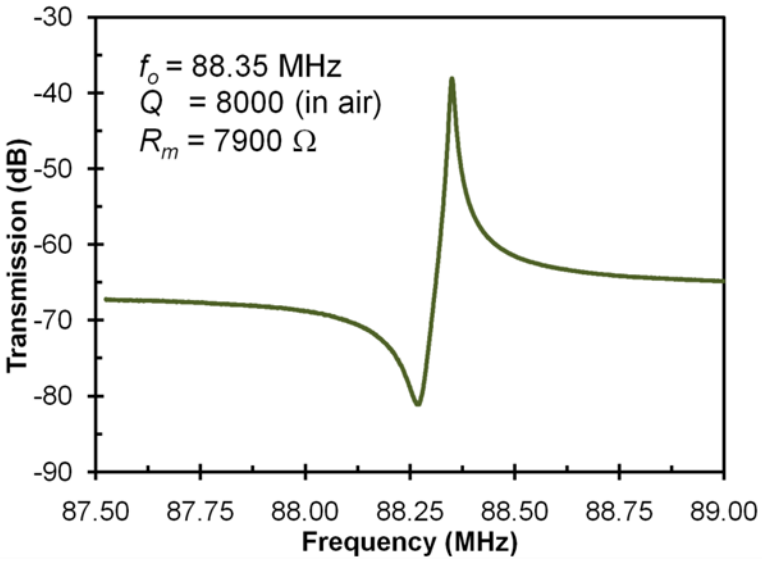

Figure 4.6 – Frequency response of 30 µm-radius piezo-on-silicon disk resonator excited in its fundamental radial contour mode, showing a *Q* of 8,000 at 88.35 MHz

Figure 4.6 presents a 30 μm-radius piezo-on-silicon disk resonator operating in the fundamental radial contour mode at 88.35 MHz with a measured *Q* of 8,000. The resonator body is composed of a 20 μm- thick silicon device layer and a 500 nm-thick ZnO piezoelectric layer. This device uses two 3 μm-wide anchors with their length strategically designed to quarter wavelength ($\lambda/4$) long in order to maximize its quality factor by decreasing the acoustic energy radiation from the resonator body through the support tethers to the substrate. Even though this resonator is much heavier than the identically-sized piezoelectric resonator made of a thin film ZnO layer (Section 4.2.1), its motional resistance is 1.5 times lower. This is largely due to its improved quality factor (*Q* ~ 8,000). Moreover, its motional resistance can be further decreased by a factor of 4 by designing the top electrodes to cover the whole resonator surface or using a thinner silicon device layer. In order to explore the impact of the silicon device layer thickness, the identically-sized device was also fabricated with a 5μm-thick silicon device layer while retaining the thickness of the ZnO layer (500 nm) and the electrodes.

As can be observed in Figure 4.7, the motional resistance decreased almost four times as compared with the identically sized device fabricated with a 20 μm-thick silicon device layer. The slight decrease in the quality factor is due to the reduction of the silicon device layer thickness, meaning that a major part of the resonator structure is made of ZnO, a material with higher acoustic loss. Although the decrease in the quality factor for this device in this particular design is only 16%, the quality factor is expected to degrade more for resonators with even thinner device layer. In the meantime, as the silicon device layer gets thinner, the top ZnO piezoelectric transducer layer becomes a greater portion of the resonator body, thus enhancing the electromechanical coupling coefficient

and lowering the motional resistance. Therefore, a trade-off must be made between quality factor and motional resistance, which both heavily depend on the silicon device layer thickness, but in opposite ways. Based on our measurement results so far, the optimum silicon device layer thickness should range from 4 μm to 10 μm for the piezoelectric ZnO layer with thickness between 0.5 μm and 1.0 um. As shown in Figure 4.7, the resonance frequency is also shifted down from 88.35 MHz to 80.42 MHz as a direct result of the reduced silicon device layer thickness from 20 μm to 5 μm, which is largely owing to the more severe mass loading effect from the ZnO layer and the electrodes that have lower acoustic velocities. As expected from Equation (4.6), if the thickness of the silicon device layer is reduced, the more severe loading effect would result in a reduction of the resonance frequency. However, this frequency shift can be accurately predicted with less than 1% error and can be corrected via revised CAD layout by decreasing the lateral dimensions of the resonator to hit the target frequency as needed for oscillators and filters.

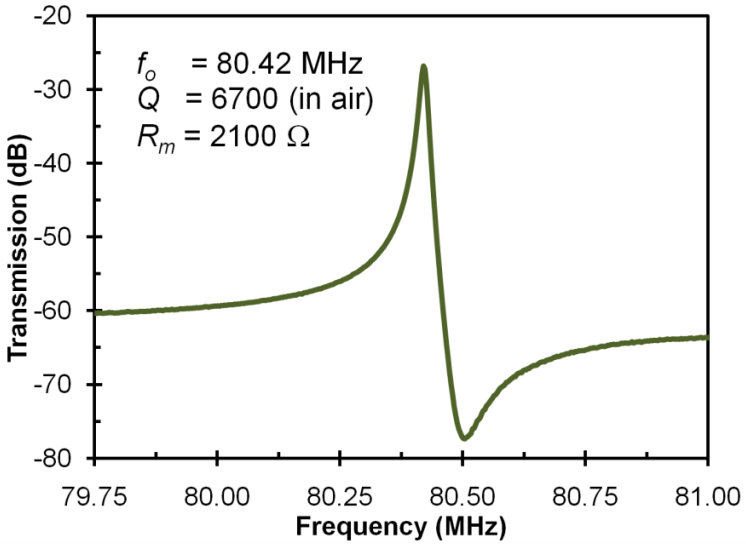

Figure 4.7 – Frequency response of a 30 μm-radius Piezo-on-silicon disk resonator with a 5 μm-thick silicon device layer, excited in the fundamental radial contour mode, showing a loaded Q of 6,700 at 80.375 MHz

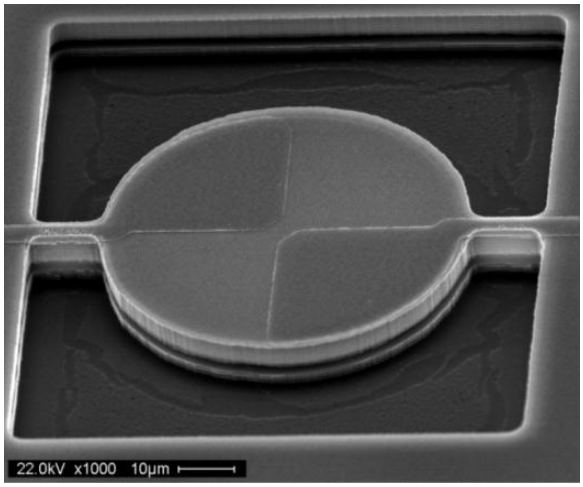

Figure 4.8 – SEM micrograph of a 30 um-radius piezo-on-silicon disk resonator fabricated with a SOI wafer with 5 µm-thick silicon device layer, showing the device in its two-port configuration with two split top electrodes. The measured frequency response for this device is shown in Figure 4.7

4.2.3 Quality Factor in ZnO-on-SOI Resonators

When determining the quality factor of a micromechanical resonator, several energy dissipation mechanisms must be taken into account including air damping, material related losses, thermoelastic damping, and anchor losses. The overall resonator *Q* can be found as the sum of the inverses of the individual *Q*'s associated with all the contributing loss mechanisms:

$$\frac{1}{Q_{total}} = \frac{1}{Q_{air}} + \frac{1}{Q_{material}} + \frac{1}{Q_{thermoelastic}} + \frac{1}{Q_{anchor}} \tag{4.10}$$

Air damping depicts the loss of energy contained in a resonating structure to the surrounding atmospheric environment. For the case of micromechanical structures that have high a surface-to-volume ratio, air damping represents a major source of energy dissipation. Particularly, resonators with electrostatic transduction mechanism are much more vulnerable to a specific type of air damping known as squeeze-film damping that considerably lowers the quality factor of such devices especially at low frequency. The

squeeze-film damping occurs in a capacitively-transduced resonator as the vibrating resonator body moves in close proximity to the surrounding electrodes, in effect alternately stretching and squeezing any "fluid" (i.e., ambient gas) that may resides within the capacitive transducer air gap. Piezoelectrically-transduced resonators are less susceptible to air damping compared with electrostatically-transduced resonators, since piezoelectric transducers do not require narrow air gaps. As demonstrated by other researchers, contour-mode piezoelectrically-transduced resonators operating in vacuum at frequencies below 300 MHz have shown a noticeable improvement (i.e., 20%-50%) as compared to the same device during vacuum-less operation [30][32]. The effect of air damping decreases at higher resonance frequencies due to that the resonator displacement diminishes with frequency as reported by Wang *et al.* [17], who demonstrated the operation of a capacitively-transduced micromechanical disk resonator vibrating at 1.156 GHz with a *Q* of 2,700 both in vacuum and air.

In the present work, resonators have not been evaluated in vacuum due to the lack of a vacuum measurement set-up at the University of South Florida. However, this limitation is not a major bottleneck against the main objective of this work, which is to design and implement the several filter topologies based on contour-mode piezoelectric or piezo-on-silicon resonators operating in ambient environment without the need for vacuum packaging for RF applications, with percentage bandwidth between 1% and 5%.

Anchor loss is the portion of the vibration acoustic energy that is not completely confined within the resonator body, and rather capable of transmitting through the support anchor(s) to the substrate. The amount of acoustic energy radiating through the anchor(s) is considered as anchor related losses as it is not conserved within the

resonator. Based on the convention wisdom for reducing the anchor losses, the number of tethers attached to the resonator is kept as low as possible and their lengths are either design to be quarter-wavelength ($\lambda/4$) or electrically short (i.e. less than $\lambda/8$). A quarter-wavelength tether operates as acoustic transmission line that transforms a fixed end to a free end that is capable to moving without any constraints. Meanwhile, the width of the tethers is designed to be as narrow as possible for certain designs such as radial contour mode disk resonators. However, this rule of thumb might not be applicable at gigahertz frequencies. In particular, the quarter-wavelength theaters of resonators operating at gigahertz frequencies approach 4 μm in length, making it difficult for fabrication of such small supports. Although support related losses in micro-machined flexural-mode beam resonators and contour-mode disk resonators anchored at the center have been modeled [47][48], there does not exist a general model for anchor losses that could be applicable to the resonators on this work. However, a short experiment have been carried out in which is demonstrated that the width of the anchor substantially affects the *Q* of the resonator. Results of the aforementioned experiment are summarized on Table 4.2.

Table 4.2 – Statistical data for the anchor loss study of 30 μm-radius piezo-on-silicon micromechanical disk resonators fabricated with a SOI substrate with a 20 μm-thick silicon device layer

Support width (μm)	**Resonant Frequency (MHz)**	**Theater Number**	**Quality Factor**
3	88.350	2	8,000
5	88.293	2	6,395
7	88.190	2	5,980
10	88.092	2	4,650
3	88.240	4	6,670
5	88.024	4	5,500
10	87.898	4	4,110

Thermoelastic energy dissipation is caused by irreversible heat flow across the resonator structure, which is driven by the temperature gradient between stretched and compressed regions, which result in loss of the vibration energy. When a mechanical structure undergoes a load, the strain field leads to distribution of the internal energy so that the compressed region gets warmer and the extended region becomes cooler. The mechanism responsible for thermoelastic damping is basically the outcome due to lack of thermal equilibrium between various parts of the vibrating structure. Energy is dissipated through irreversible heat flow driven by the temperature gradient thereby degrading the *Q* of the microresonators. A comprehensive study of this loss mechanism can be found in Zener's classical work [49]. Although the thermoelastic damping is the dominant loss mechanism for micro-beam resonators undergoing flexural vibrations at low frequency (i.e., tens of megahertz) [50], its impact is much less severe for resonant microstructures excited in contour-mode vibrations with resonance frequencies beyond the characteristic cutoff frequency of the thermoelastic damping [51].

The material loss mechanism limits the absolute maximum quality factor of a mechanical resonator made of a certain material. The contribution of this loss mechanism in the overall quality factor of a resonant structure can be quantified by means of the acoustic attenuation coefficient (α). The larger this coefficient for a material, the lower the absolute maximum achievable quality factor of the resonator made of such a material will be. Piezo-on-silicon resonators leverage the fact that the acoustic attenuation in materials such as silicon, silicon carbide and diamond is much lower than the attenuation in common piezoelectric materials, such as PZT, AlN and ZnO. Specifically for the case of the ZnO-on-silicon resonators investigated in the present work, resonators with thicker

silicon device layer exhibited higher quality compared with devices with thinner device layer, as mentioned in Section 4.2.2. Although the highest quality factor for the resonators studied in this work is around 8,000, higher quality factors can be achieved if low acoustic loss device layers such as chemical vapor deposited diamond in conjunction with a low acoustic loss piezoelectric material such as AlN are employed. However, both AlN and diamond deposition require production-grade tools currently not available at USF.

4.2.4 Temperature Dependence

The resonance frequency of a contour-mode resonator is governed by the Young's modulus, the material density and its geometry. Because the aforementioned parameters all change with temperature, the temperature coefficient of the resonance frequency manly relates to their temperature dependence. Both timing and frequency reference applications rely on the use of highly stable resonators with frequency variation less than 20 ppm over the whole operating temperature range (generally -25 °C to 100 °C). A resonator technology that can fulfill the above frequency stability with the advantages of small footprint and power consumption is highly desirable.

The temperature coefficient of frequency (*TCF*) of a resonator is generally expressed as follows with a unit of ppm per degree Celsius:

$$TCF = \frac{1}{f_o}\frac{\partial f}{\partial T} = -\frac{1}{a}\frac{\partial a}{\partial T} + \frac{1}{2}\frac{1}{E_p}\frac{\partial E_p}{\partial T} - \frac{1}{2}\frac{1}{\rho}\frac{\partial \rho}{\partial T} \tag{4.11}$$

where f_o is the resonance at the normal temperature operation point (i.e., room temperature ~ 25˚C), a is the fundamental geometrical parameter that sets the device resonance frequency, and T represents the temperature of operation. This Equation is very general and does not take into account the particular modal of vibration of the structure,

but in general can be used as a realistic approximation. The third term in Equation (4.11) can be neglected due to its low impact on the overall coefficient. The TCF is expressed in a simplified form as follows:

$$TCF = -\alpha_p + \frac{1}{2} TC_{E_p} \tag{4.12}$$

where α_p is the thermal expansion coefficient of the piezo layer in the thin film piezoelectric resonators, or the thermal expansion coefficient of the stacked piezo and silicon device layers in the ZnO-on-SOI resonators, and TC_{E_p} is the temperature coefficient of the Young's modulus of the piezo layer or the stacked piezo and device layers for ZnO-on-SOI resonators. The metal top and bottom electrodes also contribute to the overall *TCF* value, however they were not taken in account in the simplified model.

Table 4.3 – Thermal expansion coefficient for silicon and ZnO [52]

Material	α	TC
Silicon	-2.6 ppm/ºC	-40 ppm/ºC
Zinc Oxide	(-4.4) – (-5.6) ppm/ºC	-50 ppm/°C

The frequency response for a 30 µm-radius disk resonator operating in its fundamental radial contour-mode for both thin film piezoelectric and ZnO-on-SOI resonators are reported in Figure 4.3 and Figure 4.6, respectively. The measurements were carried out using a cascade probe station with a temperature controlled chamber. The scattering parameters (s-parameters) of the device were extracted directly using an Agilent E5071B vector network analyzer. A Short-Open-Load-Thru (SOLT) calibration procedure was implemented to de-embed the effects of connectors and the carrier substrate. The device wafer was heated between room temperature and 120°C while the resonance frequency is continuously monitored. The *TCF* shows a perfectly linear

behavior over the whole temperature range as seen in Figure 4.9. The measured *TCF* for the 30 µm-radius disk ZnO-on-SOI resonator has the value of -31.05 ppm/ºC, which is higher as compared with other resonator technologies that uses silicon and polysilicon as a structural material [16][17][53]. The apparent discrepancy between the measured *TCF* and prior reports for silicon-based resonators can be attributed to impacts of the ZnO layer and the metal electrodes. Figure 4.9 also shows the measured *TCF* for a thin film piezoelectrically-transduced disk resonator of 30 µm-radius. As was expected, the *TCF* for this case is higher as compared with the resonator with silicon as the major part of the structural device layer. However, it is still almost two times lower as compared with the *TCF* for uncompensated FBAR resonators, which has been reported to be close to -60 ppm/ºC [54].

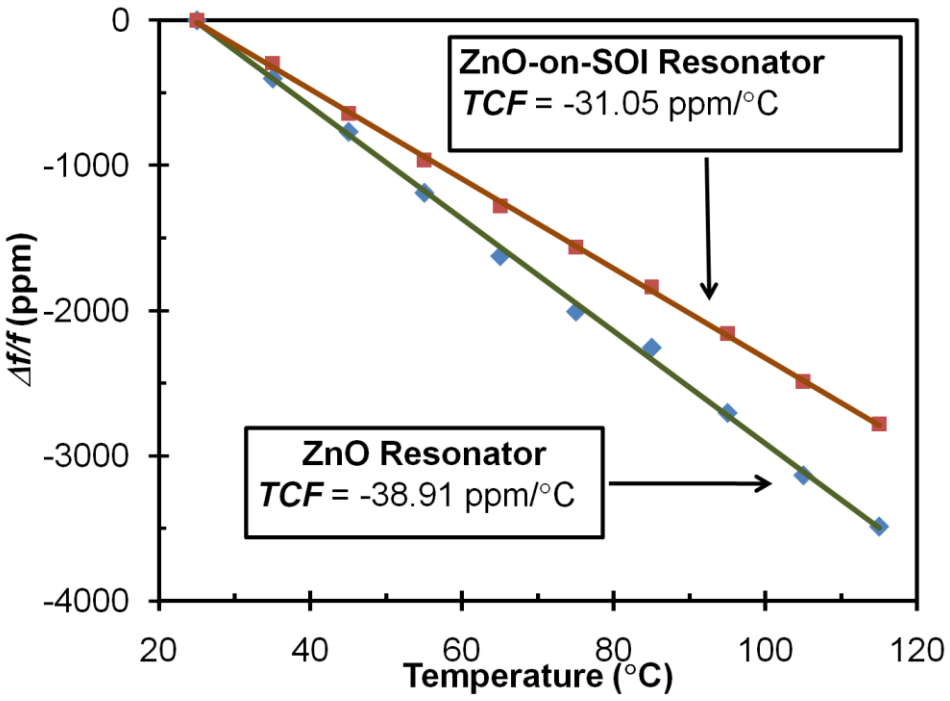

Figure 4.9 – Measured fractional frequency change versus temperature for a 30 µm-radius disk piezoelectrically-transduced resonator operating in the 1st radial contour mode

Although the measured uncompensated *TCF* for this kind of resonator could be sufficient for front-end RF pre-select and image-reject filter applications, this is not adequate for timing and frequency reference applications such as oscillators. The *TCF* of the fabricated devices is significantly larger in magnitude than that of the worst AT-cut quartz crystals [55]. Nevertheless, this uncompensated temperature coefficient could be further reduced by several different methods, including micro oven stabilization [56], and temperature compensation of silicon via degenerate boron doping and boron-assisted aluminum doping [57]. However, the first approach is a power hungry and the second method is relatively costly due to the need of low resistive silicon wafer (<0.001 Ω-cm).

4.3 Length-Extensional Mode in Piezoelectrically-Transduced Plate Resonators

Figure 4.10 shows the first four length-extensional modes in piezoelectrically-transduced plate resonator. Several in-plane length-extensional mode shapes can be excited in a rectangular plate resonator either by changing its physical dimensions or by engaging higher order modes. The piezoelectric detection of these modes relies on the strength of the electromechanical coupling, which is directly related with the electrode design. Therefore, only those resonance modes for which the net charge on the surface on the electrodes is non-zero can be detected electrically. From the transducer design and modal analysis point of view, the top electrode should be patterned to match the shape of the strain field for a desired resonance mode at the target frequency.

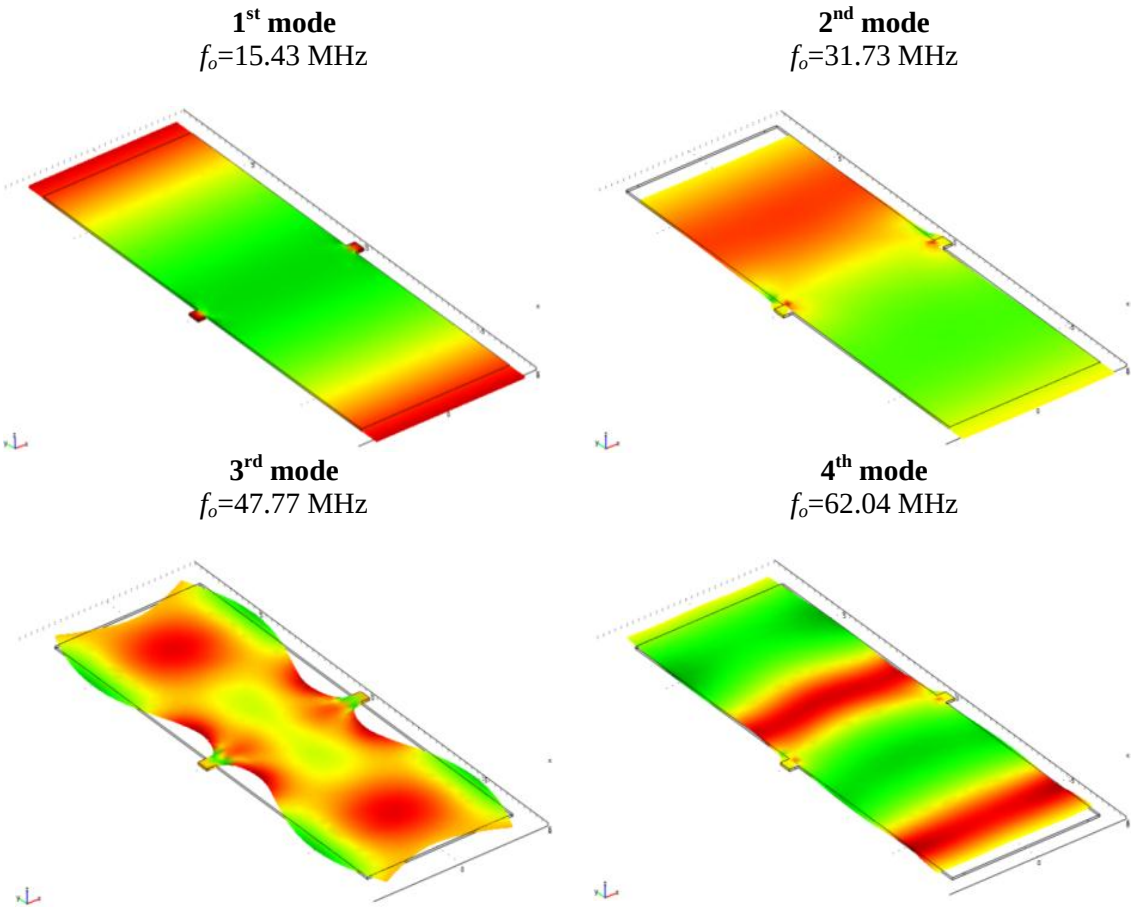

Figure 4.10 – Simulated mode shapes for dilation-type contour-modes (via FEMLAB COMSOL) for a 140 μm × 50 μm rectangular plate made of 500 nm-thick ZnO

If a two-port configuration with the electrodes parallel to width of the rectangular plate is chosen, only the first and second mode can be electrically detected as shown in Figure 4.10. Due to the electrode configuration, the third and the fourth modes are expected to generate very small net charge for all typical top electrode designs. In order to be able to detect the high-order length-extensional modes of a rectangular plate through piezoelectric transduction, a pair of interdigitated top electrodes with optimum patterns is needed.

The simulated response of the 9th length-extensional mode of a rectangular ZnO plate resonator with dimensions of 140 µm × 50 µm is shown in Figure 4.11 with a pair of strategically-designed interdigitated top electrodes. As shown by the modal simulation, the regions in green color represent areas under compressive strain whereas the red color highlights the regions under tensile strain. As rule of thumb, in order to excite higher order resonance modes, the top electrodes should be designed to match the periodic strain field pattern of the targeted mode shape to maximize the electromechanical coupling. Although closed-form solutions for higher-order resonance modes of an ultra-thin rectangular plate could be readily derived under the plane stress assumption, the accuracy would not be sufficient when the thickness of the plate resonator becomes comparable with its lateral dimensions. This is a particular concern for the ZnO-on-SOI devices with 20 µm-thick silicon device layer. Therefore, the modal analysis by finite element method (FEM) simulation of the resonance mode shape of a chosen structure provides considerable insight for design optimization of the top electrodes over the piezoelectric transducer for the purpose of maximizing the electromechanical coupling.

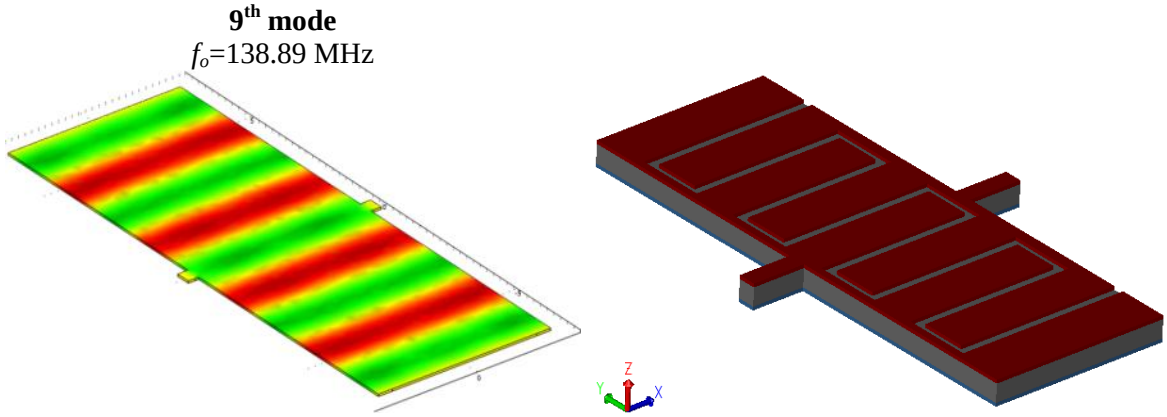

Figure 4.11 – (a) The 9th order length-extensional resonance mode-shape of a ZnO plate resonator ; (b) Interdigitated resonator design

In order to analyze the expression for the resonance of such device and derive the equivalent electromechanical model for a rectangular plate resonator, the approach presented in Section 2.5 is used. The resonance frequency equation is given by:

$$f_n = \frac{n}{2l} v_{eq} \tag{4.13}$$

where l is length of the plate, v_{eq} is equivalent acoustic velocity of the structural material, and n is the mode number. The same approach used for the contour-mode radial disk resonator presented in Section 4.1 can be used to modify Equation (4.13) in order to accurately predict the resonance frequency for thin-film ZnO resonators and ZnO-on-SOI resonators with rectangular geometries. The equivalent mass of a rectangular plate resonator can be computed by:

$$M_{eq} = \rho T \iint \left(u_x^2 + u_y^2\right) dxdy \approx \rho_{eq} \frac{wlT_{eq}}{2} \tag{4.14}$$

where w, l, T_{eq}, and ρ_{eq} are the width, length, thickness and equivalent density of the resonator. Equation (4.14) applies to the calculation of the equivalent mass for the fundamental length and width extensional modes, as well as their higher order modes. Contrary to the case of a disk resonator, the equivalent mass for a rectangular plate is not dependent on the resonance mode (i.e., width-extensional or length-extensional) and the mode of operation (i.e., fundamental or higher order modes). As defined by Equation (2.16), the electromechanical coupling factor is the ratio between the total induced charge on the surface of the resonator and the maximum displacement. For a rectangular plate resonator vibrating in its length-extensional contour mode, the electromechanical coupling factor is given by:

$$\eta = \frac{Q_{Total}}{u_{max}} = \frac{2E_p}{1-\sigma}\iint\left(\frac{\partial u_x}{\partial x} + \frac{\partial u_y}{\partial x}\right)dA \approx 2E_p d_{31} w \tag{4.15}$$

where E_p represents the equivalent Young's modulus of the structure, d_{31} is the piezoelectric coefficient, and w represents the width of the top electrode. For a device in a two-port configuration the actual value of w is half of the width of the plate, since the top electrodes are divided into two symmetrical halves (one for actuation and the other for sensing). For a device in a one-port configuration, the entire top electrode is used for actuation. For a resonator equipped with the interdigitated electrode, w represents the width of the electrode. As illustrated in Figure 4.11, the interdigitated electrode regions with equal phase are electrically connected. Hence, the electromechanical coupling factors for the input and the output port are:

$$\eta_1 = N_1\left(2E_p d_{31} w\right) \tag{4.16}$$

$$\eta_1 = N_2\left(2E_p d_{31} w\right) \tag{4.17}$$

where N_1 and N_2 are the number of electrode regions (fingers) for the input and the output electrodes, respectively. It can be seen in Figure 4.11 that the input and output interdigitated electrodes cover almost the entire surface area of the resonator plate with the separation between electrode fingers set by the minimum fabrication tolerance. For a device operating in its n^{th} (an odd number) mode that corresponds to the number of electrode fingers, the number of electrode regions for the input and the output electrodes are given by:

$$N_1 = (n+1)/2 \tag{4.18}$$

$$N_1 = (n-1)/2 \tag{4.19}$$

where *n* is mode order. The product of η_1 and η_2 (i.e., input and output electromechanical coupling factors) is given by:

$$\eta_1 \eta_2 = (n^2 - 1)\left(E_p d_{31} w\right)^2 \tag{4.20}$$

Therefore, the parameters values of the equivalent electrical circuit for a two-port rectangular plate resonator vibrating in its nth length-extensional mode are:

$$R_{m=} \frac{\omega_n M_{eq}}{Q \eta^2} = \frac{n}{n^2 - 1} \frac{\pi T_{eq} \sqrt{E_{eq}/\rho_{eq}}}{2 {d_{31}}^2 {E_p}^2 w Q} \quad n = 1,3,5.. \tag{4.21}$$

$$R_{m=} \frac{\omega_n M_{eq}}{Q \eta^2} = \frac{1}{n} \frac{\pi T_{eq} \sqrt{E_{eq}/\rho_{eq}}}{2 {d_{31}}^2 {E_p}^2 w Q} \quad n = 2,4,6.. \tag{4.22}$$

$$L_{m=} \frac{M_{eq}}{\eta^2} \tag{4.23}$$

$$C_m = \frac{\eta^2}{\omega_n^2 M_{eq}} \tag{4.24}$$

Equations (4.21) and (4.22) are particularly interesting because the motional resistance of a plate resonator vibrating along its length is independent of the resonance frequency of the device. Moreover, the motional resistance of a plate resonator decreases by a factor directly proportional to $1/n$, meaning that devices operating at higher order modes exhibit a lower motional resistance. This distinctive characteristic will be used later on in the design of piezoelectrically-transduced filters with low motional resistance operating in the UHF range.

4.4 Experimental Results

The fabricated contour-mode micromechanical resonators were tested by a Cascade RF probe station in air at atmospheric pressure and ambient temperature. The scattering parameters (S-Parameters) of the devices are extracted directly using an Agilent E5071B vector network analyzer. A Short-Open-Load-Thru (SOLT) calibration procedure was implemented to de-embed the effects of the probes, the cables and other errors introduced by the vector network analyzer.

Figure 4.12 shows the frequency response for a ZnO-on-SOI resonator operating in the 5^{th} order length-extensional mode at 247.3 MHz. Even though this resonator was composed of 20 μm-thick silicon device layer, it still exhibited a motional resistance of only 277 Ω along with an unloaded quality factor of 3,267 in air. Ideally, if the device would have been made entirely of single crystalline silicon, the resonance frequency would be 266.92 MHz by assuming an acoustic velocity of 8,451 m/s. However, because part of the resonator body is made of ZnO piezoelectric transducer layer and the platinum electrodes, the loading effect introduced by these layers shifted down the resonance frequency. By taking this effect into account in combination with Equations (4.5) and (4.6), the equivalent acoustic velocity of the ZnO-on-SOI resonator is 7,965 m/s, which results in a theoretically-predicted resonance frequency of 248.9 MHz at the corresponding 5^{th} resonance mode.

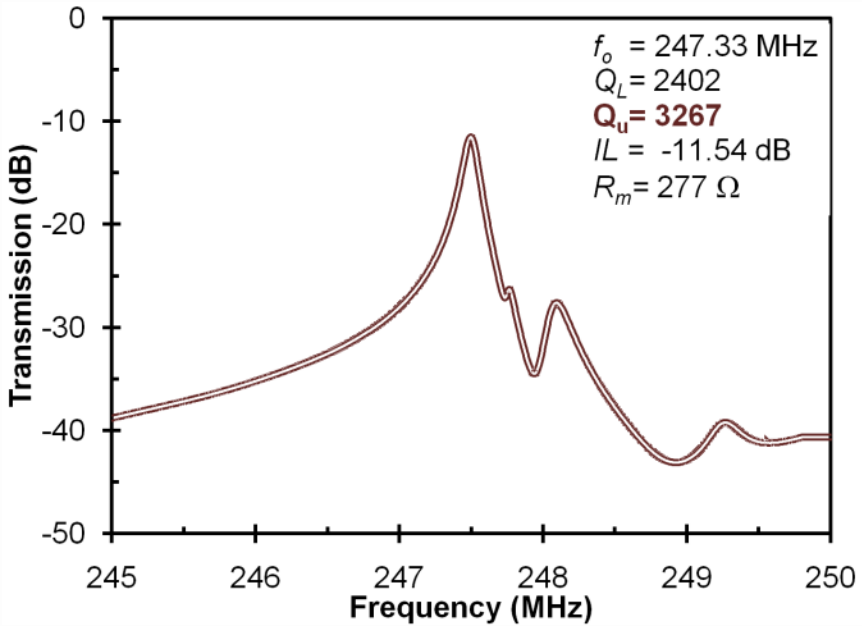

Figure 4.12 – Frequency response of a 5th order ZnO-on-silicon resonator with a 16 µm finger pitch and resonator dimensions of 80 µm x 320 µm

Figure 4.13 shows shows the frequency response for a similar device, which is fabricated in SOI wafer with a 5 µm-thick silicon device layer. As expected, the quality factor of this device is slightly lower compared with the one with a 20 µm-thick silicon device layer (Figure 4.12). Apparently, for the case of rectangular plate resonators, a thicker device layer results in a higher quality factor. However, this is only true for devices at lower frequencies (e.g., below 500 MHz). For high frequency devices operating in their in-plane contour modes, the thickness of the resonator body should be kept below the acoustic wavelength.

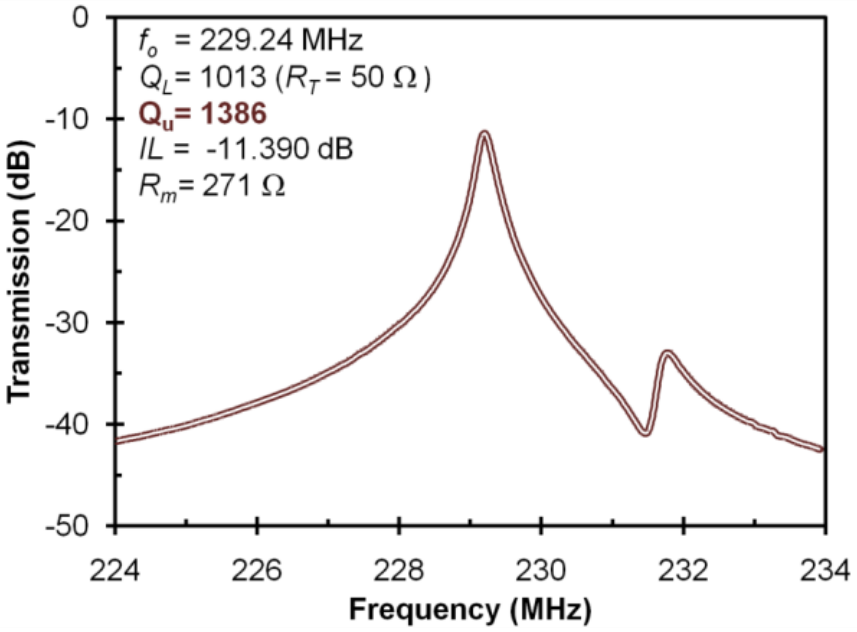

Figure 4.13 – Frequency response of a 5th order ZnO-on-silicon resonator with a 16 µm finger pitch and resonator dimensions of 80 µm x 170 µm

A higher resonance frequency can be achieved by retaining the length of the rectangular plate while reducing the finger pitch size of the top electrode. Figure 4.14 shows the frequency response for 9th order ZnO-on-silicon resonator. The measured center frequency is at 440.5 MHz with an unloaded Q of 5,335 in the air. The motional impedance of the resonator is 140 Ω which makes it a very attractive candidate as the tank circuit for implementation of a reference oscillator. The dimension for this device is 80 µm × 200 µm. As can be observed, this device has the same length as the one presented in Figure 4.14, but the top interdigitated electrode is composed of nine fingers instead of five. The width of the device also has been adjusted in order to attenuate a spurious mode adjacent to the desired resonance frequency. Additionally, as the resonator has been actuated in its higher order mode, the motional resistance is anticipated to be reduced, compensating for the lower electromechanical coupling. As shown in Figure 4.14, the unloaded quality factor of this device operating in the air is 5,335, which is on

par with the quality factor reported for capacitively-transduced counterparts made solely of low acoustic loss silicon in a similar frequency range [58].

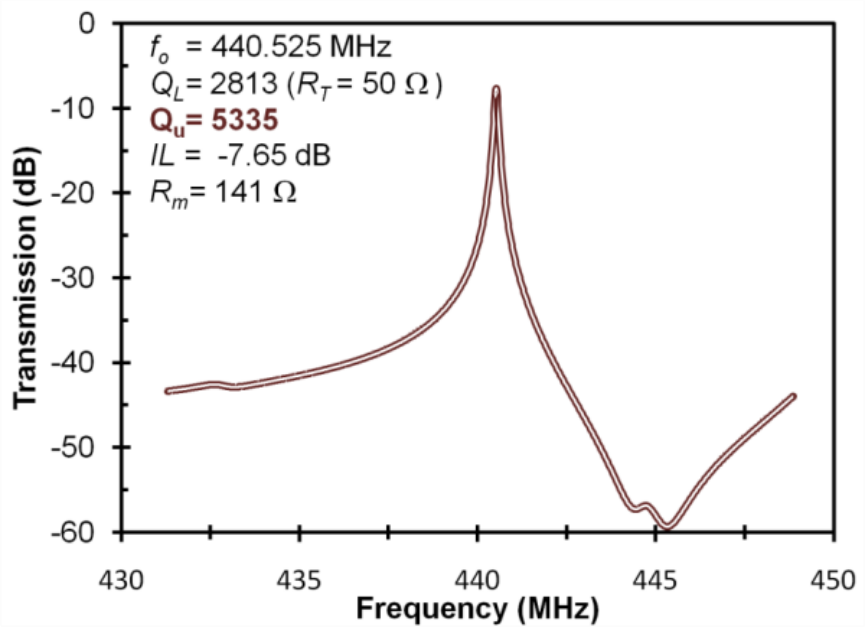

(a)

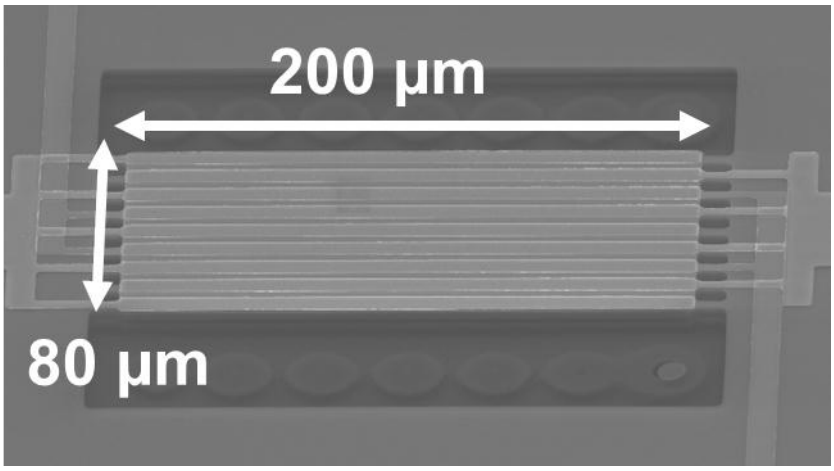

(b)

Figure 4.14 – (a) Frequency response of a 9th order ZnO-on-SOI rectangular plate resonator with a 8.88 µm finger pitch and resonator dimensions of 80 µm x 200 µm; and (b) SEM micrograph of the fabricated ZnO-on-SOI rectangular plate resonator

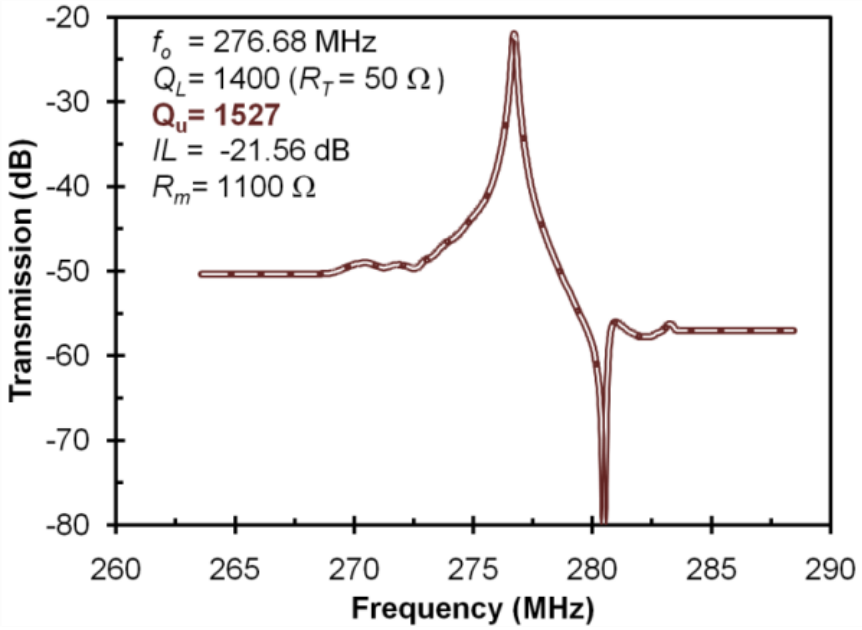

(a)

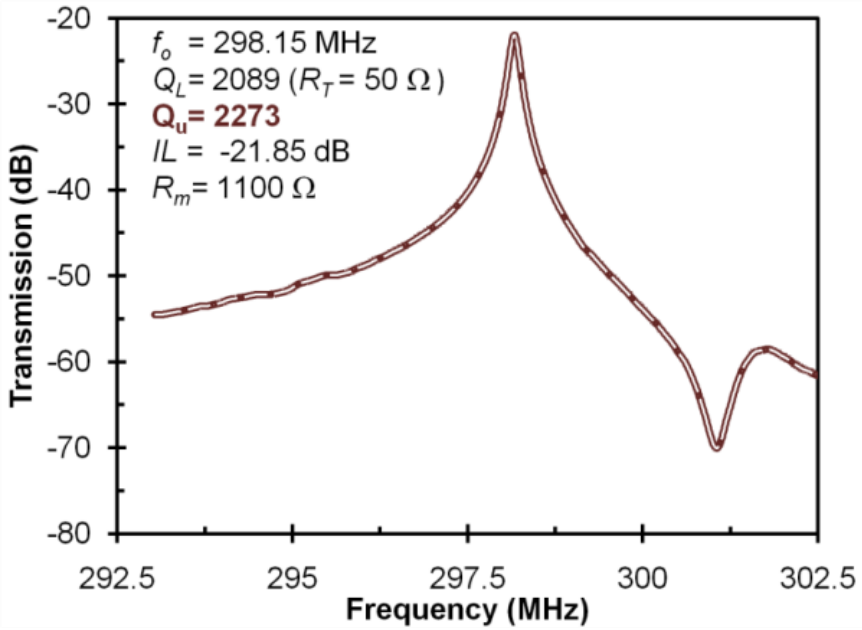

(b)

Figure 4.15 – Frequency responses for two identically-sized piezo-on-silicon resonators with 200 µm × 100 µm dimensions (a) operating in the 14th order length-extensional mode; and (b) operating in the 15th order length-extensional mode

It is worth mentioning that higher resonance mode does not necessary translate to higher frequency. The dimension that set the resonance frequency for a piezoelectrically-transduced resonator with interdigitated top electrode is the finger pitch size, which is given by the ratio between length of the resonator plate and the order of the length-extensional mode. Figure 4.15 shows the frequency responses for two identically-sized ZnO-on-silicon resonators composed of a 20 μm-thick silicon device layer operating in its 14^{th} and 15^{th} order length-extensional modes. Despite the fact the resonator operates in a higher order mode, the resonance frequency and quality factor are comparably lower than the one presented in Figure 4.14. The lower resonance frequencies for this device can be attributed to the relatively larger electrode finger pitch size of 14.28 μm and 13.33 μm, for the 14^{th} and 15^{th} resonance mode, respectively. With regard to the quality factor, it relates strongly to the length to width ratio of the rectangular plate aside from its dependence on the anchor design. Although the finite element modal analyses can easily predict the resonance frequency and the mode shape for each resonator design, there are no existing simulation packages capable of correctly predicting the *Q* of these microresonators. It is widely believed that the quality factor is predominantly limited by the anchor losses rather than the other energy dissipations such as internal damping, viscous gas damping, and thermoelastic damping. Nevertheless, for a given resonator design, the major intensity of the strain field determined by the modal analysis simulation is a strong indication that the device is anticipated to exhibit a large quality factor.

Figure 4.16 presents the frequency response for a piezo-on-silicon resonator operating in its 13^{th} resonance mode at 868.4 MHz. The dimension of this rectangular plate resonator is 60 μm × 120 μm. the theoretically calculated resonance frequency is

862.87 MHz with an effective acoustic velocity of 7,965 m/s for the ZnO-on-silicon stacked-layers. The predicted resonance frequency is in very close agreement with the measurement result. Moreover, the theoretically-predicted motional resistance is 1,336 kΩ, which is also on par with the measured value.

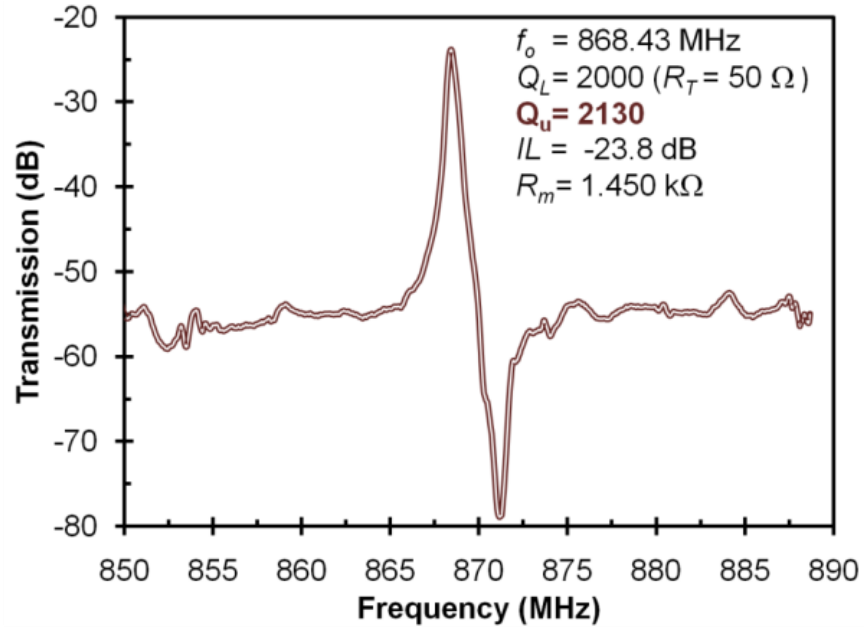

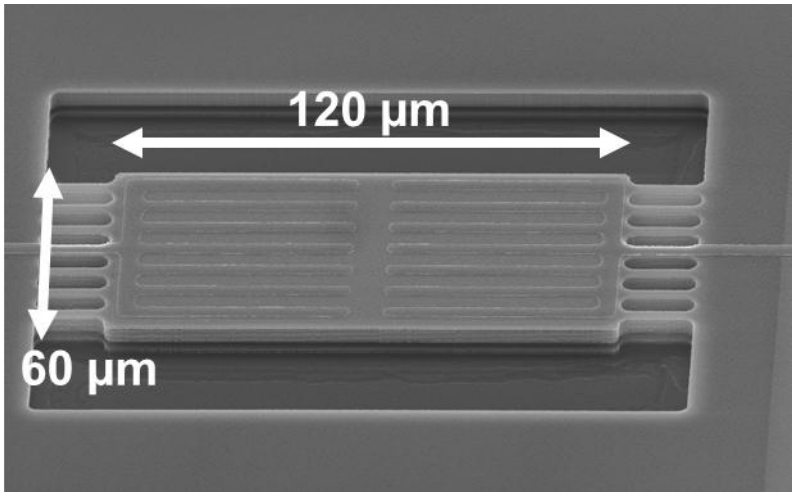

Figure 4.16 – Frequency response for ZnO-on-SOI resonator operating at 868.43 MHz and the SEM micrograph of the fabricated device

It should be emphasized that devices based on capacitively-transduced silicon bulk acoustic-wave resonators have been demonstrated with resonance frequencies up to 1.55 GHz along with quality factors on the order of 3,000 [59] . However, they required a large actuation voltage in the range of 50 V to obtain a motional resistance in the order of 30 kΩ, which makes it challenging to integrate them directly with 50 Ω electronics. With regard to the capacitively-transduced contour-mode disk resonators, they also suffer from their large motional resistance on the order of ~ 100 kΩ at gigahertz frequencies, which in some cases prevent direct measurement of the resonator response without the use of a highly-specialized mixing measurement technique [60].

In general, despite the slightly lower quality factor of piezoelectrically-transduced resonators, they do not require a polarization or bias voltage to operate while exhibiting characteristic motional resistance typically lower than 1 kΩ. These two unique advantages make the piezoelectrically-transduced contour-mode resonators very attractive for implementation of RF-front end subsystems such as filters and oscillators at gigahertz frequencies.

Chapter 5

Micromechanical Filters Based on Piezoelectric Resonators

During the past two decades, the demand for bandpass filters operating in the VHF and UHF ranges have increased significantly. Filters with high selectivity, low insertion loss, excellent out-of-band rejection, small size, and standard IC process compatibility are an enabling technology for the next generation of multiband and multimode wireless communication transceivers. The current state-of-the-art RF filters predominantly employ surfaces acoustic wave (SAW) resonators or bulk acoustic wave (BAW) resonators, which are both relatively small in size. However, SAW devices have low quality factors (*Q*'s~ 200-1,000), which affect ultimately the minimum attainable insertion loss, especially for filters with fractional bandwidth less than 1%. Moreover, SAW filter technology is deemed IC compatible. Filters based on thin film bulk acoustic wave resonators (FBAR's) exhibit *Q's* up to 1,000 with low insertion loss at gigahertz frequencies. Nevertheless, the monolithic integration of FBAR's with RFIC circuits have been delayed due that their operation frequency is set by the thickness of piezoelectric film, thus impeding the implementation of multi-frequency filters within a single RFIC chip. At the moment, filters and oscillators based on the SAW and FBAR technologies are utilized as off-chip components that must be interfaced with electronics at the board level to occupy a sizable portion of current wireless transceivers, thereby imposing a bottleneck against the ultimate miniaturization and portability of the future wireless communication devices.

As an emerging technology, filters and oscillators based on micromechanical contour-mode resonators have become a promising on-chip alternative to the aforementioned technologies. Efforts have been focused upon strategies for the design and implementation of micromechanical filters capable of replacing the current dominant SAW and FBAR technologies without sacrificing the overall performance, but at the same time reducing size, fabrication cost and allowing the direct monolithic integration with 50 Ω IC electronics.

This chapter details the design, implementation and characterization of piezoelectrically-transduced MEMS filters based upon contour-mode micromechanical resonators. Three different filter synthesis techniques based on mechanically coupled, electrically coupled and acoustically coupled resonator filters have been concurrently explored. The filters were designed and implanted to operate at frequencies ranging from 50 MHz to 900 MHz while exhibiting insertion losses as low as 2 dB with filter termination resistances as low as 300 Ω. Moreover, the fabricated filters can be seamlessly integrated with 50 Ω electronics by the proper design of LC impedance matching networks similar to SAW filters. In addition, a new methodology for increasing the order of a filter based on mechanically-coupled resonators while reducing the total number of constituent resonators has also been explored.

5.1 Mechanically-Coupled Resonators

The use of high-*Q* contour-mode micromechanical resonators, whose frequencies are set by their lithographically defined lateral dimensions, permits the synthesis of filters at multiple target frequencies on a single chip. Filters synthesized using mechanically-coupled contour-mode resonators or resonator arrays are capable of obtaining wider

bandwidth than electrically coupled ladder filters, without the use of external tuning components or post-fabrication frequency trimming. This section presents the design and measurement results of RF filters based on mechanically-coupled piezoelectrically-transduced resonators.

5.1.1 Device Operation

The working principle of a mechanically-coupled bandpass filter is illustrated in Figure 5.1(a) - (d), which shows the mode shapes, frequency response and equivalent circuit model for a filter composed of two contour-mode resonators mechanically coupled by a longitudinal beam. In this coupled mechanical system, there are two types of modal vibrations. In the first low-frequency mode, both resonators move in phase while stretching and compressing the coupling beam. In the second high-frequency mode, the two resonators move out-of-phase, thus leaving the coupling beam almost unstressed. The filter passband is determined by the frequency difference between the aforementioned modes as shown in Figure 5.1(c). The simplified equivalent circuit is shown in Figure 5.1(d), where the mass-spring-damper parameters represented as series LCR tanks model the mechanical response of the individual resonator and the spring constants represented by the t-network capacitors model the mechanical coupling beam between the constituent resonators. Moreover, η_i and η_o represent the electromechanical coupling coefficient between the mechanical filter and the electrical input and output terminals whose port capacitances equal to C_o.

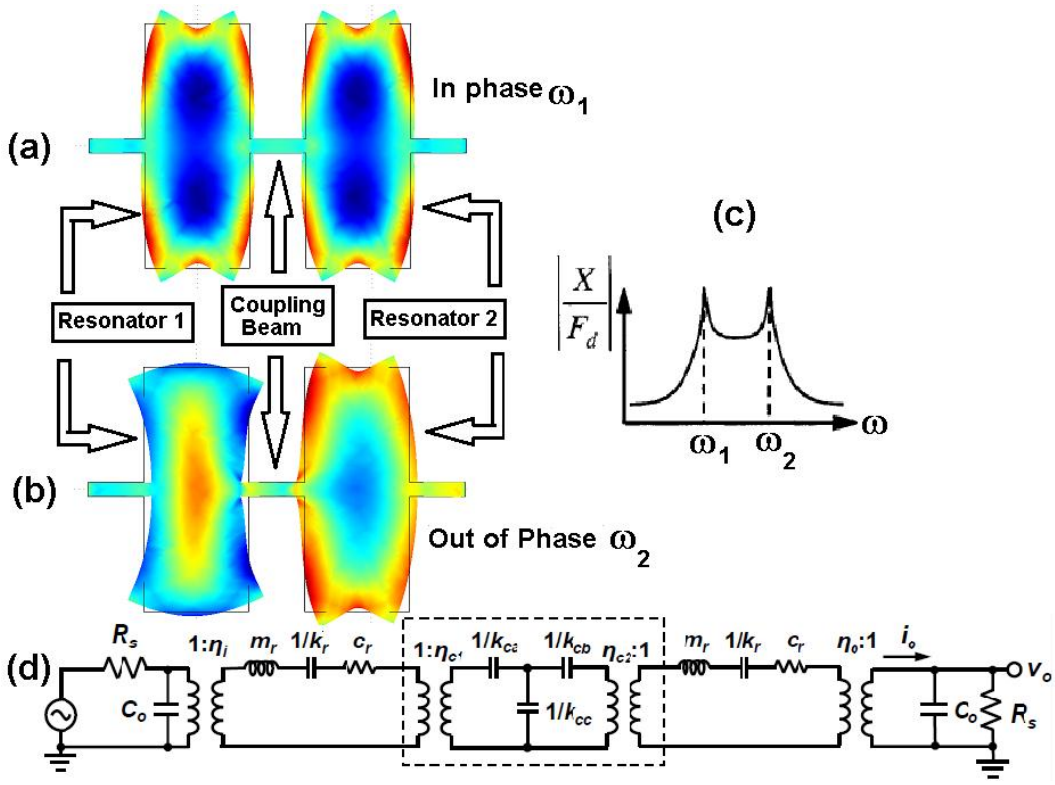

Figure 5.1 – Illustration of the working principle for a mechanically-coupled resonator filter vibrating in (a) in-phase mode; (b) out-of-phase mode; with (c) predicted bandpass frequency characteristic; and (d) electrical equivalent circuit model

The center frequency of the filter is determined by the common resonance frequency of the constituent resonators, and the filter bandwidth is designed by adjusting the equivalent stiffness ratio between the resonator and the coupling beam. The resonance frequency and equivalent stiffness at the coupling location of each the resonator depends on its physical dimensions, its geometry (e.g., disk, ring, rectangular plates, etc.), and its mode shape. For instance, a mechanical resonator exhibits the highest equivalent stiffness at its nodal location when vibrating in a certain mode shape. As a result, a filter with narrower bandwidth can be synthesized by positioning the coupling beam closer to the nodal location.

5.1.2 Coupling Beam Design

The bandwidth of a mechanically-coupled two-pole filter is proportional to the ratio of the coupling beam stiffness k_s to the resonator stiffness k_r at the coupling location, which is given by:

$$BW = \frac{k_s}{k_r} k_{12} \tag{5.1}$$

where k_{12} is the normalized coupling coefficient between resonators tanks for a given filter type [61]. In this work type I Chebyshev filter was chosen along with the corresponding coupling coefficient k_{12}. As mentioned in the previous section, the stiffness of the resonator at the coupling location can be calculated as a function of its equivalent mass and resonance frequency. For the coupling beam, its stiffness can be modeled as an acoustic transmission line. Figure 5.2(a) and (b) shows the schematic of an extensional-mode coupling beam with dimensions of w_c (width), T_c (thickness), and l_c (length) and its equivalent transmission line π-model.

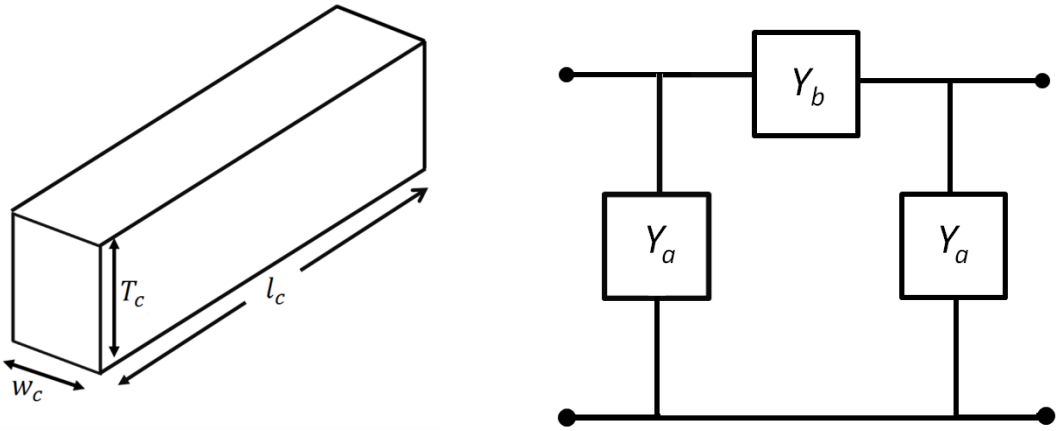

(a) (b)

Figure 5.2 – (a) Extensional-mode coupling beam with its physical dimensions; and (b) its equivalent transmission line π-model representation

The value of the acoustic impedances Y_b and Y_a in Figure 5.2(b) are functions of the material properties and coupling beam dimensions given by [42]:

$$Z_0 = \frac{1}{w_c T_c \sqrt{\rho E}} \tag{5.2}$$

$$\alpha = 2\pi f_0 \sqrt{\frac{\rho}{E}} \tag{5.3}$$

$$Y_b = \frac{-j}{Z_o \sin \alpha l} \tag{5.4}$$

$$Y_a = \frac{-j \tan(\alpha l/2)}{Z_o} \tag{5.5}$$

where E and ρ are the Young's modulus and the material density of the coupling beam, respectively, while f_o is the resonance frequency. From Figure 5.1(b), the transformers turn ratios associated with the coupling beam, ηc_1 and ηc_2, model the mechanical impedance transformation realized by coupling one resonator to the other. Ideally, if the coupling beam is connected at the same location of both constituent resonators, the values for ηc_1 and ηc_2 are equal to one, which means that all the mechanical energy is transferred by the coupling beam between the resonators.

Two especial cases are particularly interesting. Under the first scenario, the length of the coupling beam is equal to half of the wavelength ($\lambda/2$), then the composite resonator array behaves as a single resonator with a resonance frequency equal to that of its constituent resonator. Under the second scenario, when the length of the coupling beam is equal to quarter of the wavelength ($\lambda/4$), the composite array behaves as a coupled resonator filter, with the bandwidth of the passband given by Equation (5.1). Even though the effect of a coupling beam with any specific length on the frequency response of the filter can be modeled by Equations (5.2)-(5.5), it is preferable to use $\lambda/4$-

long coupling beam(s) while changing the width of the beam in order to adjust the bandwidth of the filter. It is worth mentioning that the resonators and the coupling beam(s) usually have the same thickness, therefore the thickness parameter does not affect the ratio of the coupling beam stiffness k_s to the resonator stiffness k_r, which determines the filter bandwidth. The electrical equivalent circuit for a mechanically-coupled piezoelectric resonator filter consists of two identical resonator coupled by a longitudinal extensional beam modeled as π-network capacitors shown in Figure 5.3.

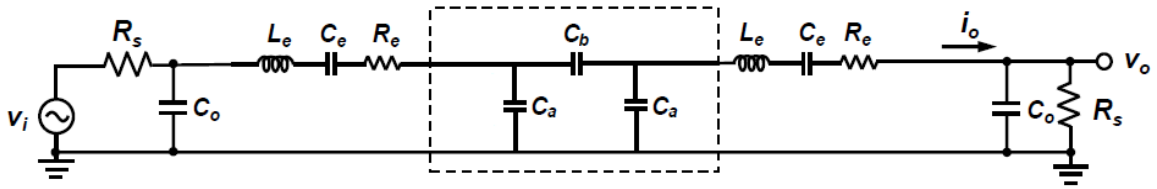

Figure 5.3 – Electrical model for a micromechanical filter composed of two identical coupled resonators

In order to illustrate the behavior of a mechanically-coupled two-pole resonator filter, a finite-element simulation of the frequency response of mechanical filter with two mechanically-coupled and identically-sized 30 μm-radius piezoelectrically-transduced disk resonators has been performed. The parameters for the simulation have been calculated based on the equations presented in Section 4.1. The resonator is made of a 500 nm-thick ZnO layer, embedded between 150 nm-thick Pt bottom and top electrodes. The values for the parameters of the equivalent electrical model are summarized in Table 5.1.

Table 5.1 – Equivalent electrical circuit parameters for a mechanically-coupled filter with different coupling beam lengths

Parameter	$\lambda/4$	$\lambda/3$	$\lambda/2$
R_{eq}	1.47 kΩ	1.47 kΩ	1.47 kΩ
C_{eq}	2.5923 fF	2.5923 fF	2.5923 fF
L_{eq}	5.6569 mH	5.6569 mH	5.6569 mH
Q	1,000	1,000	1,000
f_0	41.513 MHz	41.513 MHz	41.513 MHz
C_a	0.1182 pF	0.2070 pF	-11.654 pF
C_b	- 0.1182 pF	-0.1370 pF	5.827 pF

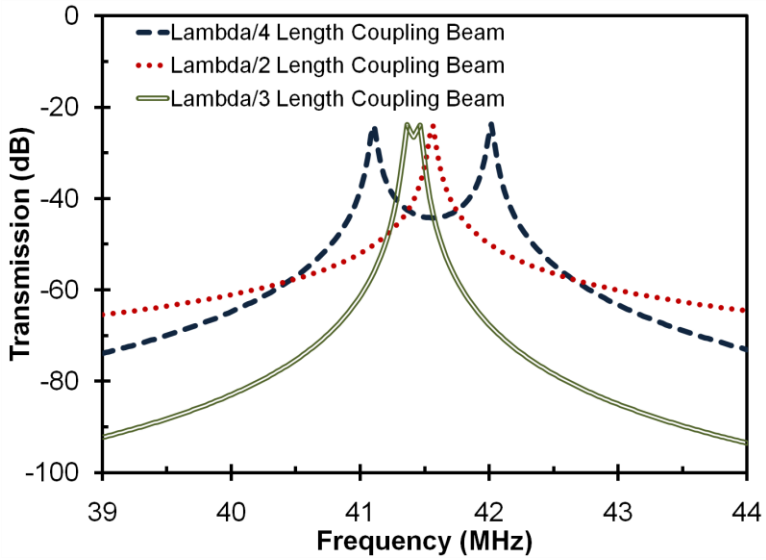

Figure 5.4 – Frequency response for a mechanically-coupled filter with different coupling beam lengths

As expected for the case in which the coupling beam length is equal to $\lambda/2$, the coupled system behaves like a single resonator. When the length of coupling beam is equal to $\lambda/4$ the system behaves as a filter with its bandwidth defined by the Equation (5.1). However, when the length of the coupling beam is equal to $\lambda/3$, the coupled resonator array still behaves as a filter, but the design of the coupling beam affects the center frequency and the bandwidth of the synthesized filter. Nevertheless, this behavior can be accurately modeled, and potentially may be beneficial when the fabrication

process tolerance limits the minimum achievable width of the coupling beams. It is worth mentioning that the purpose of the simulation results presented in Figure 5.4 is to show the frequency responses (especially the bandwidth) of a pair of mechanically-coupled resonators with a variety of coupling beam length, but these coupled resonator filters have not been properly terminated as the termination resistance has been set to 50 Ω. Also for simplicity, the feedthrough capacitance and the device input/output capacitances have not been included in the simulation. Later on, the effect on the frequency response and the termination resistance of the filter introduced by these capacitances will be further explained.

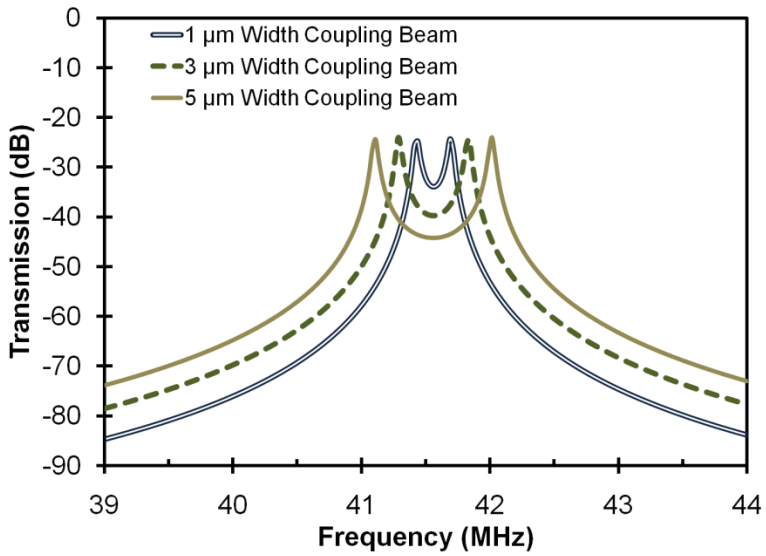

Figure 5.5 – Frequency response for a micromechanical filter with different coupling beam widths

As mentioned earlier, the bandwidth of a mechanically-coupled filter can be designed by changing the stiffness of the coupling beam. If the length is set equal to $\lambda/4$, the only parameter that can be changed via CAD layout is the width of the coupling beam. To illustrate this concept, Figure 5.5 shows the finite element simulation results for

a mechanically-coupled filter consisted of two identical 30 μm-radius piezoelectrically-transduced disk resonators coupled via a $\lambda/4$ beam with different widths.

Table 5.2 – Equivalent electrical circuit parameters for a mechanically-coupled two-pole resonator filter with different coupling beam width

Parameter	$\lambda/4$ (1μm-wide)	$\lambda/4$ (3μm-wide)	$\lambda/4$ (5μm-wide)
R_{eq}	1.47 kΩ	1.47 kΩ	1.47 kΩ
C_{eq}	2.5923 fF	2.5923 fF	2.5923 fF
L_{eq}	5.6569 mH	5.6569 mH	5.6569 mH
Q	1,000	1,000	1,000
f_0	41.513 MHz	41.513 MHz	41.513 MHz
C_a	396.1 fF	118.2 fF	198.1 fF
C_b	- 396.1 fF	- 118.2 fF	198.1 fF

Compared with conventionally cascaded ladder filters based on FBAR resonators, it is advantageous to be able to synthesize the filter bandwidth by changing a physical dimension (i.e. width of the coupling beam) that can be accurately designed by the CAD layout. Ideally, the width of the beam can be selected upon the desired filter bandwidth. However, the minimum beam width of the beam is set by the lowest achievable resolution by the fabrication technology, and its upper limit is set at the point where the coupling beam is so wide that it starts to considerably distort the frequency response of the synthesized filter and lower its quality factor.

5.1.3 Termination Resistance

Having determined the effect of the coupling beam on the bandwidth of a mechanically-coupled resonator filter, the effect of the termination resistance must be also explained. The frequency response of the filter shown in Figure 5.5 has a jagged passband and unacceptable insertion loss. This is due to the mismatch between the characteristic motional resistance of the coupled constituent resonators and the filter

termination impedance. To smooth the passband and reduce the insertion loss, a termination resistance is needed to load the quality factor of the constituent resonator to a value equal to $q_i Q_{filter}$, where Q_{filter} is the quality factor of the filter, and q_i is a normalized "q" value obtained from a filter design handbook [62]. The value of the termination resistance is given by [63]:

$$R_T = R_{res}\left(\frac{Q_{res}}{q_i Q_{filter}} - 1\right) \tag{5.6}$$

where Q_{res} is the quality factor of the constituent resonator. With the filter properly terminated at both input and output ports, the insertion loss can be defined as:

$$IL = 20Log_{10}\left(\frac{2R_T}{2R_T + R_{filter}}\right) \tag{5.7}$$

It is clear from Equation (5.7) that a large motional resistance of the constituent resonator demands a large termination resistance. It is demonstrated by Pozar [64] that values of the termination resistance larger than 5 kΩ cannot be matched using on-chip passive components such as inductors and capacitors.

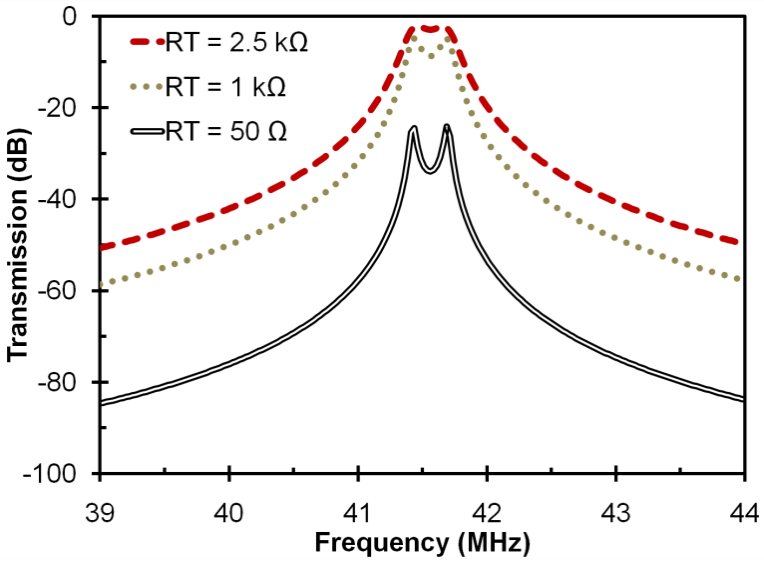

Figure 5.6 – Frequency response for a mechanically-coupled two-pole filter terminated with termination resistors of different values

Figure 5.6 shows the frequency response for a mechanically-coupled resonator filter consisting of two identical 30 μm-radius disks operating in the fundamental radial contour-mode, terminated with 50 Ω, 1 kΩ and 2 kΩ resistors. As can be seen, the termination resistance R_T affects the frequency passband and the out-of-band rejection of the filter, which must be jointly considered in the order to satisfy the filter specifications (i.e. insertion loss, ripple within passband and out-of-band rejection) for a certain communication standard. The most effective way to reduce the termination resistance is to improve the electromechanical coupling of the constituent resonators. This can be done by increasing the quality factor of the resonator or increasing its piezoelectric transducer surface area. If the transducer size is increased, the radius of the disk resonator must also be increased, but this will reduce the resonance frequency. If the quality factor is increased, carefully consideration must be taken to retain the bandwidth of the filter. Consequently, filters with relatively large bandwidth and composed of high-*Q* resonators, require a large termination resistance. The advantage of a high *Q* does not translate necessarily to a lower termination resistance for a filter with a large bandwidth (e.g., > 2%). In the subsequent section, a method for reducing the value of the termination resistance without compromising filter performance will be discussed.

5.1.4 Filter Termination using L-Matching Network

The example presented in Figure 5.6 represents the ideal case scenario where the input impedance of the unterminated filter is mostly resistive. In practice, the input impedance of a MEMS filter has a reactive component, which is mainly due to the intrinsic and parasitic capacitances of the constituent resonators. The simplest case for impedance matching would have equal source and load resistances but unequal reactance

(e.g., $Z_S = R_S \pm j0$ and $Z_L = R_L + jX_L$ where $R_S = R_L$).For this case, one added component between source and load having a reactance of $-jX_L$ is all that is required to cancel the load reactance to realize conjugate match. In most cases when $R_S \approx R_L$, the use of a single component can provide acceptable performance without the need to transform the small difference in the reactance.

Nevertheless, the most generic filter termination requires a matching network with a minimum of two reactive components. This matching network has four possible arrangements that consist of one capacitor and one inductor as shown in Figure 5.7. In all four cases, the resistive part of the impedance adjacent to the shunt element must be higher than the resistance of the other impedance. In different terms, $R_L > R_S$ for configurations shown in (a) and (c), whereas $R_S > R_L$ for the topologies shown in (b) and (d). With respect to the MEMS filters developed in the present work, the value of source impedance *Rs* is 50 Ω and the value of the load impedance is given by the form $Z_L = R_L - jX_L$, where $R_L > R_S$. Therefore, only L-matching networks based on configuration (a) and (c) can be used to match those filters to a 50 Ω source and termination impedance.

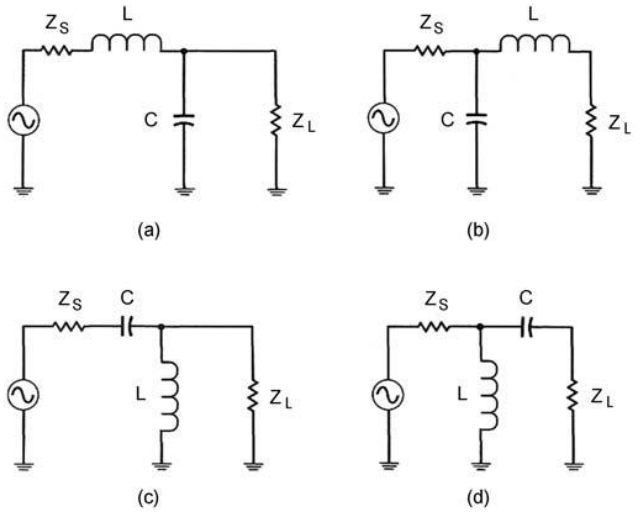

Figure 5.7 – Four possible L-matching network topologies for MEMS filters [64]

The values of the passive components for the case when $Z_L = R_L + jX_L$, and $R_L > R_S$ can be calculated by following the procedure presented by [64]. The effective impedance by looking into the matching circuit followed by the load impedance must be equal to Z_S to realize an impedance matching condition:

$$Z_S = jX + \frac{1}{jB + 1/(R_L + jX_L)} \tag{5.8}$$

where B and X represented the shunt and the series passive components in Figure 5.7 (a) and (c). By rearranging the real and imaginary parts separately, two equations with the two unknown variables B and X can be derived as follows:

$$B(XR_L - X_L Z_S) = R_L - Z_S \tag{5.9}$$

$$X(1 - BX_L) = BZ_S R_L - X_L \tag{5.10}$$

Solving (5.9) for X and substituting it into Equation (5.10) gives a quadratic equation for B. The solution is given by:

$$B = \frac{X_L \pm \sqrt{R_L/Z_S}\sqrt{R_L^2 + X_L^2 - Z_S R_L}}{R_L^2 + X_L^2} \tag{5.11}$$

Since $R_L > Z_S$ the argument of the second square root is always positive, then the series reactance can be found as:

$$X = \frac{1}{B} + \frac{X_L Z_S}{R_L} - \frac{Z_S}{BR_L} \tag{5.12}$$

It is clear from Equation (5.11) that two solutions are possible for B and X. Both solutions are physically realizable, since both positive and negative values of B and X are viable. Basically, positive X represents an inductor and negative X can be achieved by a capacitor, while positive B implies a capacitor, and negative B represents an inductor. As mentioned previously, for the case when $R_L > R_S$, both topologies (a) and (c) in Figure 5.7 can be implemented. The selection of one particular solution may result in significantly

smaller values for the capacitors and inductors. Additional consideration for the preferred solution may relate to the wider bandwidth of the matching circuit, and the lower standing wave ratio on the line between the matching network and the load [64]. For filters with percentage bandwidth less than 5%, the criteria for designing a LC impedance-matching network would rely mainly on the commercially available capacitor and inductor components.

To analyze the effect of the different matching circuit topologies on the filter characteristic, the mechanically-coupled resonator filter with equivalent circuit model presented in Table 5.2 along with λ/4-long and 1 μm-thick coupling beam will be employed for a case study. Both solution for topologies shown in Figure 5.7 (a) and (c) provide the same matching bandwidth and insertion loss (i.e., *IL*=2.29 dB, *BW*=1%). The values for the passive components are calculated using Equations (5.11) and (5.12). For the configuration shown in Figure 5.7(a) the values of the shunt capacitor and the series inductor are 13.88 pF and 1.02 μH, respectively. For the configuration as seen in Figure 5.7 (c), the value of the shunt inductor and series capacitor are 1.06 μH and 14.37 pF, respectively. As compared to the same filter terminated by a resistor, the performance of the LC-terminated filter is substantially better especially in terms of the out-of-band rejection. Moreover, the matching circuit behaves as a filter by itself, therefore it provides additional advantage such as better attenuation of spurious modes (i.e., unwanted resonance peaks) and improved isolation for noise at frequencies lower than the passband of the filter as shown in Figure 5.8.

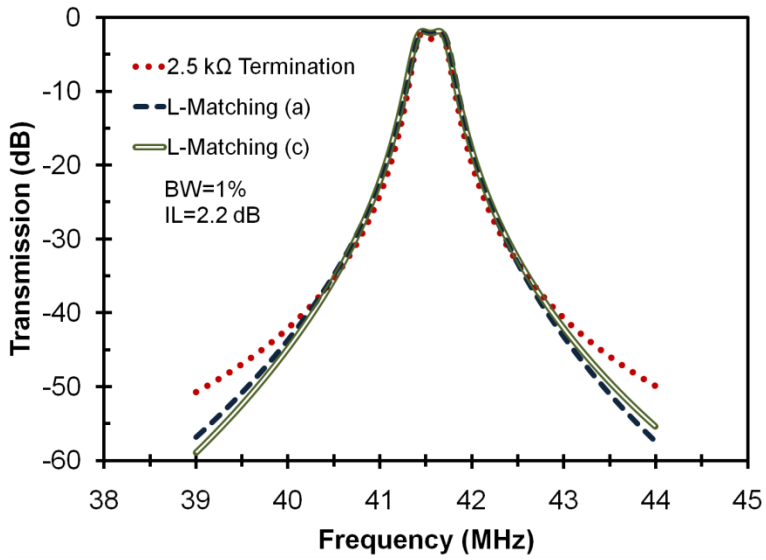

Figure 5.8 – Simulated frequency responses for a micromechanical two-pole filter with three different matching network designs, two of which are based on topologies shown in Figure 5.7(a) and (c)

5.1.5 The Effect of the Substrate Parasitics on the Frequency Response

When a resonator or filter operates away from its resonance frequency, it behaves as an open circuit with the overall electrical equivalent circuit given by Figure 5.9. Thus, the out-of-band rejection can derived as:

$$Rej[dB] = -20log_{10}\left(\frac{C_f}{C_o}\right) - IL \tag{5.13}$$

where C_f represents feedthrough capacitance that is determined by the feedthrough current between the input and the output port mostly through the substrate itself, while C_o is defined as the intrinsic capacitance at the resonator input and output terminals together with the capacitance of the probing pads.

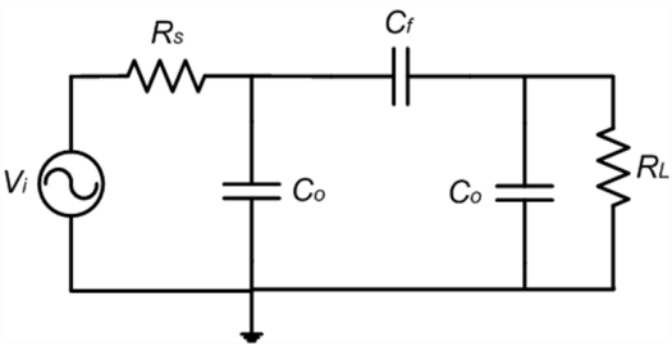

Figure 5.9 – Equivalent circuit for off-resonance response of a micromechanical filter that includes substrate effects for the calculation of the out-of-band rejection

Figure 5.10 presents the simulated frequency responses of a filter with different values of C_o. The parameters of the equivalent electrical circuit of the filter are listed in Table 5.2. In the simulation, the termination resistance was retained to be 2.5 kΩ and the intrinsic port capacitance of the constituent resonator has been varied between 0 to 1 pF. As expected, as C_o increases, the insertion loss of the filter also increases. Since part of the RF signal is diverted towards C_o, there is less electrical energy to be converted into mechanical energy, which ultimately results in the extra insertion loss of the filter. As can be observed in Figure 5.10, the filter insertion loss was not significantly affected when C_o=0.2 pF which happens to be its theoretical value for a piezoelectric resonator device with the specifications presented Table 5.1. As compared to the ideal scenario when C_o=0 pF, the insertion loss increases substantially from 2 dB to 5 dB for C_o=1 pF. Moreover, the ripple in the passband increases from 0.5 dB to 5 dB. This is because the termination impedance could not effectively flatten the passband of the filter when shunt port capacitors C_o are large enough to steer away signals. In different terms, if the equivalent impedance of the shunt port capacitor C_o is comparable to the value of the termination impedance, then a large portion of the signal will not pass through the filter termination

circuits and therefore negatively impacting the effectiveness of the termination circuit. As rule of thumb, the equivalent impedance of the shunt capacitor C_o at the central frequency of the filter should be kept much larger than the value of the termination impedance. However, in some designs of mechanically-coupled filters, the intrinsic port capacitance C_o have relative large value that could not be further reduced. On the contrary, for mechanically-coupled rectangular plate resonators, this parameter can be strategically designed to circumvent its impacts. Nevertheless, there is a trade-off between the device sizes which define both the value of this capacitance and the electromechanical coupling coefficient for piezoelectrically-transduced contour-mode resonators.

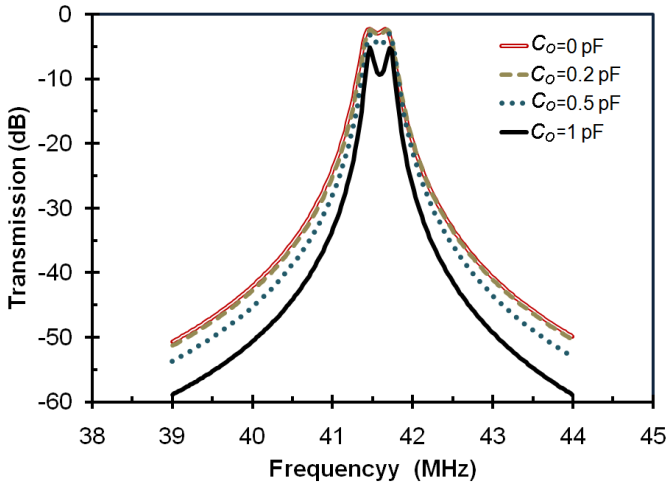

Figure 5.10 – Effect of the port capacitance C_o on the simulated frequency response of a mechanically-coupled filter terminated with a 2.5 kΩ resistance

The out-of-band rejection of a filter is mainly determined by its feedthrough parasitic capacitance C_f, which is largely dependent upon the electrical properties of the carrier substrate. For the piezoelectrically-transduced resonators and filters developed by this work, high-resistivity silicon wafer with resistivity >1 kΩ-cm, and silicon on insulator (SOI) wafers were employed. Figure 5.11 shows the combined effect of C_o and

C_f on the simulated frequency response of a filter with equivalent electrical element values listed in Table 5.2. The termination resistance was set to 2.5 kΩ, the intrinsic capacitance of the constituent resonator was assumed to be C_o= 0.2 pF and the feedthrough capacitance C_f has been varied between form 10 fF to 100 fF. It can be observed from the simulation results that the filter out-of-band refection decreases and the insertion loss increases as a consequence of the increase in C_f, as C_f increases, the value of its equivalent impedance decreases. At some point when the equivalent impedance of C_f is somewhat comparable to the motional resistance of the coupled resonators, thus a major part of the electrical energy would be diverted towards to C_f instead of passing through the actual filter, which ultimately results in an increase of the filter insertion loss. Typical values for the feedthrough capacitance range between 1 fF to 10 fF depending upon the electrical properties of the carrier substrate (e.g., high-resistivity silicon, low-resistivity silicon, SOI wafer, etc.) and the crosstalk isolation features if an approach for three-dimensional substrate impedance engineering is used [65].

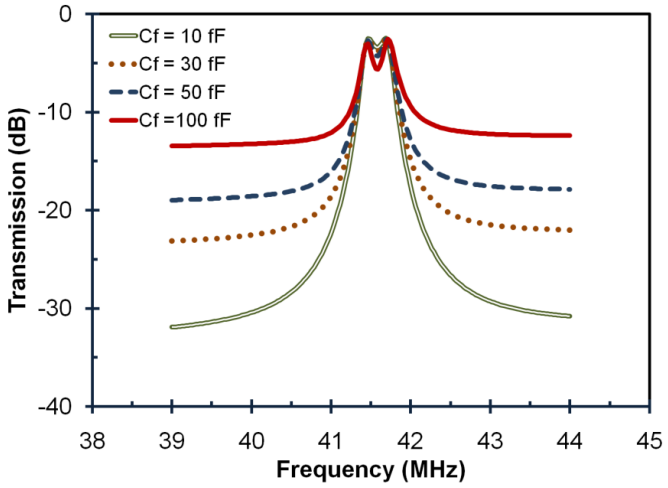

Figure 5.11 – Effect of the feedthrough C_f on the frequency response of a micromechanical filter terminated with a 2.5 kΩ resistance

Figure 5.12 shows the combined effect of C_o and C_f when the filter is terminated with a 2.5 kΩ resistance, and when the filter is coupled to a 50 Ω termination impedance using a L-matching circuit. As was previously mentioned, using a L- matching circuit results in an improvement of 8 dB in the out-band rejection as compared when the filter is terminated with a termination resistance.

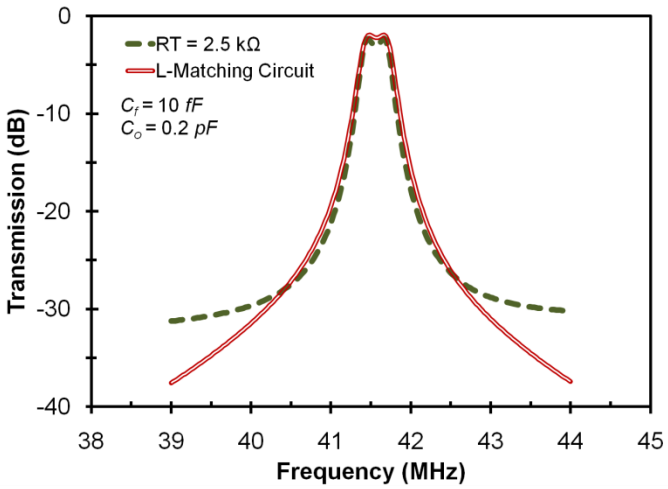

Figure 5.12 – Effect of C_f and C_0 on the frequency response of a mechanically-coupled filter terminated with a 2.5 kΩ resistance or a L-matching network

5.1.6 Fabrication of Piezoelectrically-Transduced Mechanically-Coupled Filters

Arrays of mechanically-coupled contour-mode resonator disk and rectangular plate geometries have been fabricated using the process described in Section 3.3. For instance, the fabricated filters consist of chains of 2, 4, 6, 9 and 20 of 20 µm-radius or 30 µm-radius disk resonators, operating in its 1st and 2nd radial contour-modes.

5.1.7 Experimental Results

The measured frequency response of a mechanically-coupled filter composed of a chain of four mechanically-coupled resonators is presented in Figure 5.13. The filter consists of two 30 µm-radius piezoelectrically-transduced disk resonators connected by a

λ/4 coupling beam. A 700 nm-thick ZnO film was deposited and embedded between 130 nm-thick platinum bottom and top electrodes. Another chain of two mechanically-coupled resonators are electrically connected in parallel in order to reduce the effective motional resistance, thus decreasing termination resistance of the filter. Ideally, the coupling beams were design to be λ/4 in length, however, uncertainties in exact value of the materials properties such as Young's Modulus and residual stress of the film has shifted the central frequency of filter from the expected values predicted from the material properties shown in Table 4.1. The quality factor of each constituent resonator is roughly 800, which is sufficient for synthesizing filters with bandwidth higher than 0.5 % while obtaining low insertion loss < 2.6 dB. The 2 kΩ termination resistor was employed in order to load the quality factor of each constituent resonator and flatten the passband. As compared to standard 50 Ω electronics and testing instruments, the 2 kΩ termination resistor is 40 times larger. One could expect that resonators with higher *Q* can be leveraged to get better filter characteristics. However, given the higher Q of the constituent resonators of such filter would require a larger termination resistance in order to flatten the filter passband as evidenced by Equation (5.6). An alternative solution to this problem would be increase the total number of electrically-coupled resonators in parallel as a single composite resonator. The reduction of the termination resistance will be inversely proportional to number of sub-filters that operates in parallel. Ideally, there is no limit in the number of sub-filters that can be implemented in parallel. However, in a practical filter implementation, the parasitic capacitances (i.e., C_o and C_f) introduced by each additional sub-filter and the chip area constraint would impose an upper limit.

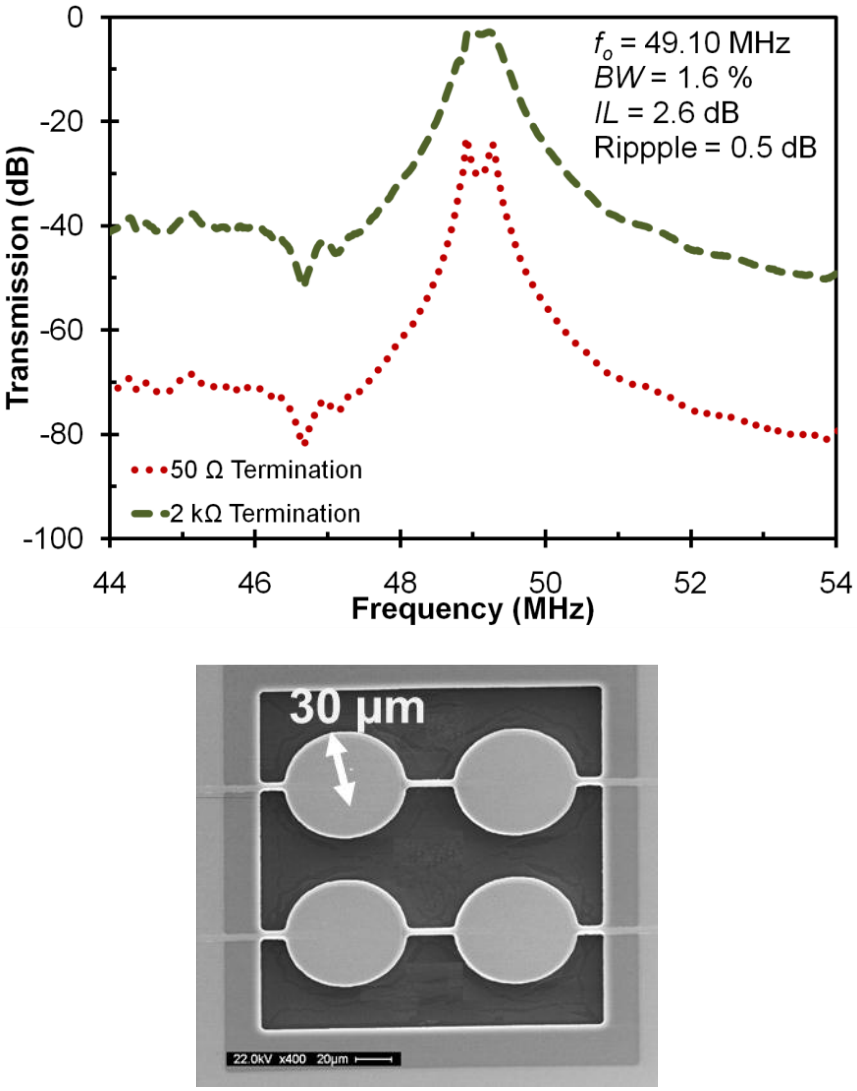

Figure 5.13 – Frequency response for 2×2 micromechanical contour-mode filter with 30-µm radius disk piezoelectric resonators as constituent elements and SEM micrograph of the fabricated filter

The frequency response for a second-order mechanically-coupled filter with four sub-filter chains connected in parallel is shown in Figure 5.14. As can be observed, the termination resistance for this filter is lower as compared to the device with only two sub-filters shown in Figure 5.13. The center frequency of the filter has been shifted up slightly and the bandwidth was increased from 1.3% to 1.6%, which should be attributed to the fabrication variation rather than the addition of a third sub-filter chain. In addition,

the value of the termination resistance was decreased from 2 kΩ to 1 kΩ, which was expected due to the addition of an extra sub-filter. Nevertheless, the motional resistance can be decreased even further if more sub-filter chains are introduced.

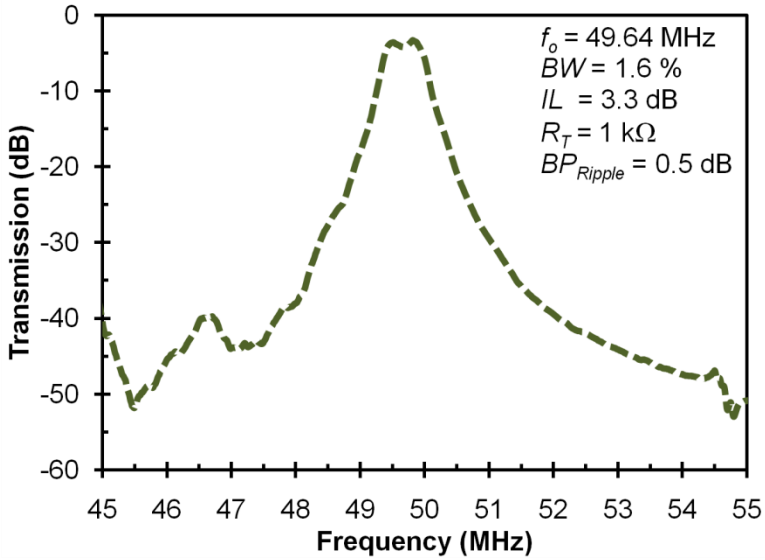

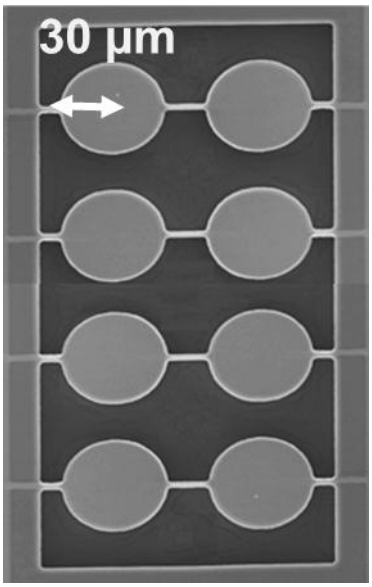

Figure 5.14 – Frequency response for 4×2 micromechanical contour-mode filter with 30-µm radius disk piezoelectric resonators as constituent elements and SEM micrograph of the fabricated filter

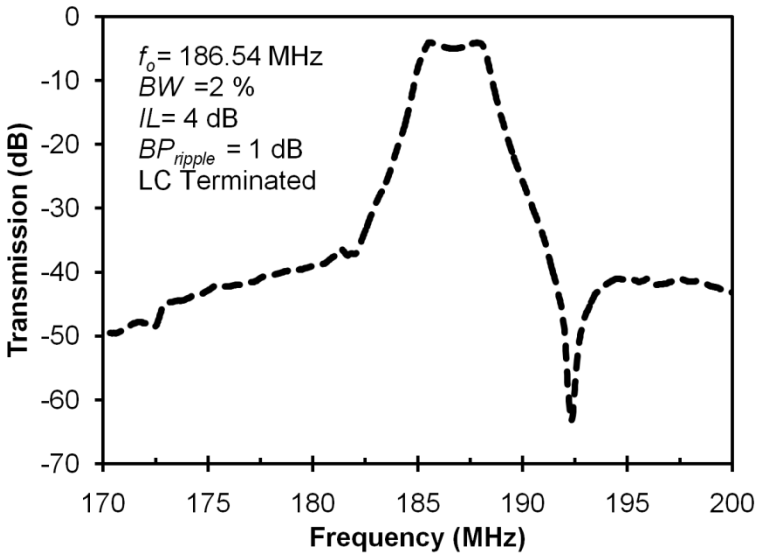

Figure 5.15 – Frequency response for 3×3 micromechanical contour-mode filter composed of two mechanically-coupled 20 μm-radius Zn thin film piezoelectric disk resonators

If a filter operating at a higher frequency band needs to be designed, the size of the constituent resonator can be adjusted, while the length and the width of the coupling beam need to be calculated depending on the desired operation frequency and bandwidth of the filter. A filter consisted of two 20 μm-radius piezoelectrically-transduced disk resonators coupled by a 15 μm-long and 5 μm-wide coupling beam have been implemented. The measured frequency response for this device is shown in Figure 5.15.

Although contour-mode resonators based on circular plates and rings using electrostatic transduction mechanism have been demonstrated at GHz frequencies [17][66], they have large motional impedances which hinders their direct integration with 50 Ω electronics. Moreover, some of the tested capacitively-transduced filters have to utilize a special de-emending technique in order to cancel the parasitics from the carrier substrate and the constituent resonators in order to match the filter to a feasible termination resistance [67]. On the contrary, filters synthesized with arrays of

mechanically-coupled disk resonators equipped with piezoelectric transducers can be successfully matched to 50 Ω termination resistances for frequencies below 400 MHz without the need of de-embedding techniques.

So far, all the measurement results presented are based on two-pole mechanically-coupled disk resonators. Despite their low quality factor (i.e., 800~1,000), the synthesized filters have shown better performance in terms of the insertion loss compared with conventional SAW devices operating at similar frequencies. However, they lack the necessary shape factor for more demanding applications where high selectivity between the stopband and the passband is critical. In order to implement higher order filters, chains composed of more than two mechanically-coupled resonators are needed. The explanation behind this is based on the fact that the order of a mechanically-coupled filter is equal to the number of the coupled resonator LCR circuits in series. Therefore, the higher the order of the filter, the better the selectivity of the filter is. Ideally, the number of mechanically-coupled resonators in a filter can be as high as necessary to fulfill a specific shape factor imposed by the target application. However, in a practical filter implementation, the number of the resonators in the filter will depend on the size constrains and the tolerances imposed by the fabrication process. The concept of an *n*-resonator coupled filter is shown in Figure 5.16.

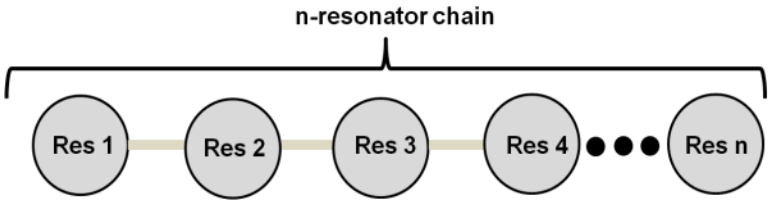

Figure 5.16 – Mechanically-coupled filter composed of *n*-constituent resonators

Filters implemented based upon this topology could also benefit from the employment of parallel sub-filters in order to decrease the effective motional resistance of the filter. When the quality factors of the constituent resonators are not extremely high (Q<1,000), filters based on the topology shown in Figure 5.16 can be implemented without degrading the overall performance. This topology was adopted with an open chain of 2×2 resonators and 3×3 resonators for the measurement results presented in Figure 5.13 and Figure 5.14, respectively. However, for a filter configuration where the *Q's* of the constituent resonators are higher than 1,000, minor differences in the parallel chains will degrade the performance of the filter as demonstrated by Stephanou *et al.* [68], who implemented a 8^{th} order filter with ten parallel sub-filter chains. Despite its terrific frequency selectivity shown by the excellent 20 dB shape factor of 1.8, the insertion loss of this filter after termination with a 2 kΩ resistor was 15 dB with a maximum ripple of 3 dB within the passband.

Conventionally, a method to improve the performance of open-chain filter is to connect an array of identical sub-filter in parallel with λ/2 coupling beams, forcing each sub-filter chain to resonate at the same frequency, thus decreasing the effect of both the frequency variation of each individual sub-filter and the quality factor of each constituent resonator on the array. A conceptual illustration diagram for a mechanical filter composed of a 2D array of coupled resonators is shown in Figure 5.17. However, one of the main disadvantages of this approach is that the overall filter performance is highly sensitive to the possible length deviation of the coupling beam from λ/2.

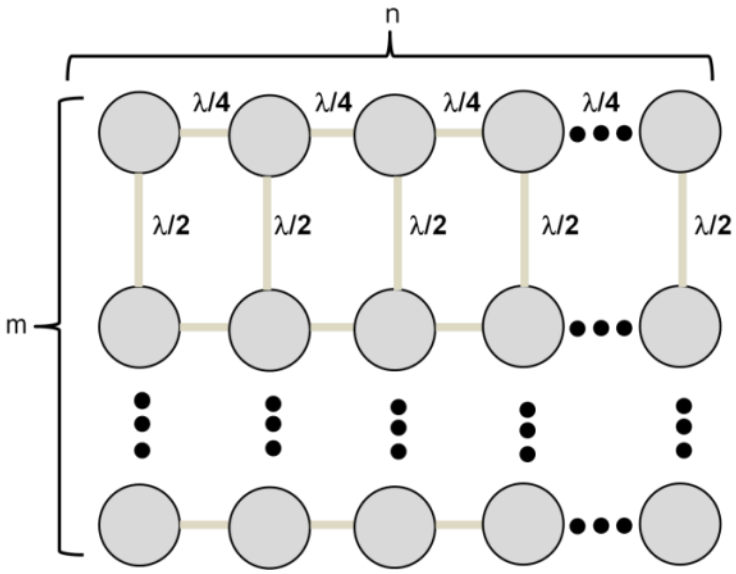

Figure 5.17 – Loop coupled filter composed of a 2D array of mechanically-coupled *n*×*m* constituent resonators

To address the aforementioned issues related to the variations in the quality factor, resonance frequency, and material properties of mechanically-coupled filters, a close-chain filter topology that utilizes λ/2 coupling beam instead of λ/4 beam for connecting parallel sub-filter chains has been implemented. This approach presents several advantages as compared with conventional close-chain filter configurations. The order of the filter is not only defined by the number of the coupled resonators in series to allowing more design flexibility. Hence, a filter with a passband characteristic of a second order filter can be designed with the anticipated shape factor of a 4^{th} order filter. Moreover, this array is less sensitive to the coupling beam length variation, and the motional resistance can be reduced by *m* times the number of parallel arrays.

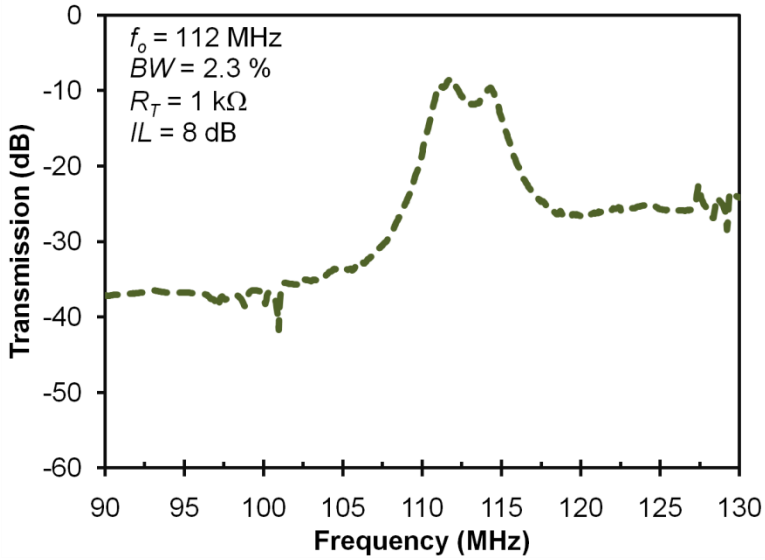

(a)

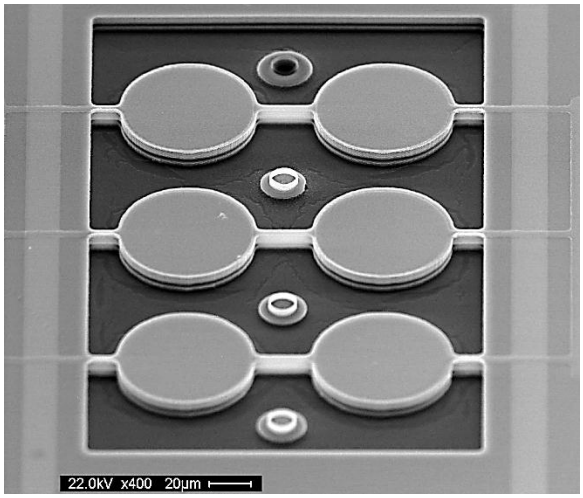

(b)

Figure 5.18 – Frequency response for 3×2 micromechanical contour-mode filter that consists of an array of a 20 µm-radius disk resonator fabricated using a SOI wafer with a 5 µm-thick silicon device layer ; and (b) SEM micrograph of the fabricated device

Figure 5.18 shows the frequency response for a mechanically-coupled filter composed of 20 µm-radius ZnO-on-silicon piezoelectrically-transduced disk resonators as constituent elements. The device was fabricated using a SOI wafer with a 5 µm-thick silicon device layer. The filter consists of three parallel arrays of two mechanically-

coupled resonators. The parallel chains are not linked, thus the order of the filter is given by the number of resonators connected in series, which for this case is two.

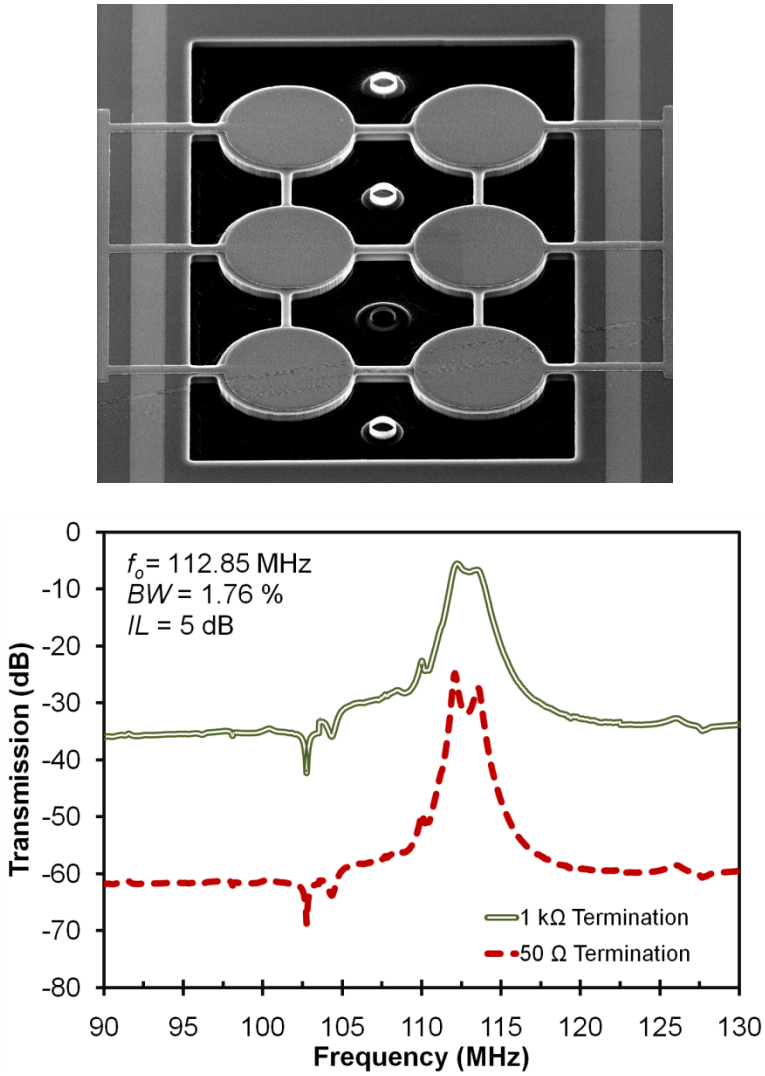

Figure 5.19 – Frequency response for 3×2 micromechanical contour-mode filter composed of an array of 20μm-radius disk resonators linked by λ/4 coupling beams fabricated using a SOI wafer with a 5 μm-thick silicon device layer

If the same filter is re-constructed by a 3×2 parallel array of identically-sized constituent disk resonators that are connected by λ/4 (instead of λ/2) coupling beams, then the coupled array should behave as 6th order filter. If the termination resistance is kept the same for both cases (Figure 5.18 and Figure 5.19) in order to make a fair

comparison, the passband of the 6th order filter should be more flat, and ideally the insertion loss should be at least the same or lower. As seen in Figure 5.19, both the insertion loss and the passband of the filter have been improved. Particularly, the response of the fitter became much sharper. As mention previously, the termination resistance was retained for both filters because ideally they have the same motional resistance (both filters have the same number of parallel arrays).

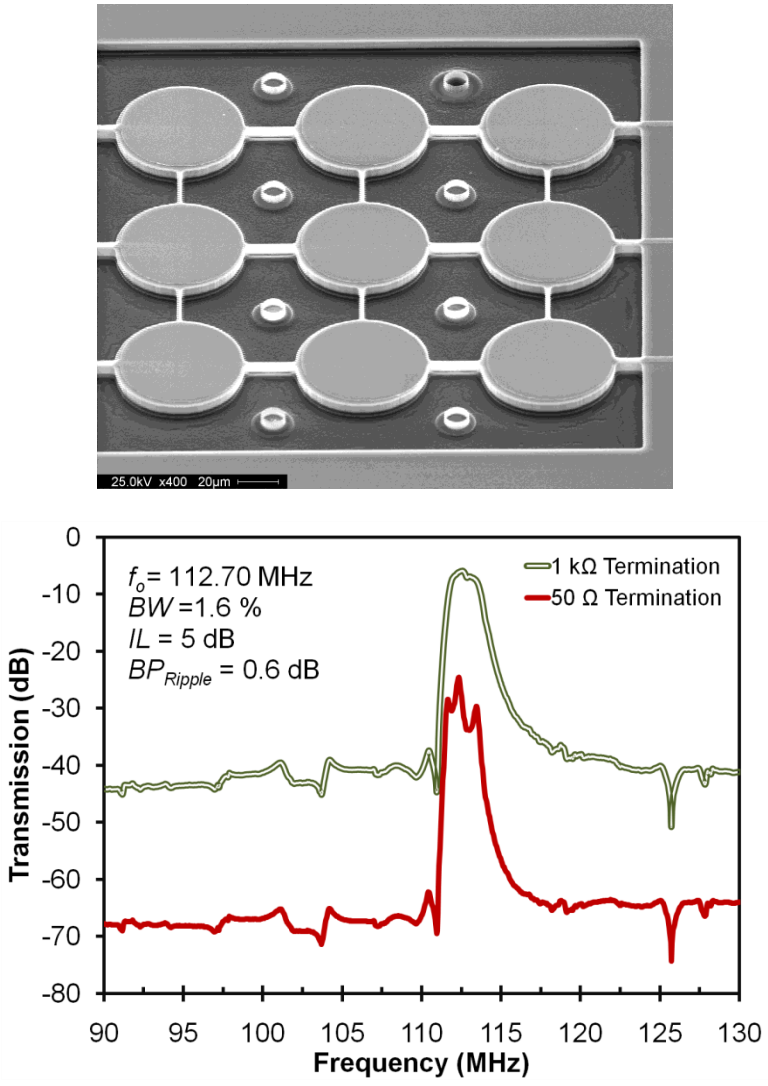

Figure 5.20 – SEM micrograph and frequency response for 3×3 micromechanical contour-mode filter that consists of an array of a 20 µm-radius disk resonators coupled with λ/4 coupling beams fabricated using a in SOI wafer with a 5 µm-thick silicon device layer

If the number of resonators connected in series is increased while keeping the number of parallel sub-filter arrays, a 9th order filter could be implemented with a 3×3 mechanically-coupled resonator array connected in close chain configuration as shown in Figure 5.20. The frequency response for such filter is also shown in Figure 5.20. As can be noted, this filter exhibited a sharp shape factor that is more similar to that of a SAW filter operating in this frequency range. Although the filter was terminated with a termination resistance of 1 kΩ, this can be decreased to 50 Ω if 64-sub-filter chains are connected in parallel, or can be terminated with 50 Ω if a proper L-matching network is inserted.

Figure 5.21 and Figure 5.22 show the SEM micrograph and the frequency response for a two-pole mechanically-coupled filter equipped with 10 sub-filter arrays connected in parallel, respectively. Each sub-filter is composed of two mechanically-coupled 30 μm-radius disk resonators fabricated using a SOI wafer with a 5μm-thick silicon device layer. The resonators operate in the fundamental radial contour mode at 73.2 MHz. The motional resistance of this device is 200 Ω, which allows terminating the filter with a termination impedance as low as 300 Ω. This filter shows 10 times reduction in the termination impedance as compared with a single two-pole filter that is composed a single pair of mechanically-coupled resonators. The key for achieving such performance is the employment of ZnO-on-SOI piezoelectrically-transduced disk resonator array as composite resonator instead of stand-alone resonators. Moreover, it is also expected that the power handling capability for the coupled resonator array will be drastically increased. Aside from lowering the effective motional resistance, the impact of the

arraying concept on the linearity and power handling ability will be further discussed in the subsequent sessions.

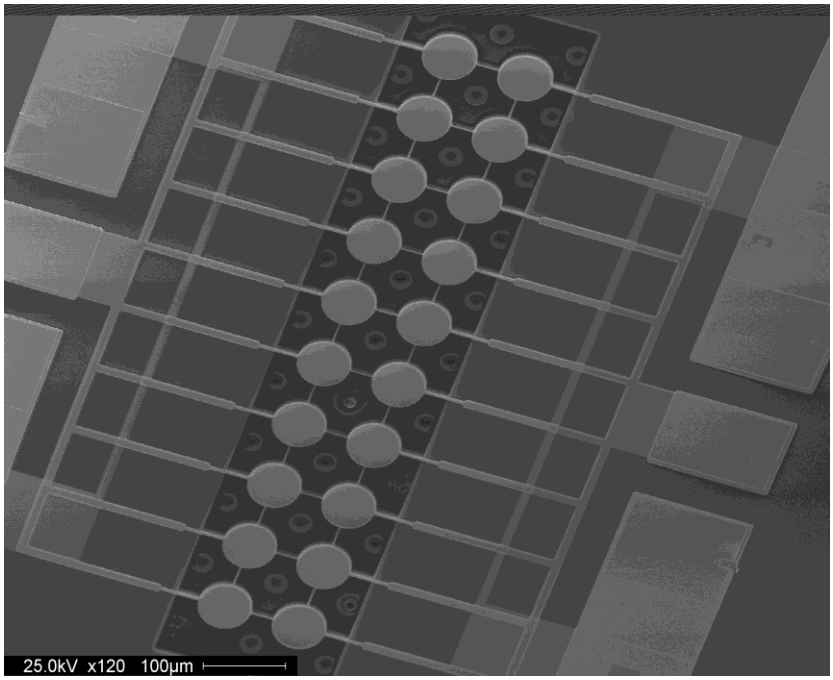

Figure 5.21 – SEM micrograph of 10×2 micromechanically-coupled filter with an array of 30 µm-radius disk resonators coupled together

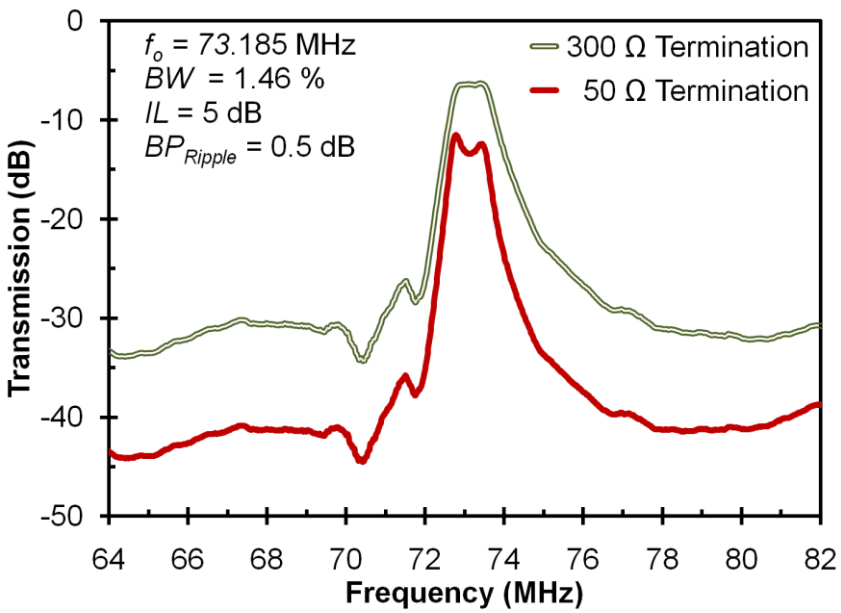

Figure 5.22 – Frequency response for 10×2 micromechanically-coupled filter with 30 µm radius-disk constituent resonators fabricated in a 5 µm SOI wafer, configured in a λ/4 close chain

Figure 5.23 shows the SEM micrograph of a mechanically-coupled filter composed of a 10×4 array of 30 μm-radius disk resonators. As can be observed, the novel fabrication process technologies presented in Section 3.4 allows the fabrication of large 2D array of mechanically coupled resonators with a high yield.

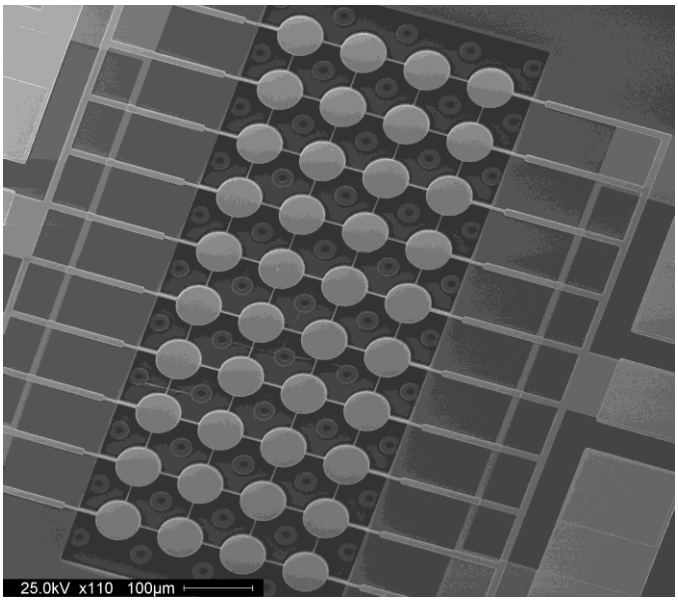

Figure 5.23 – SEM micrograph of a mechanically-coupled filter conmposed of 10×4 array of 30 μm-radius disk resonators mechanically coupled together by λ/4 coupling beams

5.1.8 Limitations of the Mechanically-Coupled Array Technique

As the size of the micromechanical disk resonator is reduced to reach operating frequencies in the UHF range, the electromechanical coupling coefficient also degrades, which leads to increased motional resistance. Moreover, to avoid mass loading effect from the coupling elements and to achieve a reasonably narrow filter bandwidth, mechanically-coupled filters would eventually require submicron coupling elements that are too hard to manufacture reproducibly using low-cost processes. Mechanically-coupled filters based on ZnO-on-SOI resonators and resonator arrays can operate with excellent performance in term of insertion loss and out-of-band rejections at frequencies

up to 300 MHz or so. Moreover, if a high acoustic velocity material such as diamond is introduced in the structural material, filters with center frequencies up to 600 MHz can be readily implementable as the acoustic velocity in diamond is approximately twice of that of silicon.

Although the coupled-array method has shown some great promise for lowering the filter termination impedance, further impedance reduction is necessary to eliminate the need of large termination resistor or L-matching networks to interface the filter directly to 50 Ω electronics. However, the further reduction of the filter termination impedance is limited by several remaining issues such as *Q* degradation and spurious-mode generation as a consequence of the array configuration. Moreover, after reaching a certain number *N* of coupled parallel resonators, the termination impedance of the filter will no longer decreases by increasing *N*. Nonetheless, the fundamental benefit of the mechanically-coupling approach is the enhancements of the power handing capability which is crucial for front-end filters operating in the VHF range.

5.2 Capacitively-Coupled Piezoelectrically-Transduced Filters

The main advantage of capacitively-coupled filters is their great potential for extending the operation frequencies into the UHF range. Piezoelectrically-transduced filters using capacitively coupling does not require mechanical beams with precisely-defined dimensions. Moreover, the filter bandwidth can be also synthesized by the device CAD layout, facilitating the design and fabrication of filters with multiple frequencies and bandwidth characteristics side by side. In addition, the electrical coupling offers the possibility to implement filters with excellent shape factors and out-of-band rejection without the need of more than four resonators.

5.2.1 Device Operation

For a two-resonator coupled system composed of a coupling capacitor and two identical resonators with nominal frequency (f_o), quality factors (Q) and motional resistances (R_m), the insertion of a shunt coupling capacitor (C_c) in between the two adjacent resonators creates a second mode of resonance, which can be expressed by:

$$f_1 = f_0 \sqrt{\frac{1 + \pi f_o C_c R_m Q}{\pi f_o C_c R_m Q}} \tag{5.14}$$

When piezoelectrically-transduced resonators are connected in the cascade mode, the shunt capacitance C_c rather than be an external element, simply represents the intrinsic capacitance of the constituent resonators, which is dependent upon the dielectric properties of the piezoelectric layer and its physical dimensions. Figure 5.24 shows the simplified electrical equivalent circuit and the frequency response for a second-order capacitively-coupled filter.

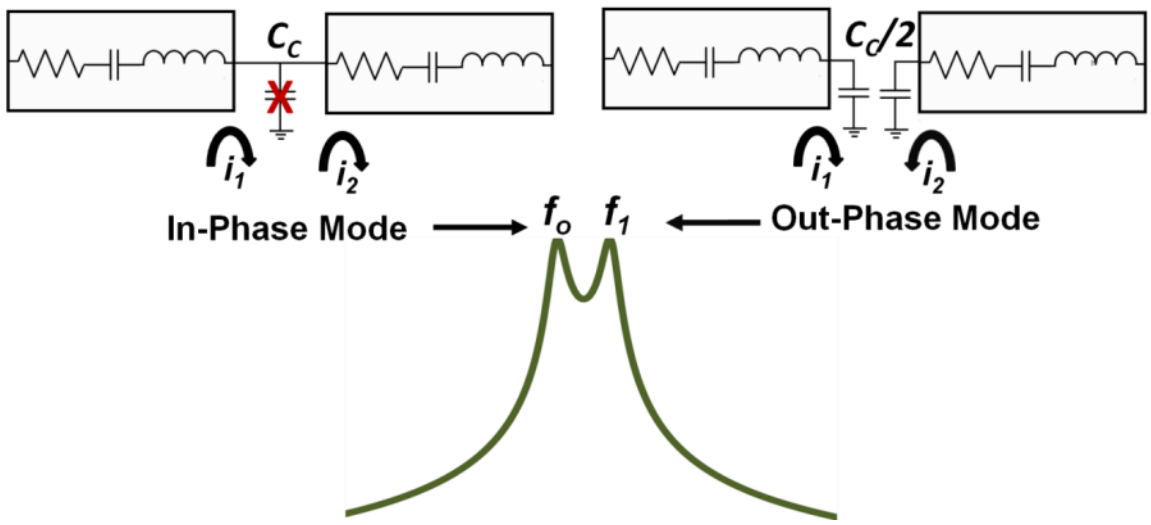

Figure 5.24 – Electrical schematic diagram of a second-order capacitively-coupled filter and its frequency response [69]

The behavior of the capacitively-coupled filter can be explained as follows: at the nominal resonance frequency f_o, the two resonators vibrate in phase and the coupling capacitor does not contribute to the frequency response of the system. At the second resonance frequency f_1, the two resonator vibration out of phase (180°), and the coupling capacitor does have an effect in frequency response of the system. To better understand the operation principle, the capacitively-coupled filter can be divided into two identical parts each acts as a resonator terminated with a series coupling capacitor $C_c/2$ connected to ground. When the two resonators vibrate in phase, the generated current through the coupling capacitor would cancel each other. But when the two resonators operate in the out-of-phase mode at the second resonance frequency f_1, each resonator tank results in in-phase current contribution to the coupling capacitor. As a consequence, the coupling capacitor reduces the total capacitance of the resonator when it operates at the second resonance frequency, thus forcing the second resonance mode to have a slightly higher frequency, which can be calculated by Equation (5.14). A complete analysis for higher order capacitively-coupled filters is described by Pourkamali *et al.* [70]. The electrical coupling approach offers the viability to implement filters with excellent shape factors and out-of-band rejection, while allowing the design of the bandwidth of the filter without the use of external components or coupling beams that can be problematic when their required dimensions approaches the sub-micron region. Similar to the case for mechanically-coupled filters, the order of the filter synthesized in this topology is also given by the number of cascade-connected resonators. In general, a capacitively-coupled filter composed of a certain number of cascade-connected resonators would behave similarly to the mechanically-coupled filter with the same number of resonators coupled

together by λ/4-long coupling beams. However, carefully consideration must be taken when designing the size of the piezoelectrically-transduced filter. For instance, if length-extensional rectangular plates are used as the constituent resonator, one of the two lateral dimensions (i.e., the length) would define the resonance frequency f_o of the constituent length-extensional mode resonators, and the second dimension (e.g., the width) in conjunction with the first dimension, the permittivity and the thickness of the piezoelectric film, will determine the intrinsic capacitance of the constituent resonators, and therefore the bandwidth of the electrically-coupled filter.

The presented analysis can be extended and revised for more than two resonators electrically cascade-connected together in order to implement a higher order filter. For a third-order capacitively-coupled filter, all resonators vibrate in phase in the first resonance mode, thus the effect of the intrinsic coupling capacitors is automatically cancelled. The frequency for this mode is given by f_o, which is the common nominal resonance frequency of the constituent resonators. At the second resonance mode, the first and the third resonator vibrate out of phase (180°), and the second resonator remains static. As a result, no current passes through the second resonator and the resonance frequency for this mode is given by:

$$f_1 = f_0 \sqrt{\frac{1 + 2\pi f_o C_c R_m Q}{2\pi f_o C_c R_m Q}} \tag{5.15}$$

In the third resonance mode, all the adjacent resonators vibrate out of phase with respect to each other. The coupling capacitor for this mode is split between the resonators. For the first and the third resonator, the effective coupling capacitor is one-

third of C_c whereas for the second resonator the effective coupling capacitor is two-third of C_c. Therefore, the resonance frequency for this mode can be calculated as follows:

$$f_2 = f_0 \sqrt{\frac{3 + 2\pi f_o C_c R_m Q}{2\pi f_o C_c R_m Q}} \tag{5.16}$$

5.2.2 Fabrication Process

Arrays of two and three capacitively-coupled piezoelectrically transduced resonators have been fabricated and tested using the fabrication process described in Section 3.3. The fabricated filters consist of piezoelectrically-transduced extensional-mode rectangular plate resonators connected in cascade electrically, with the top interdigitated electrodes patterned in order to excite the higher order length-extensional or width-extensional modes. A high resistivity silicon substrate was used for the fabrication of filters to reduce the effect the feedthrough parasitics introduced by the substrate.

5.2.3 Experimental Results

The fabricated capacitively-coupled filters were tested in a cascade RF probe station. All testing is performed in air at atmospheric pressure and ambient temperature. The scattering parameters (S-Parameters) of the devices are extracted directly using an Agilent E5071B vector network analyzer. A Short-Open-Load-Thru (SOLT) calibration procedure using a CS-5 calibration substrate from GGB Industries Inc was conducted to de-embed the effects of the connectors, the network analyzer ports, and the carrier substrate.

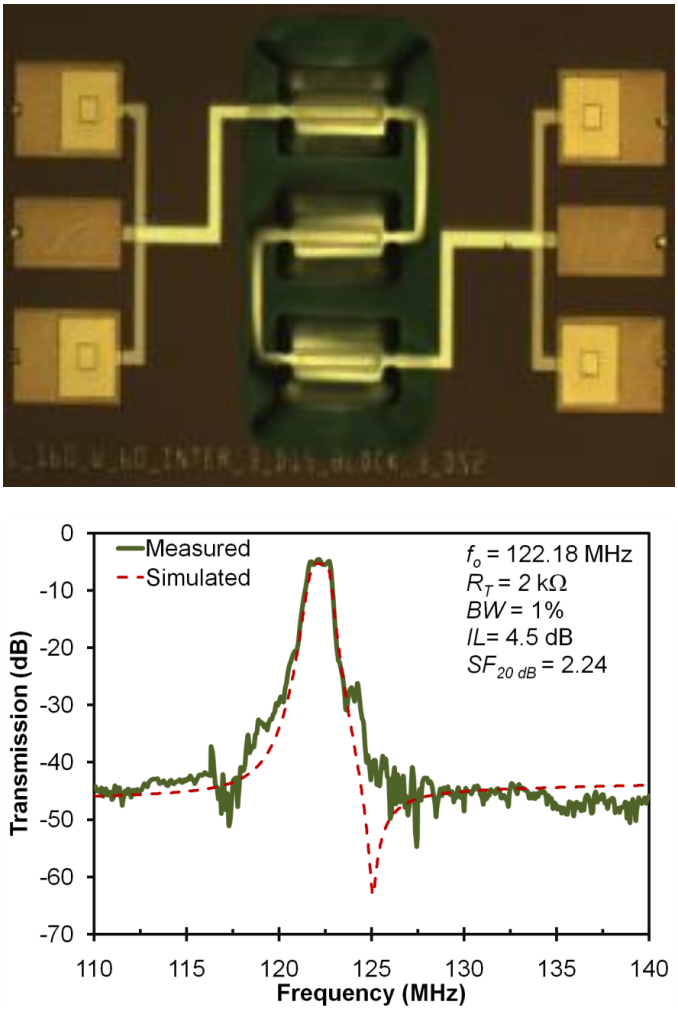

Figure 5.25 – Optical micrograph and frequency response for the fabricated 122.18 MHz 3rd order capacitively-coupled piezoelectrically-transduced filter

Figure 5.25 shows the optical micrograph and the frequency response for a 3rd order capacitively-coupled filter operating at 125 MHz. As can be clearly observed, the filter passband consists of three resonance peaks which correspond to three different resonance modes described in Section 5.2.1. The extracted values for the resonator equivalent circuit parameters are based on the model presented in section 4.3. The intrinsic coupling capacitor is calculated based on the electrical properties of the ZnO piezoelectric film and the lateral dimensions of the constituent resonators. The extracted

equivalent electrical circuit model parameters for the capacitively-coupled filter are presented in Table 5.3.

Table 5.3 – Extracted equivalent electrical parameter values for the fabricated 3rd order capacitively coupled resonator

Parameter	Value
R_m	500Ω
C_m	2.91 fF
L_m	594.6 µH
C_c	461 fF
Co	0.3 pF
C_f	1 fF

If the resonators in the same length-extensional mode is used while retaining the length dimension that define the resonance frequency, the width of the constituent rectangular plate resonators can be increased to enlarge the intrinsic coupling capacitance, thus reducing the bandwidth of the newly synthesized filter as shown in Figure 5.26. As another direct result of the increase of the area of the rectangular plate resonator, the electromechanical coupling coefficient also increases, therefore decreasing the value of the termination impedance needed to flatten the filter passband. This result is certainly encouraging for design intermediate frequency (IF) filters with narrow bandwidths that can be potentially terminated by 50 Ω impedances without the use of extra matching networks. However, to synthesize an IF filter with a truly wide bandwidth (i.e., BW>5%), it would require an intrinsic coupling capacitor of extremely small values, which in turn would require excessive scaling down of the resonator lateral dimensions beyond the practical limit. Moreover, even if such a low value intrinsic coupling capacitance can be realized for a wide-band filter, the size of the rectangular plate resonators and the piezoelectric transducers would shrink considerably, thus

decreasing the electromechanical coupling factor and increasing the termination resistance needed to flatten the filter passband. Nevertheless, as compared to the filter synthesis by mechanically-coupling approach, the capacitively-coupling provides more design flexibility and also alleviates the requirements for mechanical coupling elements to substantially lower the corresponding design uncertainty.

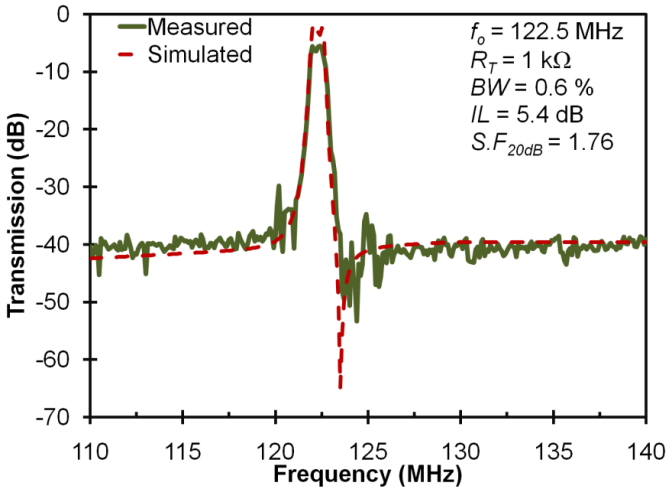

Figure 5.26 – Frequency response for the fabricated 122.5 MHz 3rd order capacitively-coupled piezoelectrically-transduced filter

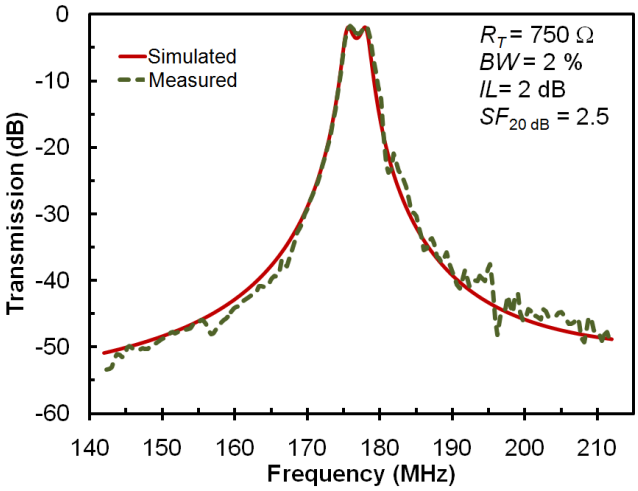

Figure 5.27 – Simulated and measured frequency responses with and without applied termination resistance for a 175.5 MHz 2nd order capacitively-coupled piezoelectrically-transduced filter

Table 5.4 – Extracted equivalent electrical parameter values for the fabricated 2nd order capacitively-coupled filter operating at 175.5 MHz

Parameter	Value
R_m	360 Ω
C_m	3.92 fF
L_m	209.77 µH
C_c	0.255 pF
Co	0.5 pF
C_f	2.0 fF

Figure 5.27 shows the frequency response for a 2nd order capacitively- coupled filter. The filter has two constituent width-extensional rectangular plate resonators with dimensions of 80 µm × 140 µm, for which the width defines the resonance frequency. The rectangular plate resonators are operating in the 6th order width-extensional mode. Both bottom and top electrodes are made of 130 nm-thick platinum, and the device layer is made of 800 nm-thick of ZnO. From Equation (2.12), the predicted resonance frequency of the constituent resonators is 169.1 MHz, which is fairly close to the measured frequency of 175.5 MHz. The discrepancy between the theoretical value and the measurement result is largely due to the fabrication tolerance and the difference between the actual properties of the deposited ZnO thin film from its bulk values used for the theoretical calculation. The filter was designed to operate with a percentage bandwidth of 2%, which is in close agreement with the measured result.

A 3rd order filter can be synthesized with three piezoelectrically-transduced resonators are electrically connected in cascade. As compared to a 2nd order filter, the 3rd order filter offers an improved shape factor, however the value of the termination resistance will also increase due the addition of an extra cascade-connected resonator. Obviously, the bandwidth of the filter would also change, which can be designed by

adjusting the width of the constituent resonators. Figure 5.28 compares the simulated and measured frequency responses for the 175.5 MHz 3rd order capacitively-coupled filter. As can be noted from Figure 5.27 and Figure 5.28, the central frequency of the filter remains the same, but the 20 dB shape factor of the filter improves from 2.5 to 2.2 for the 3rd order capacitively-coupled filter. However, as mentioned above, the necessary termination resistance also increases from 750 Ω to 1 kΩ, due to the additional resonator in the filter.

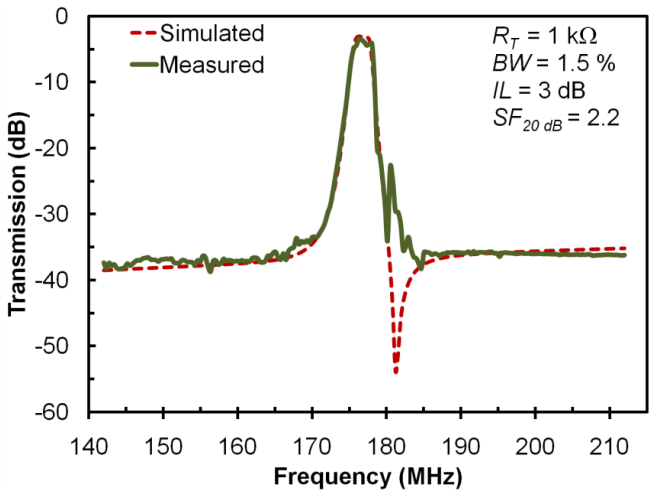

(a)

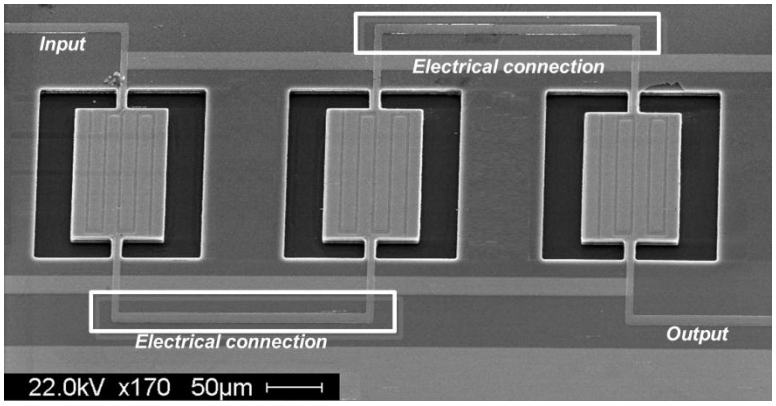

(b)

Figure 5.28 – (a) Frequency response for the fabricated 175.5 MHz 3rd order capacitively-coupled piezoelectrically-transduced filter; and (b) the SEM micrograph of the fabricated filter

5.3 Acoustically-Coupled Micromechanical Filters

Pursuant to reducing the complexity of filter implementation based on piezoelectrically-transduced micromechanical contour-mode resonators, this section presents an alternative mechanical filter synthesis strategy that uses two closely-spaced orthogonal resonances from a single piezoelectrically-transduced plate resonator vibrating in a length-extensional mode to generate a 2^{nd} order 2-pole filter without the need for multiple resonators. Moreover, this filter synthesis technique removes the need for additional mechanical coupling elements and also greatly enables the design and fabrication of multiple micromechanical filters with minimum footprint operating at different frequencies needed for futures multiband and multimode wireless transceiver front-ends.

5.3.1 Device Operation

An acoustically-coupled filter also known as monolithic filter shares a similar structural design as a two-port resonator. The main difference between a resonator and a monolithic filter is the top electrode pattern used to drive the device into the resonance. In a monolithic filter, the top electrode is pattern to enable the excitation of closely-spaced dual resonance modes of a resonator with similar electromechanical coupling factors. In the symmetric mode, the displacements of both electrodes are in-phase, whereas in the asymmetric mode the displacements of the two electrodes are 180º out of phase. As shown in Figure 5.29, by coupling multiple modes of a single resonant microstructure, the need for designing a coupling element is eliminated, thus simplifying both the design and fabrication while reducing the overall size of the filter. In the following design shown in Figure 5.29, the critical dimension which defines the center frequency in an

extensional-mode monolithic filter is the length of the plate. As is shown in Figure 5.30, by changing the width of the plate the frequency spacing between the dual modes can be fine-tuned. Therefore, the bandwidth of a monolithic filter at a certain center frequency can be precisely controlled by CAD layout design.

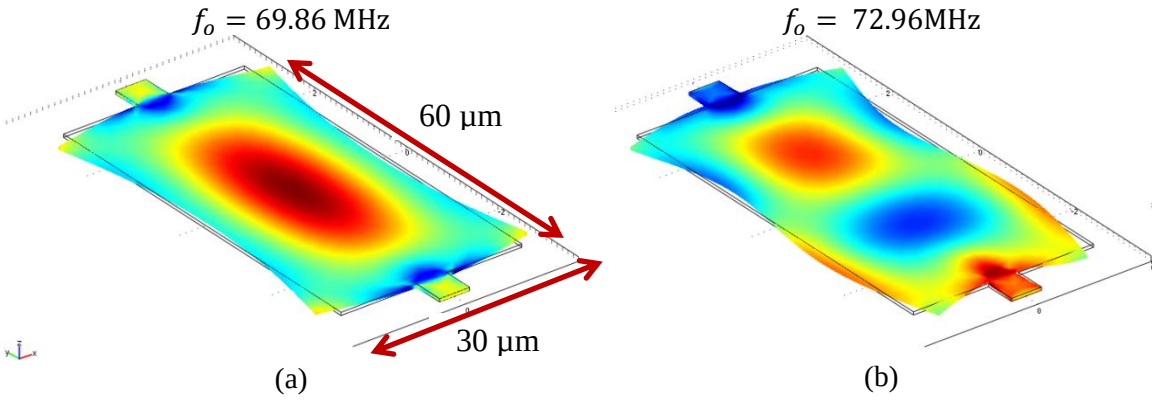

Figure 5.29 – Simulated dual fundamental length-extensional mode-shapes of a 60 µm x 30 µm ZnO plate resonator for a) symmetric resonance-mode; and b) asymmetric resonance-mode

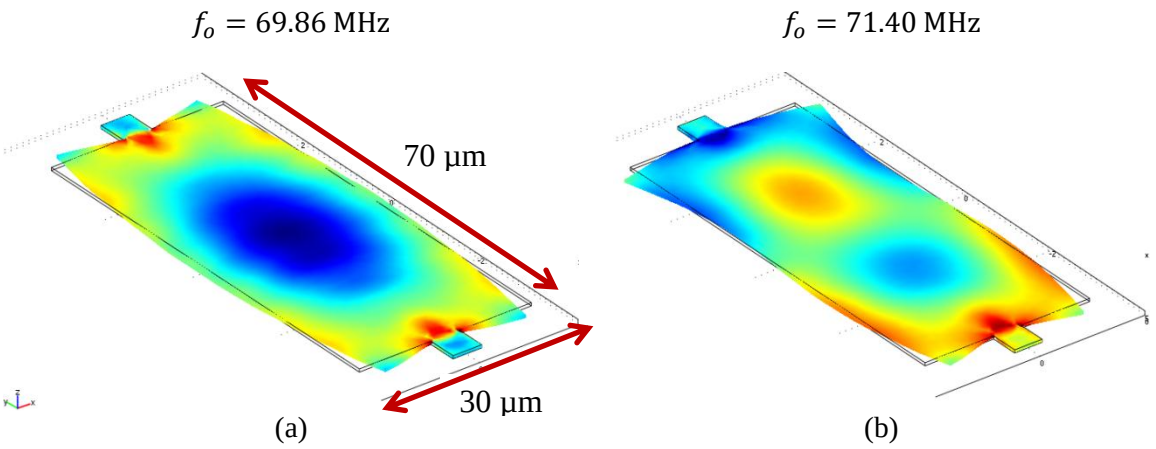

Figure 5.30 – Simulated dual fundamental length-extensional mode-shapes of a 70 µm × 30 µm ZnO plate resonator for a) symmetric resonance-mode; and b) asymmetric resonance-mode

5.3.2 Equivalent Electrical Model

A similar model to the one used for mechanically-coupled resonators can be used to model the behavior of an acoustically coupled filter. As opposed to a mechanically-coupled resonator array in which the mechanical vibrations are coupled by mean of a

coupling element (i.e., longitudinal-beam), the mechanical vibration between different modes at adjacent frequencies in an acoustically coupled filter is coupled by the device itself. The equivalent electrical circuit model for 2nd order acoustically-coupled filter is shown in Figure 5.31. The coupling element in this model is represented by an inductor (L_c) instead of a capacitor or capacitor network as needed for mechanically-coupled and electrically-coupled filters. The inclusion of the inductor in the electrical model in Figure 5.31 accounts for the fact that the frequency of the in-phase mode is not always lower than the frequency of the out-of-phase mode.

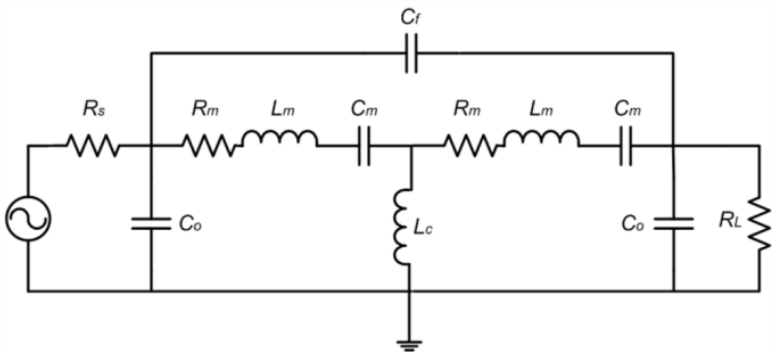

(a)

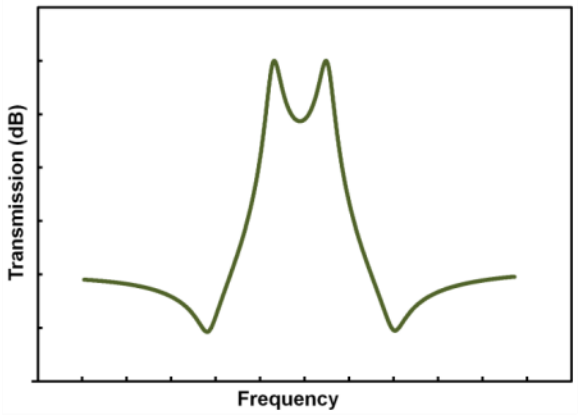

(b)

Figure 5.31 – (a) Equivalent electrical circuit model for a 2nd order acoustically-coupled filter; (b) Normalized frequency response for a 2nd order acoustically coupled filter

5.3.3 Fabrication Process

Acoustically coupled piezoelectric filters have been fabricated and tested using the process described in Sections 3.3 and 3.4. The fabricated filters consist of a single resonator in which two resonance modes at adjacent frequencies are coupled. The fabricated devices use the interdigitated design in order to excite higher order modes on the plates. The two electrode patterns are designed in order to allow the presence of the two modes simultaneously. A high resistivity silicon substrate was used for the fabrication of the monolithic filters based on thin film ZnO piezoelectric resonators. Additionally, piezo-on-silicon resonators fabricated using SOI wafers with 5 μm and 20 μm silicon device structural layers were also used.

5.3.4 Experimental Results

The fabricated monolithic filters were tested in a cascade RF probe station. All testing is performed in air at atmospheric pressure and ambient temperature. The scattering parameters (S-Parameters) of the devices are extracted directly using an Agilent E5071B vector network analyzer. A Short-Open-Load-Thru (SOLT) calibration procedure using a CS-5 calibration substrate from GGB Industries Inc was implemented to cancel the effects of connectors and the carrier substrate.

Figure 5.32 shows the frequency response a for thin film piezoelectrically-transduced monolithic filter operating at 155 MHz. The device dimensions are 100 μm × 200 μm, which is operating in the 5^{th} order length-extensional mode. As mentioned above, if the lateral dimension (length in this case) that defines the resonance frequency is set constant, and the width of the plate can be changed to adjust the bandwidth. In this example, the width of the plate was decreased, and the bandwidth of the filter was

increased consequently. For comparison, the measured frequency response for a thin film monolithic piezoelectric filter with dimensions of 100 µm × 190 µm is shown in Figure 5.33. The bandwidth of the synthesized filter increased from 0.81% to 1.26% as a result of a 10 µm change in the width of plate resonator. The electrode pitch size for both cases is 20 µm, which is the critical dimension for setting the central frequency of the filter.

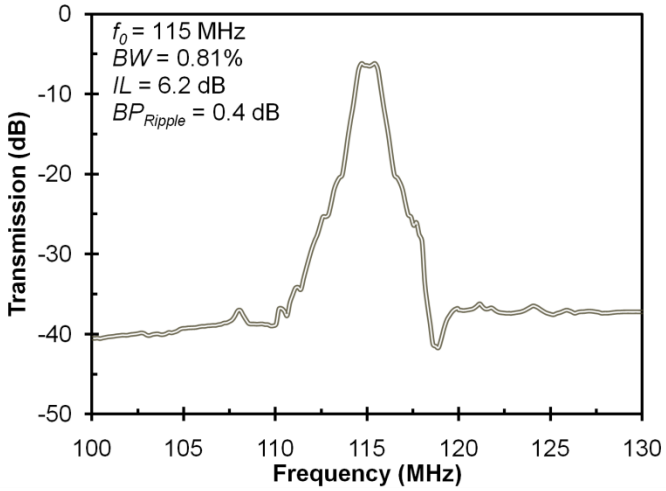

Figure 5.32 – Frequency response for the fabricated 155 MHz monolithic filter with 100 µm x 200 µm lateral dimensions

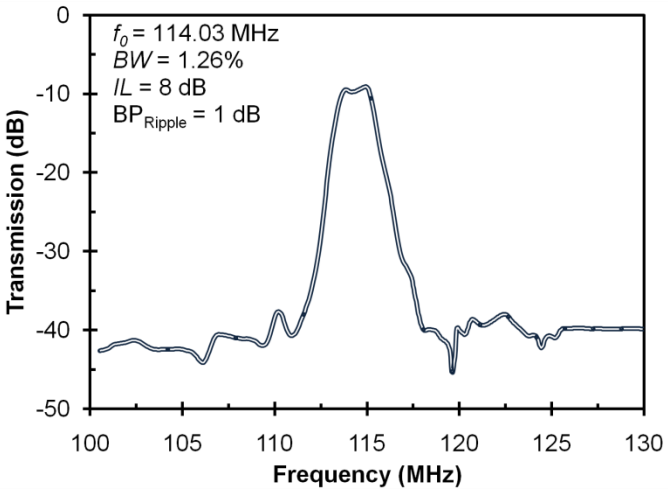

Figure 5.33 – Frequency response for the fabricated 155 MHz monolithic filter with 100 µm x 190 µm lateral dimensions

It is worth mentioning that there is a not closed-form solution to quantify the effect of the secondary dimension on the filter bandwidth. Modal analysis using finite element method allows thorough investigation of the resonance mode shapes of a designed resonant microstructure to provide considerable insight for optimization of the length and the width for obtaining the desired operation frequency and bandwidth. However, there is an upper limit for the maximum attainable bandwidth for an acoustically-coupled filter, and this limit depends on the electrical and mechanical properties of the piezoelectric thin film. The expression for the maximum attainable bandwidth is given by [71] :

$$BW_{max} = \frac{8}{\pi^2} k_t^2 \tag{5.17}$$

where k_t^2 represents the effective electromechanical coupling coefficient, which is different from electromechanical coupling factor introduced in Section 2.6. The effective electromechanical coupling coefficient is a parameter that describes the internal energy conversion efficiency between electrical and mechanical domains within the piezoelectric film. It is worthwhile mentioning that the electromechanical coupling coefficient (k_t^2) is an intrinsic property of the piezoelectric transducer and is not dependent on the geometry of the actual transducer or the shape of the resonator, which should not be confused with the electromechanical coupling factor (η). k_t^2 can be expressed by:

$$k_t^2 = \frac{d_{ij}^2}{\varepsilon_i s_{jj}} \tag{5.18}$$

where d_{ij}^2 is the piezoelectric coefficient (e.g., transverse piezoelectric coefficient d_{31} for contour-mode resonators), ε_i is the dielectric permittivity of the piezoelectric film, and s_{jj} is the compliance. For ZnO thin films, the k_t^2 value is 6.3% for in plane contour-mode

vibrations as demonstrated by Lakin [72], for AlN thin film, the k_t^2 value is on the order of 4.5 %. Using Equation (5.17), the calculated maximum attainable bandwidth for thin film ZnO monolithic filters is anticipated to be roughly 5.1 %. As far as the minimum attainable bandwidth, this is largely determined by the highest achievable quality factor of the constituent resonator.

In order to reach higher operation frequencies, a filter synthesized by the acoustically-coupled configuration can be strategically designed. In particular, the center frequency of the acoustically-coupled filter can be further extended as the width of the interdigitated electrode is reduced. Figure 5.34 shows the measured frequency response for an acoustically-coupled piezoelectrically-transduced contour-mode rectangular plate filter operating at 481.2 MHz. This filter consists of one resonator operating in the 29th order mode. The dimensions of the filter are 140 µm × 40 µm, and the pitch size of the interdigitated electrode is 4.82 µm. The measured bandwidth of the filter is 0.8 % (3.887 MHz) with an insertion loss of 6 dB when the filter is terminated using L-matching network. The first resonance mode of this filter can be calculated by:

$$f_o = \frac{n}{2l} v_{eq} \tag{5.19}$$

where v_{eq} is the equivalent acoustic velocity of the resonator body, which is equal to 4325 m/s. It is worth mentioning that loading effect introduced by the top and bottom electrodes has been taken into account using Equations (4.5) and (4.6). From Equation (5.19), the filter center frequency is predicted to be 478.19 MHz, which is in very close agreement with the measured center frequency of the fabricated device. As mentioned previously, the bandwidth of the filter can be only determined via modal analysis using FEM simulation programs such as ANSYS or COMSOL. The simulated resonant mode

shapes corresponding to the fabricated 481.56 MHz acoustically-coupled filter are shown in Figure 5.35. The total number of the lines of the simulated strain field represents the mode number of the filter in length-extensional mode. As can be observed from the modal simulation, the frequency difference between the two resonance modes is approximately 2 MHz. The apparent discrepancy between the simulated and the measured bandwidth is due to the fact that the bandwidth derived from the FEM simulation corresponds to the frequency difference between the two resonant modes without taking into account the finite quality factor of the resonance peak and the influence of the filter termination impedance.

Figure 5.36 shows the frequency response and the matching circuit diagram of a 480 MHz SAW filter (Part Number 855271) from TriQuint [73]. The bandwidth of this commercial filter is 9 MHz with a typical insertion loss of 18 dB. Although the fabricated MEMS filter has a different bandwidth, this outperforms the SAW device at the same frequency at least with respect to the insertion loss. However, the out-of-band rejection is 30 dB lower than that of its SAW counterpart. Nevertheless, this issue can be fixed by engineering the carrier substrate with proper feedthrough shielding features or employing a substrate with higher resistivity (i.e.> 6 kΩ-cm). It can be noted that SAW filters and the MEMS filters developed by this work use an L matching network to match the filter to 50 Ω source and termination impedance. Nonetheless, it is fair to mention that a commercially-available SAW filter operating at 480 MHz with slightly better performance could be found as such technology is also evolving with time. However, the main idea behind this comparison is to demonstrate that MEMS filters based upon

acoustically-coupled resonators perform as good as and potentially better than their SAW counterparts.

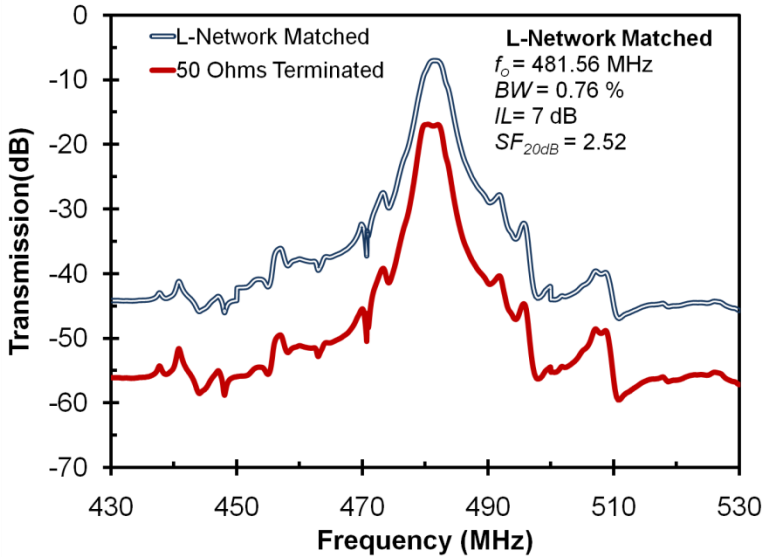

(a)

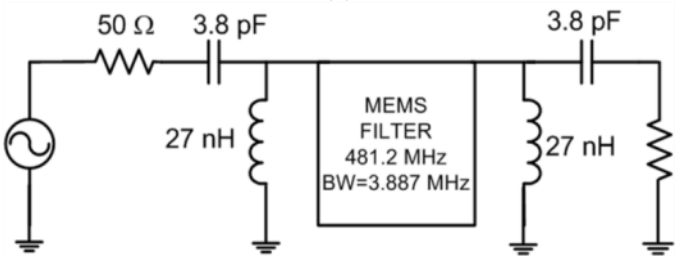

(b)

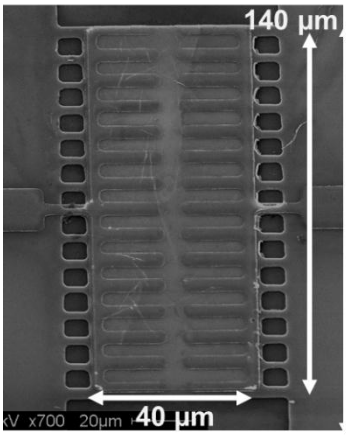

(c)

Figure 5.34 – Frequency response for the fabricated 481.56 MHz monolithic filter with different terminations; (b) Equivalent circuit model for MEMS filter terminated by L-matching network; (c) SEM micrograph of the fabricated acoustically-coupled filter

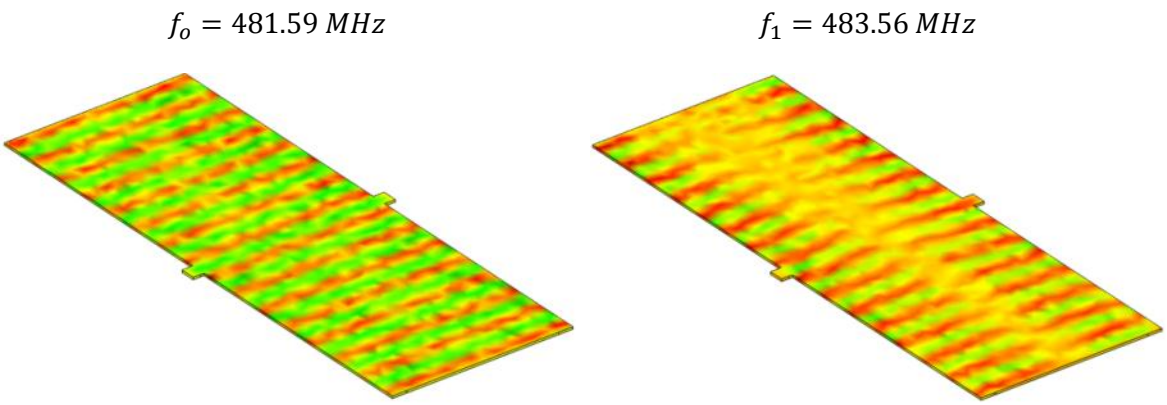

Figure 5.35 – Modal simulation of the resonance modes that define the passband of acoustically-coupled filter that corresponds to the fabricated 481.56 MHz monolithic filter (from COMSOL FEM simulations)

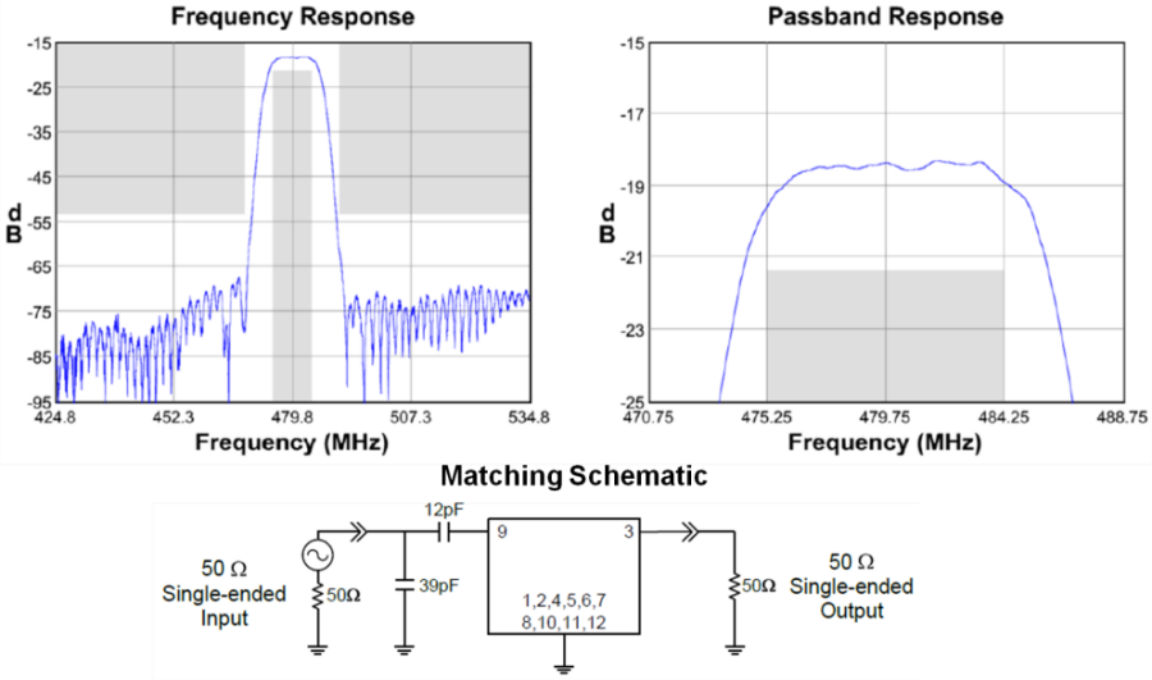

Figure 5.36 – Frequency response and matching circuit diagram of a commercial 480 MHz SAW filter (Part Number 85527 from TriQuint [73])

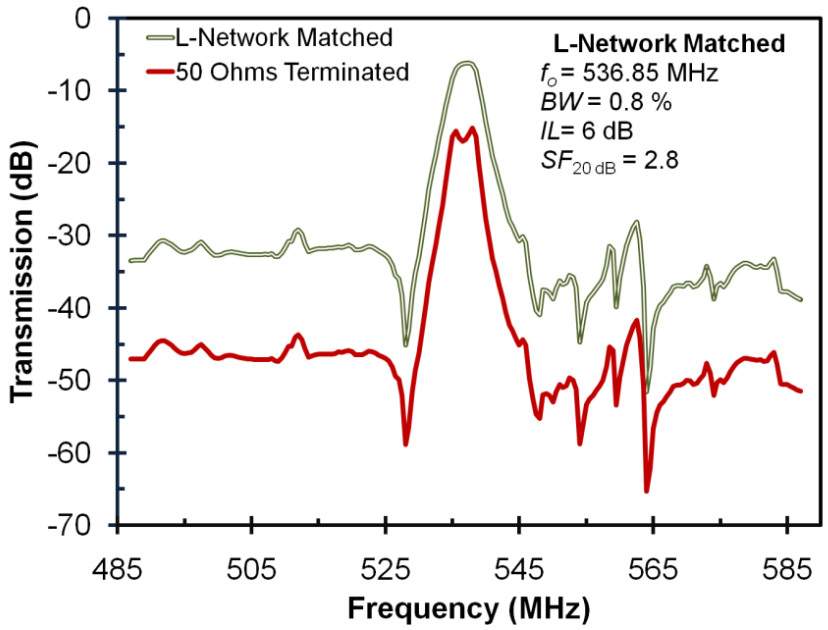

(a)

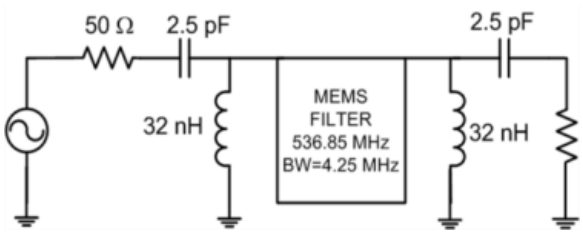

(b)

Figure 5.37 – (a) Frequency response for the fabricated 536.85 MHz monolithic filter with 140 µm × 40 µm dimensions with different terminations; (b) Electrical circuit diagram of the L-matching network used to terminate the MEMS filter

If the width and length dimensions of the filter shown in Figure 5.34 are kept the same, but the number of interdigitated fingers of the electrode is increased to excite a higher-order mode, the filter central frequency could be readily increased to 537 MHz as shown in Figure 5.37. As compared to the design shown in Figure 5.34, the pitch size of the interdigitated electrode was reduced from 4.82 µm to 4.24 µm to operate in the 33rd length-extensional mode instead of the 29th mode. The measured filter bandwidth is 0.8 % (4.25 MHz) with an insertion loss of 6 dB by terminating the filter using a L-matching

network. Figure 5.38 shows the frequency response and the electrical circuit diagram of the matching circuit for a commercial SAW filter operating at the same frequency range with similar characteristics. Figure 5.39 presents the frequency response for the fabricated 536.85 MHz monolithic filter with different terminations. It is worthwhile mentioning that the fabricated monolithic MEMS filter can be connected directly to a RF front-end antenna with 377 Ω characteristic impedance to exhibit an insertion loss of 6 dB in the passband, which is quite acceptable. Nevertheless, when the filter is terminated with an L-matching circuit as illustrated in Figure 5.37, it would exhibit a better performance in terms of out-of-band rejection.

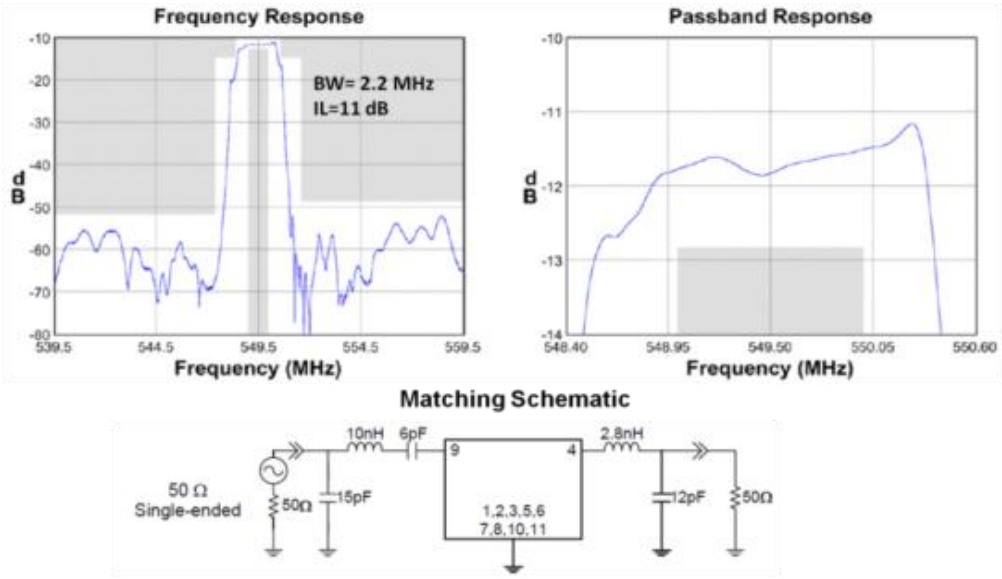

Figure 5.38 – Frequency response and matching circuit schematic for a commercial 549.5 MHz SAW filter (Part Number 855985 from TriQuint [74])

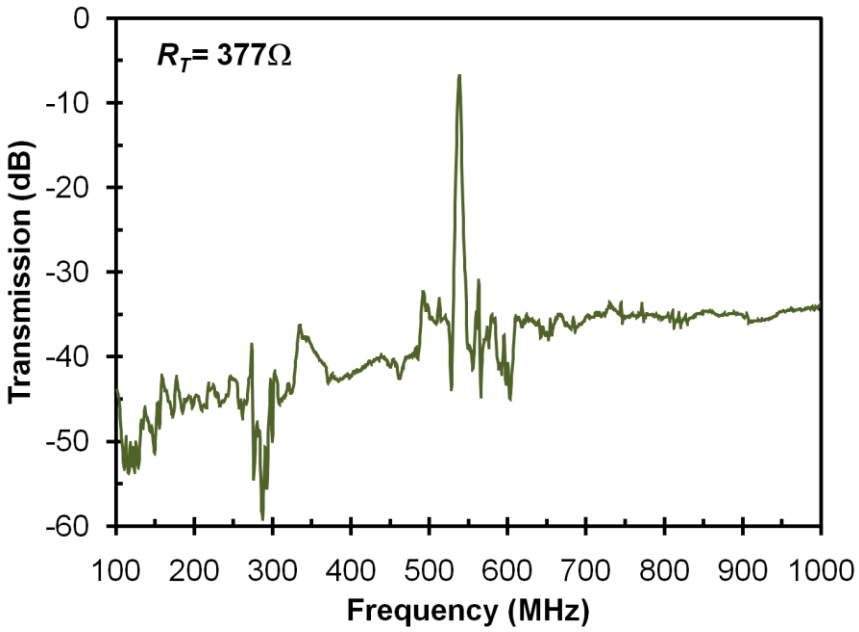

(a)

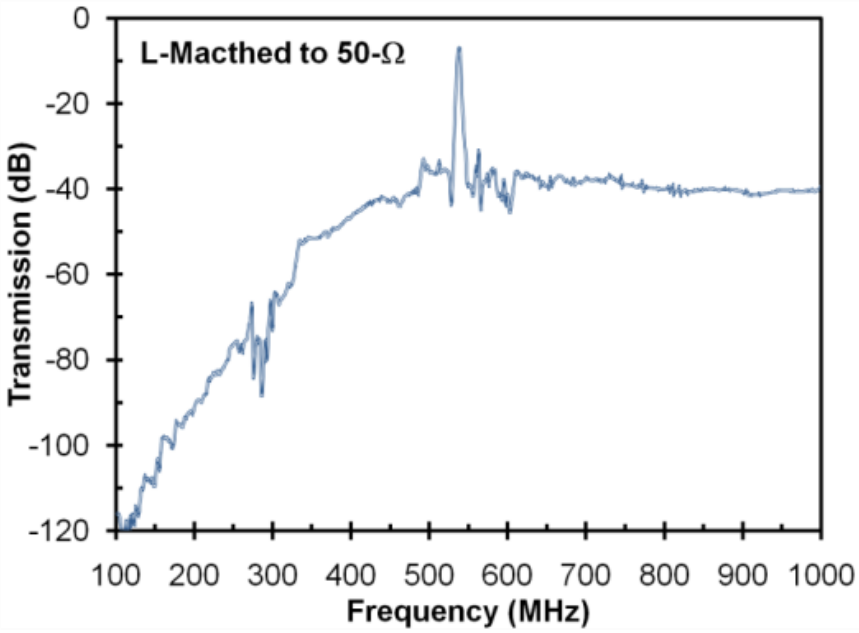

(b)

Figure 5.39 – Wide-band frequency response for the fabricated 536.85 MHz monolithic filter terminated with (a) a 377 Ω resistor, or (b) a L-matching network with element values shown in Figure 5.37

Filters operating at higher frequencies can be designed and implemented by reducing the pitch size of the interdigitated electrode to excite higher order extensional contour mode. In the meantime, the motional resistance also decreases as the rectangular plate resonator operates in its higher order, which directly translates to lower achievable insertion loss. From Equation (5.19), if the pitch size for the 140 μm × 50 μm monolithic filter could be decreased to 3 μm, the operating frequency of the filter would approach 1.08 GHz by exciting the 70^{th} length-extensional mode. However, a modal analysis should be performed in order to determine the bandwidth and the optimal width of the plate filter. Moreover, the equivalent impedance of the intrinsic capacitance of the filter must be calculated at the filter center frequency in order to ensure if its value is large enough as compared to the motional resistance of the synthesized filter, to determine the best achievable performance such as insertion loss. Evidentially, acoustically-coupled filter based upon thin film ZnO monolithic resonator operating at even higher frequencies (i.e., >2.4 GHz) would need interdigitated electrodes with sub-micron pitch size, which certainly complicates the manufacturing process and lowers the yield of such devices.

Although the fabricated monolithic filters based on thin film ZnO piezoelectrically-transduced contour-mode resonator have been demonstrated with performance on par with commercially-available SAW devices operating at frequencies up to 600 MHz, the quality factors of its constituent resonator (typical ~1000) is not sufficient for certain applications where small percentage bandwidth are needed (e.g., 170 MHz GSM filters for handset with *BW* of 200 KHz). Furthermore, if such filters are required to operate at gigahertz frequencies, their fabrication process would be quite challenging due to the need for sub-micron interdigitated electrode fingers to reach such

operational frequencies. To solve this problem, a low acoustic loss material such as single crystalline silicon is introduced in the resonator structural material to enhance its overall quality factor, thus allowing the synthesis of acoustically-coupled filters with very narrow bandwidths. Based on the same design methodology as presented earlier, the first resonance mode of the structure can be calculated based on the fundamental frequency equation for a rectangular plate contour-mode resonator, and the target filter bandwidth is the determined by means of modal analysis using FEM simulations.

Figure 5.40 shows the frequency response for a ZnO-on-SOI acoustically-coupled filter designed to operate at 170 MHz for GMS handset applications. The discrepancy between the expected and the measured center frequency of the filer is due to the misalignment between the structural layers and deviation in the thickness of the piezo-film and the electrode layers from their target values, which has a secondary effect on the center frequency of the filter. The measured 3 dB bandwidth of the filter is 380 kHz, which is on par with the aimed 200 kHz bandwidth needed for GSM handset applications in this particularly frequency range. Figure 5.41 shows the measured passband of the fabricated filter within lower frequency span. As can be noted, the insertion loss of the filter is 6.8 dB with less than 0.5 dB ripple in the passband. This result is quite good for a filter with such small bandwidth. The extracted equivalent electrical parameters for this filter are listed in Table 5.5.

It can be clearly noted in the measured frequency response shown in Figure 5.40, that the notches before and after the filter passband are prominent. The appearance of these notches is dependent on the feedthrough capacitance of the substrate. This particular filter has a relatively large extracted feedthrough capacitance C_f of 10 fF as

shown in Table 5.5. The reason for this unusually large feedthrough capacitance is due to the employment of the sputter-deposited ZnO thin film as both structural and piezoelectric transducer layer for the filter implementation. The higher the resistivity of the piezoelectric film, the better is the isolation between the input and the output ports of the filter as a result of reduced feedthrough capacitance. As detailed in the previous section, the feedthrough capacitance for the capacitively-coupled filters operating at frequencies below 200 MHz does not exceed 2 fF. The value of the feedthrough capacitance limits the best achievable insertion loss.

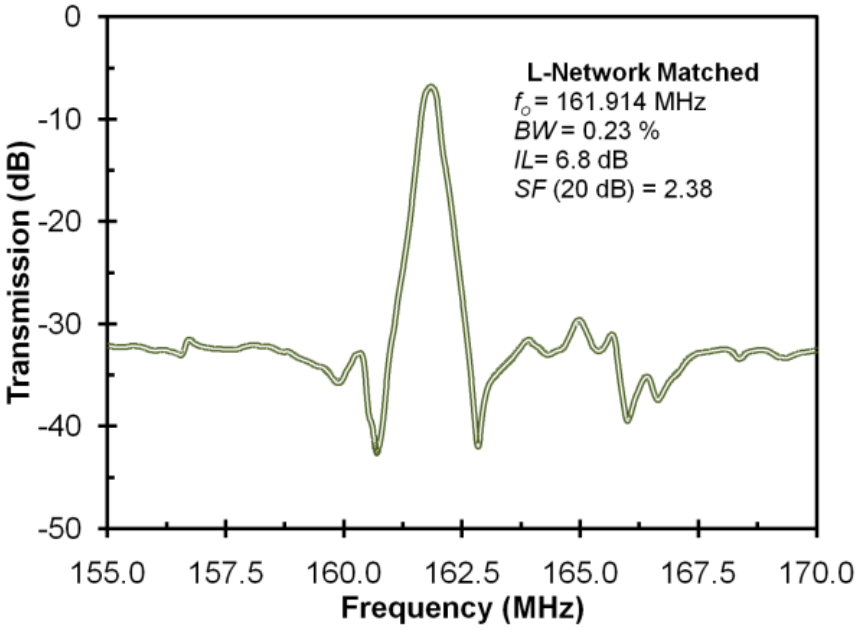

Figure 5.40 – Frequency response for a ZnO-on-SOI acoustically-coupled filter operating at 161.914 MHz fabricated using a SOI wafer with a 5 μm-thick silicon device layer

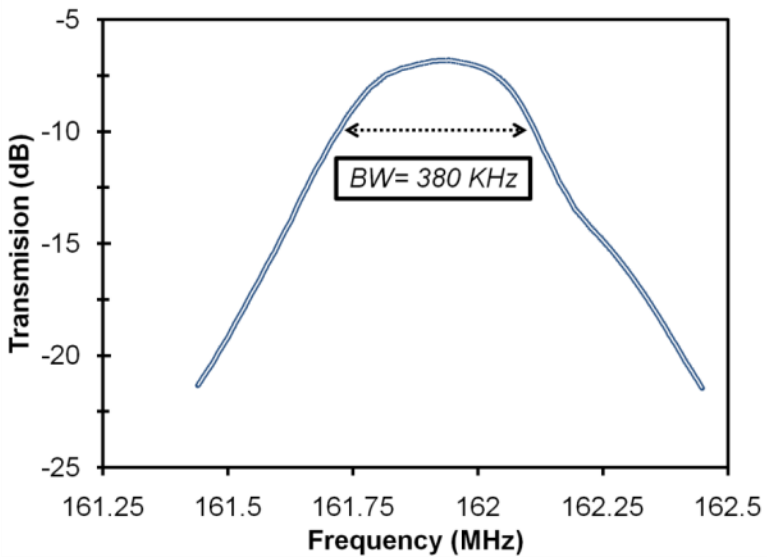

Figure 5.41 – Measured frequency response of the fabricated ZnO-on-SOI acoustically-coupled filter operating at 161.914 MHz within a small frequency span

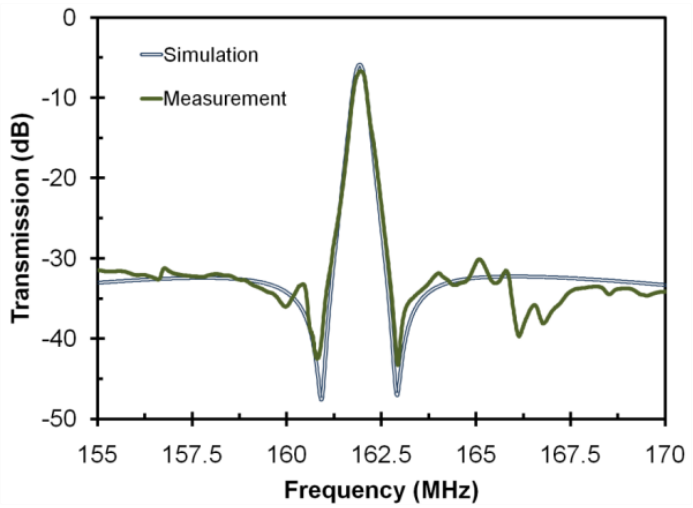

(a)

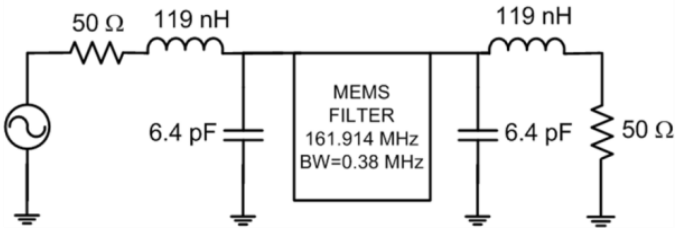

(b)

Figure 5.42 – (a) Simulated vs. measured frequency response of the ZnO-on-SOI acoustically-coupled filter operating at 161.914 MH;(b) L-matching circuit used to match the 161.914 MHz filter to 50 Ω

Table 5.5 – Equivalent electrical parameter of the acoustically piezo-on-silicon coupled filter operating at 161.914 MHz

Parameter	Value
R_m	900 Ω
C_m	1.0908 fF
L_m	884.6 µH
L_c	1.2 µF
C_f	10 fF

For comparison purposes, the frequency response for a commercial IF 170.6 MHz SAW filter from TriQuint is presented in Figure 5.43. Both MEMS and SAW filters exhibit a comparable performance in terms of insertion loss, bandpass ripple, bandwidth and shape factor. Although the out-of-band rejection of the SAW filter is superior, the out-of -band rejection of the MEMS filters can be improved by implementing a substrate isolation scheme such as Faraday cage [77], or engineering the substrate through other means [78].

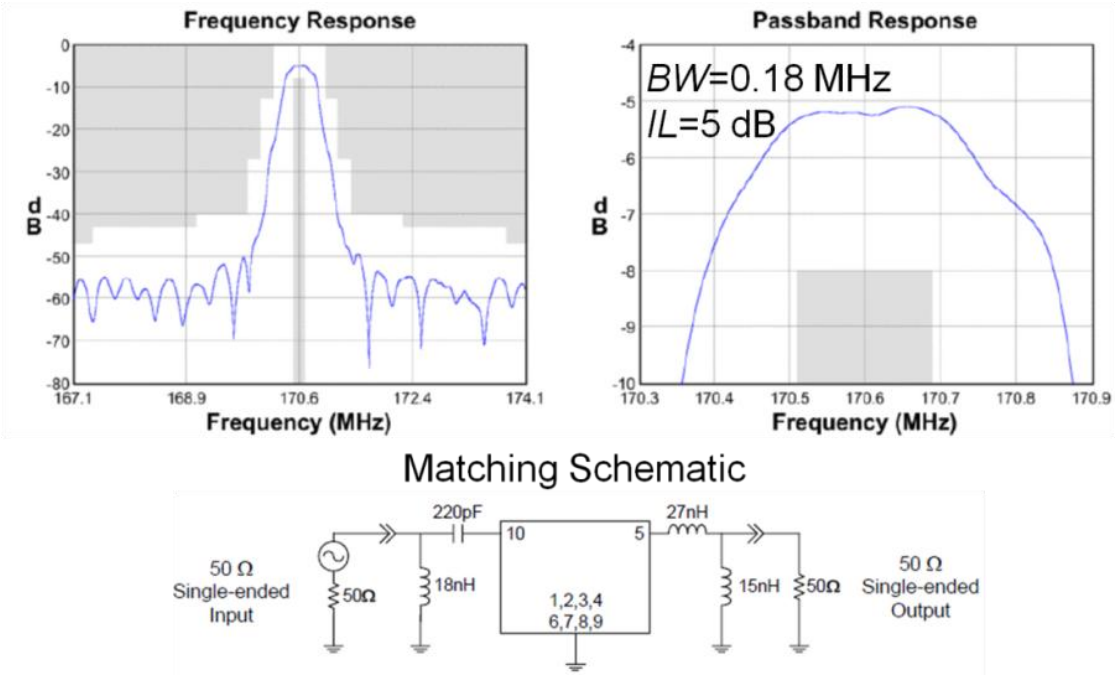

Figure 5.43 – Frequency response and matching circuit diagram for a 170.5 MHz SAW filter designed for GSM/EDGE applications (from TriQuint [75])

Figure 5.44 shows the frequency response for two fabricated 161.914 MHz monolithic filters with the same length and similar electrode configuration. However, the width of the second filter was decreased from 300 µm to 290 µm. As expected, its bandwidth was increased more than two times by reducing the resonator width, which basically demonstrated that the bandwidth of an acoustically-coupled filter can be precisely designed by tweaking the device width. Also shown, the insertion loss and the out-of-band rejection of the second filter remained the same. This is mainly due that the dimensions of both filters are practically identical (90 µm × 300 µm for the first filter and 90 µm × 290 µm for the second filter). However, it is important to mention that increasing even further the bandwidth of this filter would require a major change in its width, thus reducing the total are cover by the electrode top, which ultimate results in an increment of the motional resistance of the filter. The increase in the motional resistance of the filter will affect directly the value of the termination impedance or the components values of the L-matching network. If the 90 µm × 300 µm device is fabricated using a 20 µm SOI wafer, the frequency of this filter is higher due that the loading effect produced by ZnO layer and electrodes is lower for devices thicker silicon structural. Moreover, the quality factor of the constituent resonator is higher due that a major part of the structure is made of low loss acoustic material, enabling a narrow passband.

Figure 5.45 shows the frequency response for the 90 µm × 300 µm monolithic filter fabricated in a SOI wafer with a 20 µm-thick silicon device layer. As expected, the new central frequency for the filter is 213.319 MHz, which is higher as compared when the same device was fabricated in a 5 µm SOI wafer. Also, is noticed that the usable bandwidth of the filter is 200 kHz, which fulfill the requirements for GSM/EDGE

applications in the band of 200 MHz. Comparing this device with a similar filter implemented with a medium scale integration (MSI) micromechanical differential disk-array filter, the one presented on this work is far superior in size, simplicity and performance. The micromechanical differential disk-array filter solution requires 128 resonators connected in a differential configuration; also it needs a polarization voltage of 8 V in order to activate the device. Moreover, the device required to be operated in vacuum, which is impediment if such solution is used to replace SAW filters for GSM applications, which do not require vacuum in order to operate properly. On the contrary, the fabricated device on this work has comparatively the same performance as a commercial SAW filter operating at the same frequency range, but with the advantages of a smaller size and lower insertion loss in such small bandwidth (200 kHz).

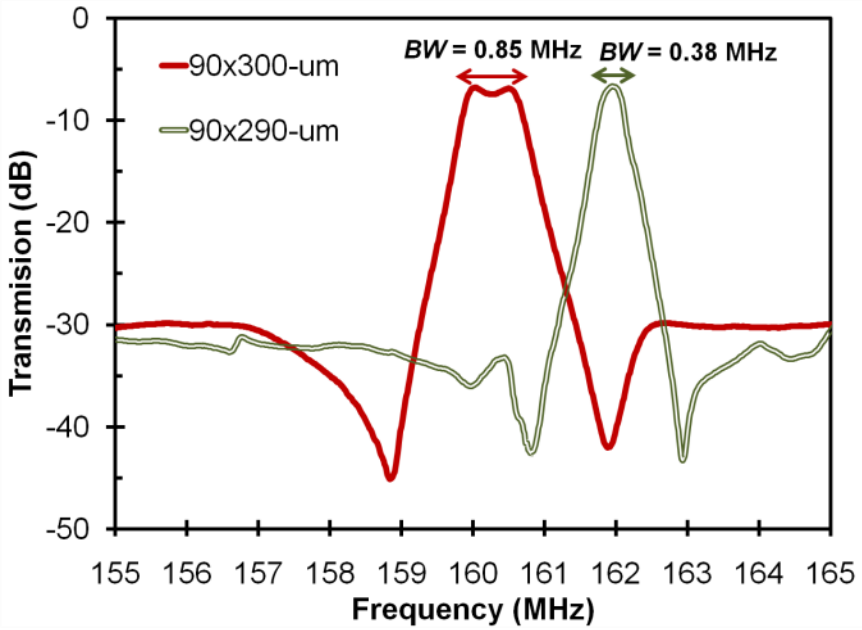

Figure 5.44 – Comparison of the frequency responses for the fabricated 161.914 MHz ZnO-on-SOI acoustically-coupled filters with the same length but different width dimensions

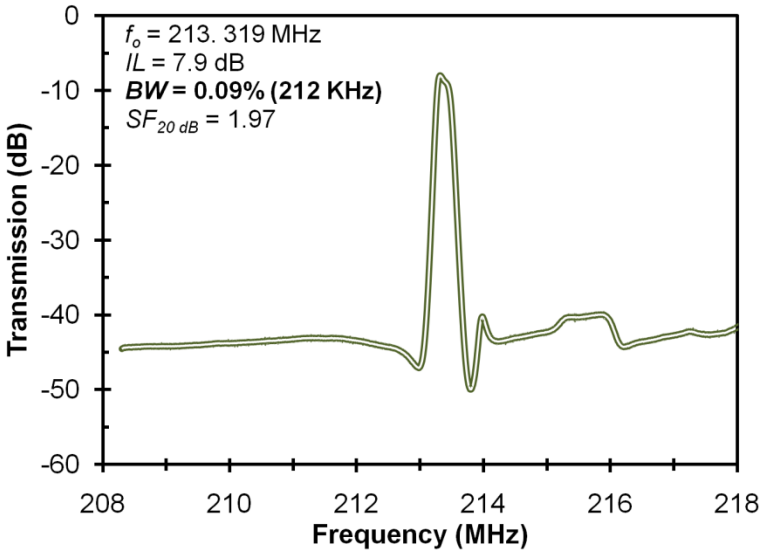

Figure 5.45 – Frequency response for a ZnO-on-SOI acoustically-coupled filter operating at 213.319 MHz with 0.09% percentage bandwidth fabricated in a SOI wafer with a 20 µm-thick silicon device layer

Figure 5.46 shows the frequency response for a ZnO-on-SOI monolithic filter fabricated using a SOI wafer with a 5 µm-thick silicon device layer. The dimensions of this device are 80 µm × 120 µm, with a finger pitch size of 16 µm, operating in the 5th order length-extensional mode. The filter has been coupled to 50 Ω source and termination impedances using the L-matching circuit shown in Figure 5.46(b). The length of this filter is 10 µm shorter than that of the other two filters presented in Figure 5.44 and Figure 5.45, which confirms that frequency can be changed by adjusting one of the lateral dimensions. Figure 5.47 presents the measured frequency response for this filter across a wide frequency scan between 100 MHz and 1 GHz for the same filter displaying no interfering spurious responses. The performance of this filter is on par with a similar commercial SAW device operating at the same frequency range but with a 10 times smaller size. Given its small size, this filter technology will allow the use of chip-level

packaging that would be promising for reducing the total chip area occupied by the filters in current and future communications transceiver.

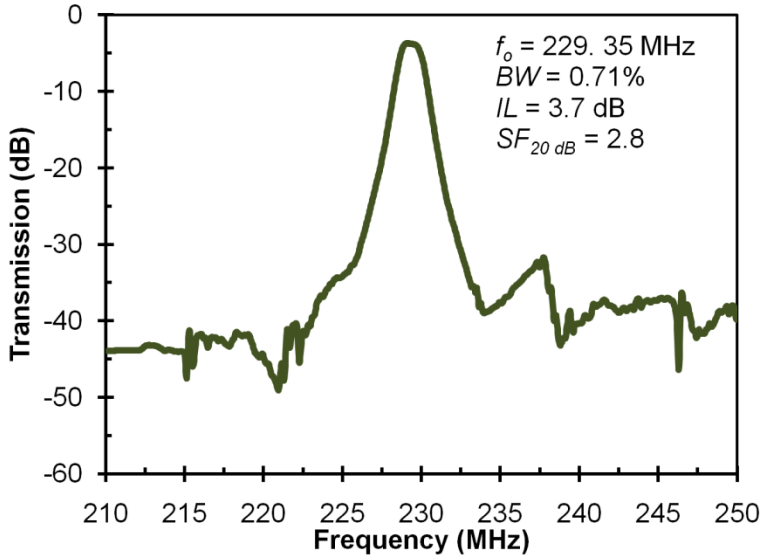

(a)

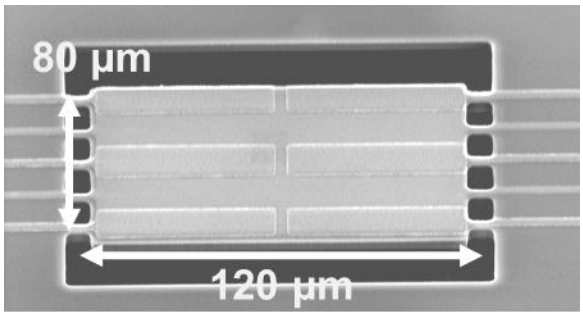

(b)

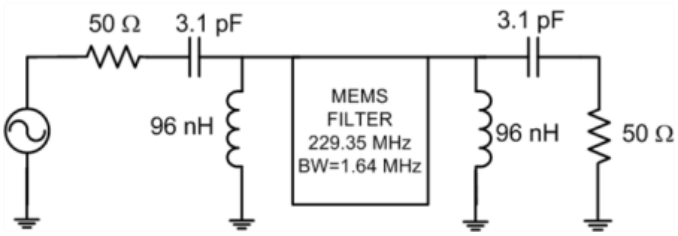

(c)

Figure 5.46 – (a) Frequency response for the fabricated 229.35 MHz monolithic filter; (b) SEM micrograph of the fabricated filter ; and (c) L-matching circuit used to terminate the filter to 50 Ω

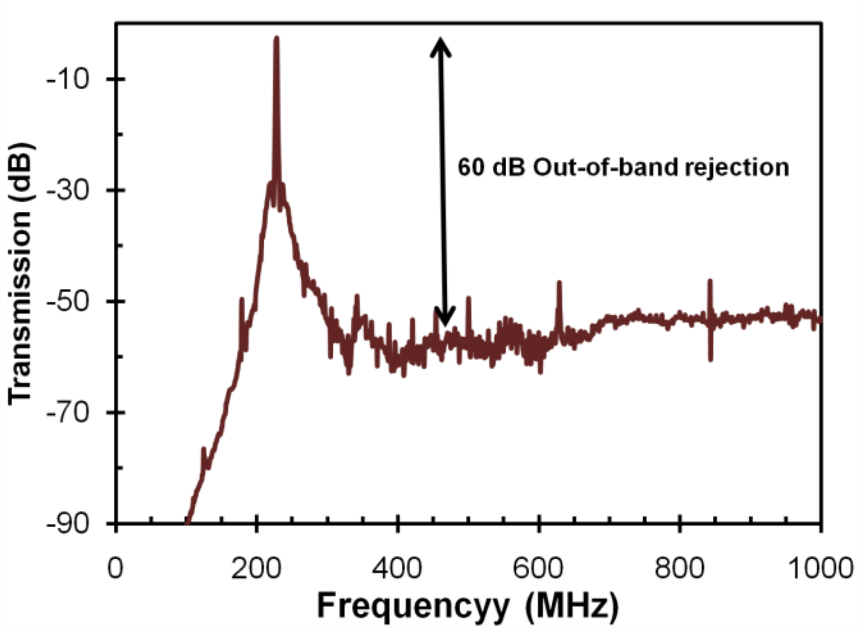

Figure 5.47 – The measured wide-span frequency response between 100 MHz and 1000 MHz of the 229.35 MHz monolithic filter showing no interfering spurious responses

Figure 5.48 and Figure 5.49 show the frequency response for a monolithic filter with 200 µm × 100 µm dimensions, working in the 39th and 43rd order length-extensional mode. The filters have been coupled to 50 Ω using a L-matching circuit. Although the out-of-band rejection characteristics of these filters were comparably lower than similar commercial solutions implemented with SAW and FBAR resonators, they exhibited low insertion loss for the required bandwidth needed for channel-select filters in the UHF range. For wideband filter applications in the UHF range, such as broadband wireless applications with target bandwidth between 10 MHz-100 MHz, contour-mode resonators can be still used to implement filters in a ladder configuration similar to that of FBAR filters. While these configurations have been already demonstrated in the VHF range [30], they have not been implemented yet using this technology in the UHF range. However, the ability of contour-mode resonators for realizing the small frequency offset needed by the ladder filter configuration through the lithographically-defined mass

loading of the top electrode, open the possibility to implement such a design at UHF frequency range.

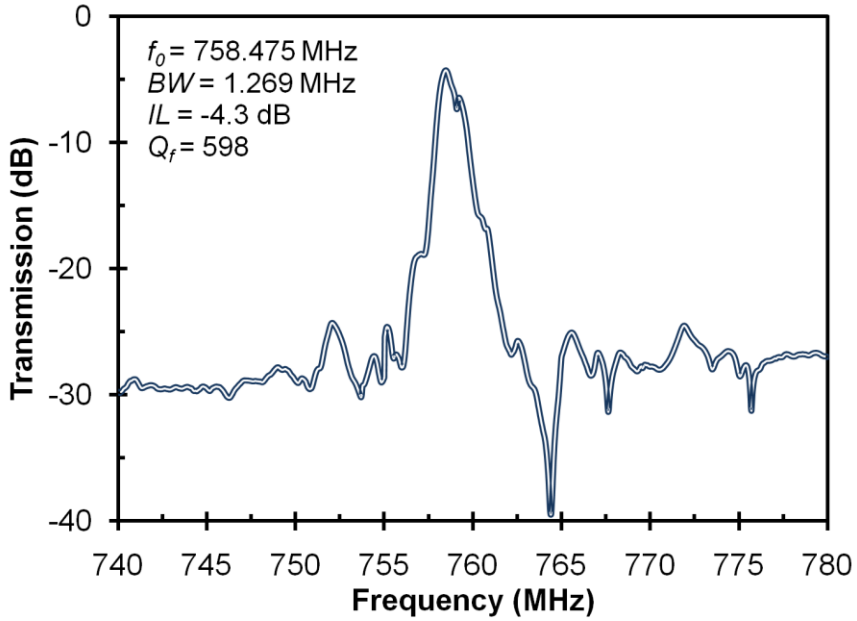

Figure 5.48 – Measured frequency response for the fabricated 758.6 MHz monolithic filter

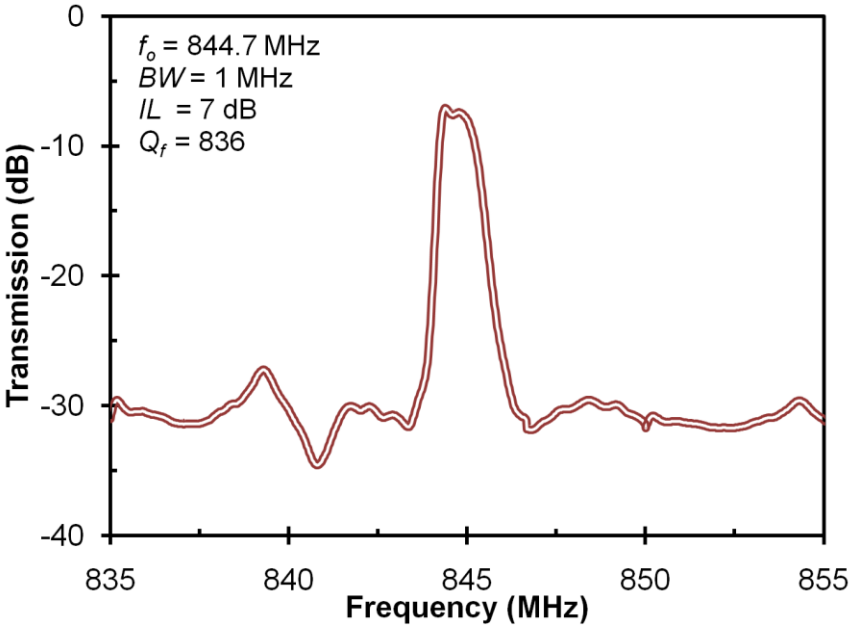

Figure 5.49 – Measured frequency response for the fabricated 844.7 MHz monolithic filter

In general, the procedure for the design of monolithic is described by the following steps:

- Calculate the resonator dimensions based on the center frequency and bandwidth needed for the target applications using the fundamental frequency equation for the piezoelectric resonator and modal analysis using FEM simulation.
- Fabricate and characterized the synthesized filter for the purposes of determining the effects of the actual material properties and the effect of the spurious modes in the proximity of the desired resonance frequency. It is worth mentioning that a multi-physics electromechanical simulation for the frequency response can be performed in order to predict the presence of the spurious mode, which would significantly reduce the cost of the research and development by avoiding the prototyping.
- Based on the preliminary measurement results, analyze the target filter specifications against the characteristics of the fabricated devices to tweak and finalize the design if necessary.

5.4 Intermodulation Distortion

Intermodulation Distortion (IMD) is a phenomenon caused by the non-linear response of a system or a device when multiple signals with closely spaced frequencies are fed into its input, which produce undesired outputs at frequencies that may turn out to be harmful [79]. In a wireless transceiver, this may cause that signals in one channel to interfere with those in an adjacent channel.

The fast-evolving wireless communication market has demanded a more aggressive usage of the overly crowded frequency spectrum, as the number of wireless

communication services has notably increased in the past years. In particular, the wireless communication channels need to be more tightly spaced in frequency. Therefore, filters with a narrow bandwidth, low insertion loss and minimum intermodulation distortion become absolutely critical for the current and future generations of communication systems.

The most common way to measure two-tone third-order intermodulation distortion is to feed the device under test with a signal composed of a combination of two tones of equal power and closely-spaced frequencies with a small frequency offset of Δf. A typical output frequency spectrum is presented in Figure 5.50.

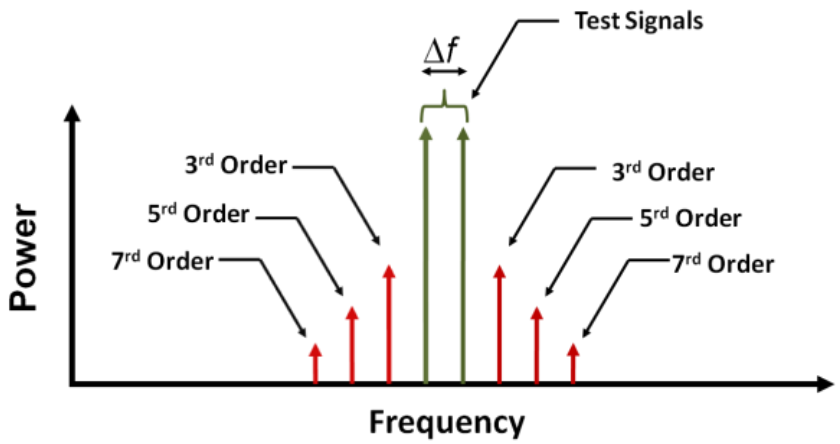

Figure 5.50 – Output spectrum of Two-Tone Intermodulation Test

From the signals shown in Figure 5.50, the 3rd order intermodulation product (IM3) is the most relevant term, since it is the closest interference to the test signals an its output power increases three time faster with the input power as compared to the test signals [79].

The third-order intercept point (IP3) for the fabricated piezoelectrically-transduced filters developed in this work has been measured using the two-tone technique

by feeding the device under test with two sine wave tones spaced with Δf and $2\Delta f$ offsets from the central frequency of the filter f_0 as follows:

$$f_1 = f_0 - \Delta f \tag{5.20}$$

$$f_2 = f_0 - 2\Delta f \tag{5.21}$$

where Δf has been set to 200 kHz to assure that the signal generated by the third intermodulation (IM3) falls within central frequency of the filter. The IP3 is defined as the crossing point of the linear extrapolations of the output powers of the fundamental signal and the IM3 signal with respect to input power of the fundamental signal. The IP3 is a useful measure of the device linearity, the higher the crossing point, the better the linearity of the device is. The measurement setup for the two-tone third-order intermodulation distortion is shown in Figure 5.51.

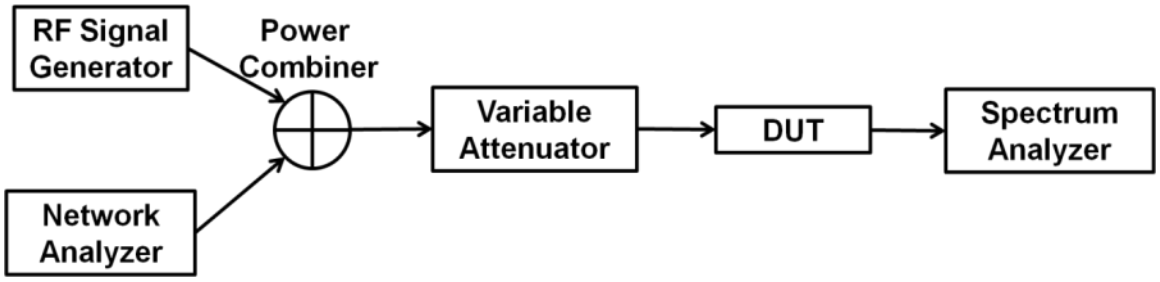

Figure 5.51 – Block diagram of two-tone intermodulation distortion measurement setup

Figure 5.52 shows the measured input intercept point (IIP3) for a thin-film ZnO piezoelectrically-transduced filter operating at 481.2 MHz. This measured IIP3 is comparable to existing SAW devices [73][80] operating at the same frequency range, which is also on par with AlN-based resonators and filters [81]. The measured IIP3 for piezoelectrically-transduced filters developed in this work is superior to that of any capacitively-transduced micromechanical resonators and filters reported to date [82][83][84]. For instance, an IIP3 of 19.49 dBm for a 157.89 MHz micromechanical

disk resonator has been reported previously. It is worth mentioning that the IIP3 value for capacitively-transduced resonators depends on the polarization voltage as it has been demonstrated [82], which is a real disadvantage for implementation of filters and oscillators. However, the use of an electric potential may be beneficial for some applications that require non-linearity such as mixing, given that the linearity of the device can be adjusted by changing the DC bias voltage.

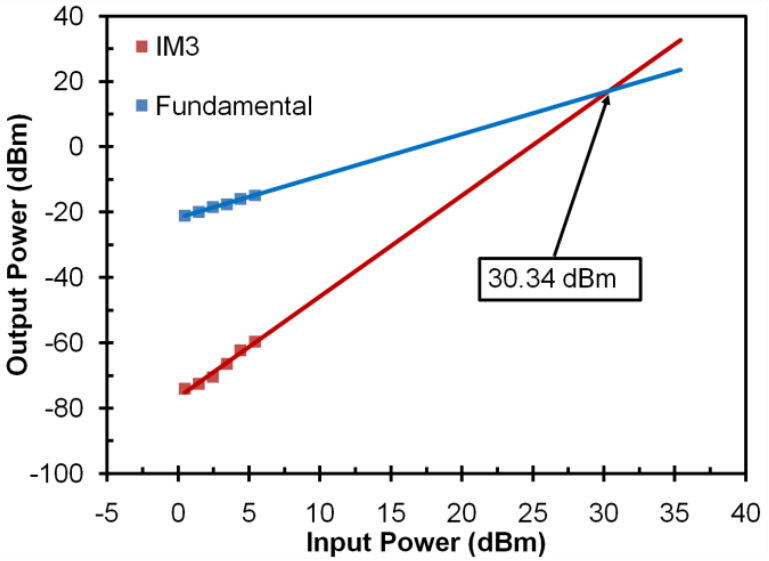

Figure 5.52 – Measured IIP3 data for a piezoelectrically-transduced contour-mode rectangular plate filter with dimensions of 140 µm × 50 µm, operating at 481.2 MHz

Figure 5.53 shows the measured IIP3 data for a ZnO-on-SOI resonator operating at 229.35 MHz. The measured IIP3 of 35.51 dBm is 5 dBm higher than the one measured for thin-film ZnO piezoelectric counterparts. The improvement can be ascribed to the fact that major part of the resonant body is composed of a non-piezoelectric material, thus reducing the non-linear effects introduced by the piezoelectric transducer thin film.

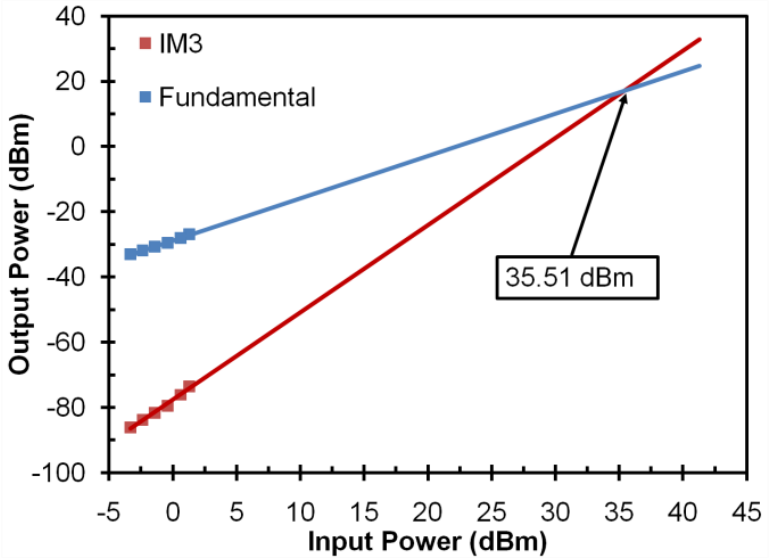

Figure 5.53 – Measured IIP3 data for a ZnO-on-SOI acoustically-coupled rectangular filter with dimensions of 80 µm × 120 µm operating at 229.35 MHz

Figure 5.54 shows the measured IIP3 data for a mechanically-coupled ZnO-on-SOI filter operating at 71 MHz. This filter consists of an array of 10×2 resonators, mechanically-coupled together by $\lambda/4$-long coupling beams. The measured IIP3 value for the mechanically-coupled filter is fairly similar to the one presented in Figure 5.53 for an acoustically-coupled filter that consists of a single contour-mode resonator. This result strongly indicates that IIP3 values do not have strong correlation with the specific type of filter configuration (i.e., mechanically-coupled, capacitively-coupled, and acoustically-coupled topologies) and the number of constituent resonators. Furthermore, several mechanically-coupled resonator filters have been measured with different number of constituent resonators, including 4×2, 4×4, 8×4, 10×2 and 10×4 resonator arrays. However, no significant differences were observed between filters constructed with a single resonator or arrays of mechanically-coupled resonators as shown in Figure 5.55.

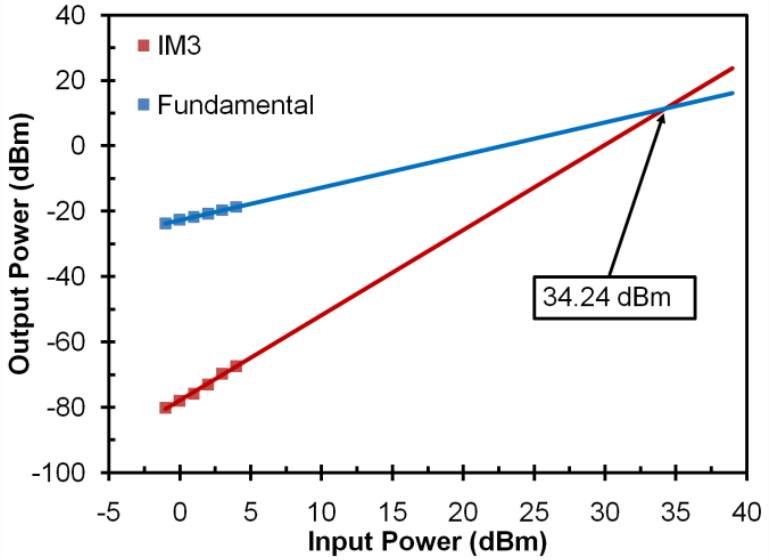

Figure 5.54 – Measured IIP3 data for piezo-on-silicon mechanically-coupled filter operating at 71 MHz composed of 10×2 array contour-mode resonators

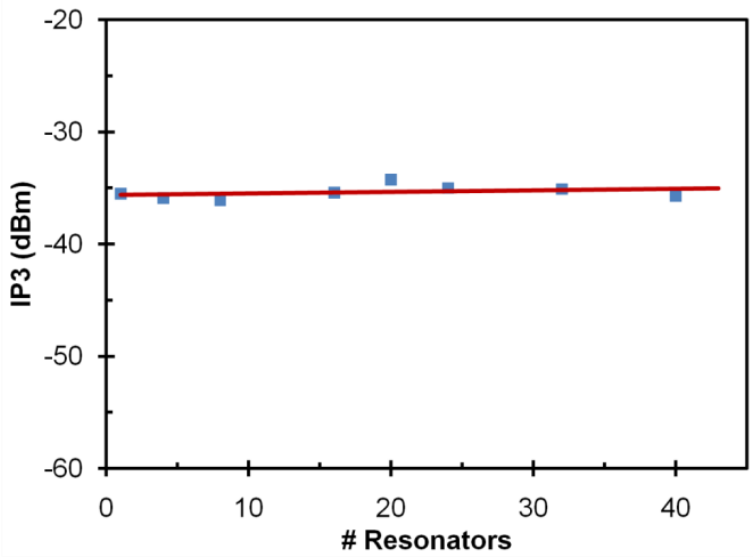

Figure 5.55 – Measured IIP3 data for a piezo-on-silicon filter with different number of resonators mechanically-coupled into an array

5.5 Group Delay

The group delay is an important parameter of any RF and microwave system (e.g., filters, amplifiers, mixers, interconnect, etc.) that describes the phase response of a signal while it passes through a network [86]. The group delay is a good measure of how the

phase response of the system creates some time distortion in the transit signal. The group delay is also defined as the transient time of a signal through a device versus frequency. Mathematically, the group delay is defined as [64]:

$$\text{Group Delay}(t) = \frac{-d\phi}{d\omega} \tag{5.22}$$

where ϕ represents the phase and ω represents the angular frequency. Figure 5.56 shows a representation of the group delay in an arbitrary filter and some important characteristics of its phase response.

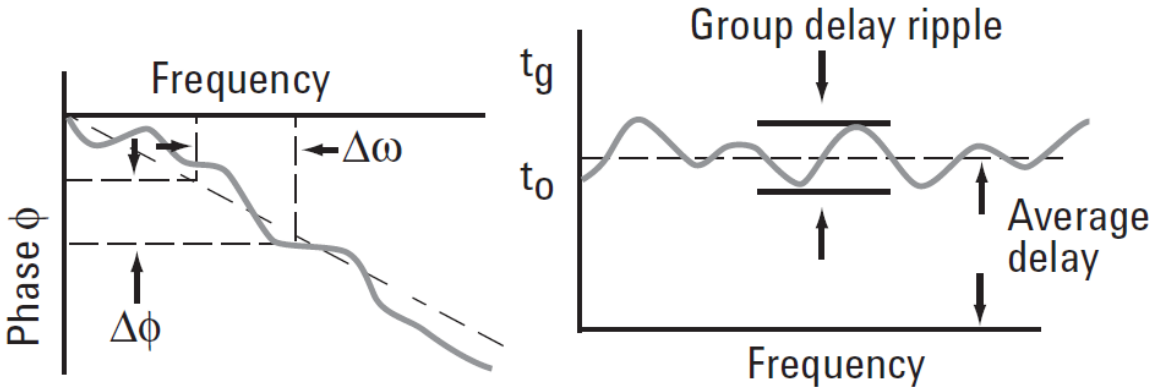

Figure 5.56 – Conceptual illustration of the phase delay and group delay

As shown by the conceptual illustration in Figure 5.56, the group delay response of a filter simply quantifies how much a filter characteristic deviates from a linear phase response. A linear phase response implies a flat or frequency-independent group delay. This is calculated by the derivative of the filter phase with respect to the angular frequency (ω) as presented in Equation (5.23). The group delay value at a single frequency within the filter's passband is just a measure of how much time it would take for a sine-wave signal to pass through the filter. The difference in group delay for signals contained in the filter's passband is considered a direct measure of the phase distortion introduced by the filter. Therefore, constant average group delay and small group delay

ripples are expected to maintain low distortion characteristics. For any transceiver systems, large group delay variations may cause inter-symbol interference in digital modulated signals, thus directly affecting the quality of the transmitted signal. From the system design perspective, the ripple of the group delay needs to be kept below an acceptable level [88].

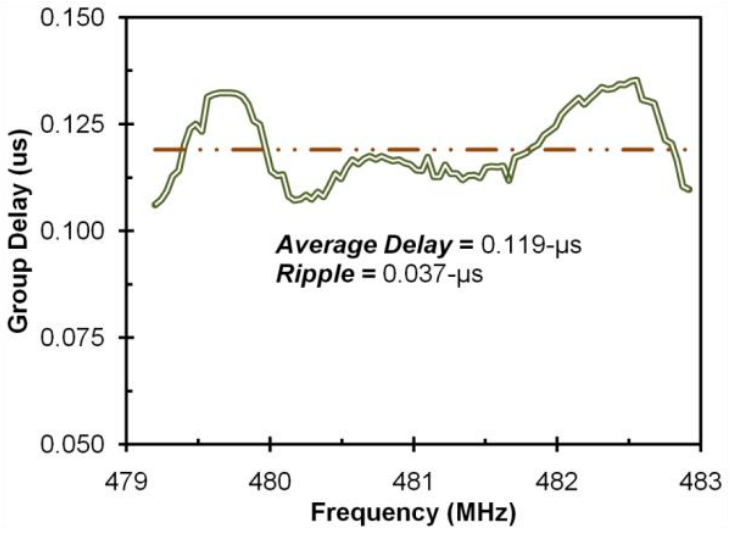

(a)

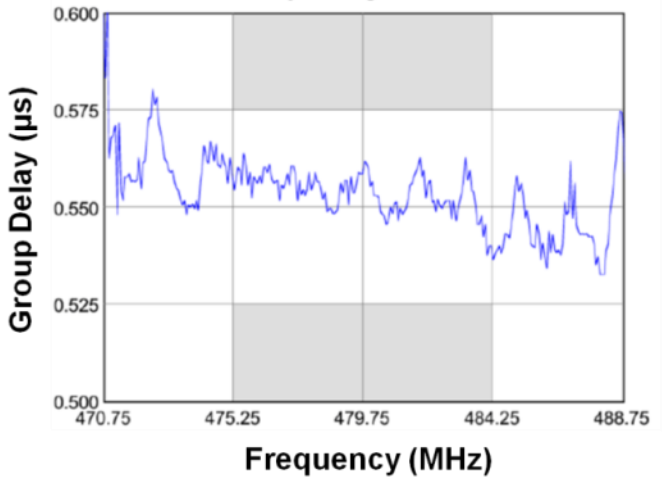

(b)

Figure 5.57 – (a) Group delay variation for the 581.56 MHz piezoelectrically-transduced MEMS filter; (b) Group delay variation for a commercial 479.5 MHz SAW filter (Part Number 855271 from TriQuint [73])

For the purpose of comparing the performance in terms of group delay for the filters developed in this work and the current state-of-the-art filter technologies available in the market, Figure 5.57 shows the extracted group delay for the synthesized 481.56 MHz piezoelectrically-transduced monolithic filter as well as a commercial SAW filter from TriQuint operating in the frequency range. From Figure 5.57, it can be seen that the group delay for the fabricated monolithic MEMS filter is 4.6 times lower than that of the SAW filter on the order of 0.431-μs. The obvious reason for the improvement is that the fabricated piezoelectrically-transduced MEMS filter has a smaller size than the SAW filter, which is expected as signals experienced less phase delay in a smaller component. With regard to the group delay variation (ripple), the piezoelectrically-transduced MEMS filter exhibited a slight improvement in the group delay variation (0.037 μs for the piezoelectric filter and 0.040 μs for the SAW filter).

Figure 5.58 compares the extracted group delay for a 161.9 MHz ZnO-on-SOI piezoelectrically-transduced filter and a commercial SAW filter from TriQuint operating at similar frequencies. As expected, the group delay for the MEMS filter is two times lower than that of the SAW filter counterparts. The group delay variation for the MEMS filter is 0.232 μs as compared to 0.4 μs for the commercial SAW filter.

Unfortunately, a comparative analysis against capacitively-transduced filters could not be performed because the group delay data has not been reported in literature for this kind of devices. Extraction of the group delay requires parameters obtained from S-parameter measurements, and more precisely the phase of the measured insertion loss (i.e., S_{21} or S_{12}, depending of the nomenclature selected for the input and output of the filter).

It is important to highlight that the comparison between the filter developed by this work and commercial SAW device are both bandpass filters operating at similar frequencies. One can certainly assert that MEMS filters based on piezoelectrically-transduced contour-mode resonators exhibit as good performance in terms of group delay variation as their SAW counterparts.

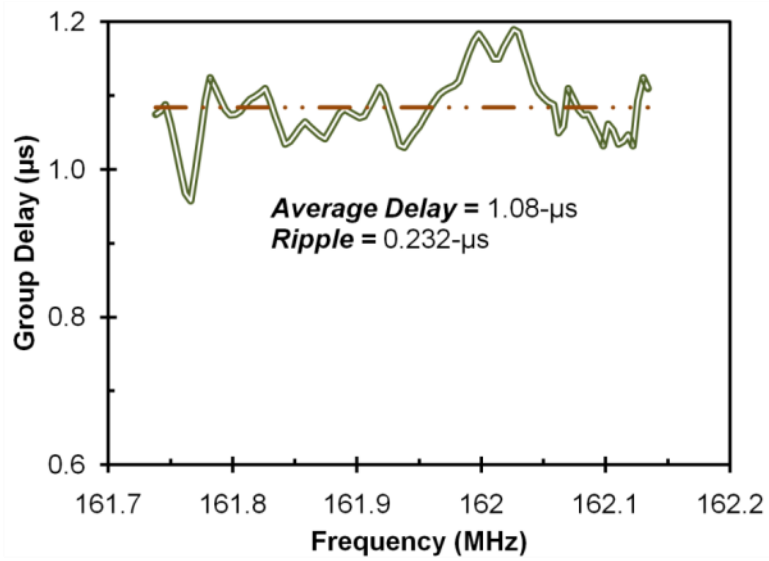

(a)

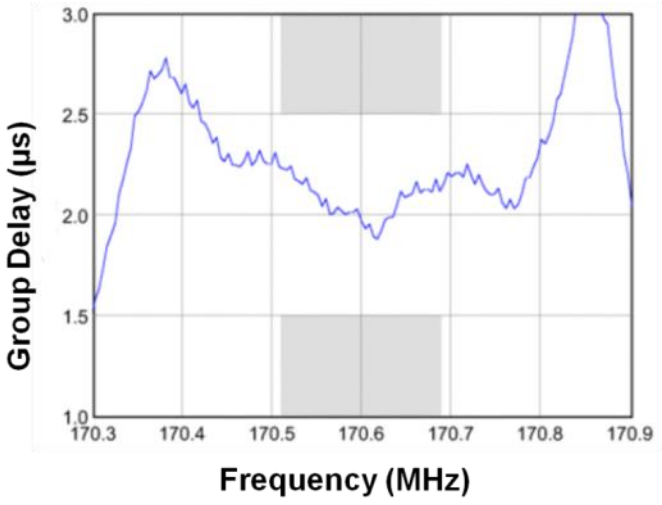

(b)

Figure 5.58 – (a) Group delay variation for the 161.91 MHz MEMS filter; (b) Group delay variation for a commercial 170.6 MHz SAW filter (Part Number 856447 from TriQuint [75])

5.6 Performance Comparison of Piezoelectric Contour-Mode MEMS Filters

An analysis of the performance of the mechanical, capacitive and acoustical coupling schemes used for the implementation of VHF and UHF filters based on piezoelectrically-transduced resonators is presented in Table 5.6.

Table 5.6 – Performance comparison for mechanically, capacitively and acoustically coupled filters based on contour-mode piezoelectrically-transduced resonators

Filter Configuration	Operational Frequency	BW	Motional Resistance	Insertion loss	IIP3	Resonator #
Mechanically-Coupled	10 MHz - 500 MHz	0.1 - 5 %	< 1 kΩ	2-5 dB	> 30 dBm	≥ 2
Capacitively- Coupled	10 MHz - 500 MHz	0.1 - 5 %	< 1 kΩ	2-5 dB	> 30 dBm	≥ 2
Acoustically-Coupled	50 MHz - 10 GHz	0.05 - 5 %	< 1 kΩ	2-8 dB	> 30 dBm	1

In terms of insertion loss, motional resistance and linearity, the three filter configuration implemented in the preset work show similar performance. For applications where high power handling is needed (i.e., >20 dBm) and device size is not a constraint, mechanically-coupled filter arrays are the optimal solution due that the power handling of the filter can be incremented by rising the number of sub-filter arrays without affecting the device linearity and the insertion loss. For applications where the out-of-band rejection and the shape factor of the filter are the most important parameters, capacitively-coupled filter can be synthesized using piezoelectrically-transduced contour-mode resonators with 20 dB shape factors as good as 1.5 and out-of-band rejection as high as 60 dB with the use of three or four resonator electrically cascaded. Subsequently, for narrow band filters (i.e., BW ~0.01 %) , two closely-spaced orthogonal resonances from a single piezoelectrically-transduced plate resonator vibrating in a length-extensional mode can be used to generate a 2^{nd} order 2-pole filter without the need for multiple resonators. Filters synthesized using this scheme have been demonstrated in the

present work with bandwidth as small as 0.09% for frequencies in the order of 200 MHz, which fulfill the requirements for GSM handsets. Moreover, with the proper design, the operational frequencies of such filters based on the acoustically-coupled technique can be extended at gigahertz frequencies with insertion losses as low as 3 dB.

5.7 Technology Limit of Contour-Mode MEMS Filters and Remarks

At the moment the most widely-deployed RF-MEMS devices are the RF front-end filters and duplexers based on FBAR resonators. There is a general misconception that the FBAR technology does not fall under the category of MEMS. In fact, FBAR resonators are indeed MEMS devices that combine both mechanical and electrical functionalities [89]. The great success of FBAR technology lies in several categories such as its ability to directly interface to 50 Ω systems without external matching networks, the high power handling ability, the high quality factors (currently Avago VI generation of FBAR resonators have *Q's* factor in the order of 5,000 at 2 GHz), and demonstrated low insertion loss from 700 MHz to 4.8 GHz for filters implemented using ladder configuration. Their ability to directly interface with 50 Ω systems comes from the fact that piezoelectric resonators operating in a thickness mode have a terrific electromechanical coupling factor much higher than their contour-mode counterparts, which is the reason behind the low motional resistance of FBAR resonators. Equations (5.23)-(5.26) model the equivalent mass, the stiffness and the electromechanical coupling factor for a FBAR resonator working in its fundamental mode. The complete derivation analysis can be found in [25].

$$M_{eq} = \frac{\rho A h}{2} \tag{5.23}$$

$$k_{eq} = \frac{EA\pi^2}{2h} \tag{5.24}$$

$$\eta = 2\frac{d_{33}A}{h} \tag{5.25}$$

$$R_m = \frac{\sqrt{k_{eq}M_{eq}}}{Q\,\eta^2} \tag{5.26}$$

Assuming a quality factor of 1,000 at 900 MHz, the motional resistance of the device in the example yields to the value of 0.8 Ω. The values of the area, density, Young's modulus, thickness and d_{33} piezoelectric coefficient used for the above example are listed in Table 5.7. Comparing the motional resistance of this particular FBAR with respect to a capacitively-transduced resonator operating in a similar frequency range [17][23][24][90], the ratio is astonishing, even in the best case scenario for a capacitively-transduced device, the motional resistance of a FBAR is 10^6 times lower.

Table 5.7 – Parameters used for the extraction of the motional resistance for a FBAR resonator operating at 900 MHz

Young's Modulus	E (GPa)	330
Density	ρ (kg/m^3)	3200
Area	A (μm^2)	500
Thickness	H (μm)	6
Piezo-Coefficient	d_{33} (pC/N)	1.5

Regarding to the quality factor, capacitively-transduced resonators have demonstrated *Q's* in order of 10^5 for frequencies below 100 MHz. However, for frequencies higher than 800 MHz, their quality factor is in the same order of magnitude of the latest FBAR generation fabricated by Avago [91]. On the other hand, the situation for piezoelectrically-transduced resonators and filters vibrating in contour-modes is more

promising. By taking the device presented in Figure 5.37 as example, the motional resistance for this particular filter operating at 536.85 MHz is predicted to be 553 Ω based on the equations introduced in Section 4.3. This theoretical resistance is in close agreement with the measured 598 Ω motional resistance for the fabricated device. Although this device cannot be interfaced directly to 50 Ω electronics, it can be easily matched using a L-matching circuit as demonstrated for all the filters developed in the present work. With regard to mechanically-coupled piezoelectrically-transduced filters, even though their motional resistances can be lowered at the same level of FBAR, they would still need relative large termination impedance on the order of 1 kΩ or a matching circuit in order to flatten the passband. Although some prior research has demonstrated piezoelectrically-transduced resonators with motional impedance approaching 50 Ω [28][29], these devices have employed one port configuration, which is not well-suited for the implementation of filters.

Based on the best results obtained by this work, it is expected that filters and resonators with motional impedances in the range of 50 Ω can be fulfilled by using piezo-on-silicon resonators and acoustically-coupled monolithic filters configuration. Such devices would have to operate in higher order modes and have relatively large size (a comparable size to FBAR) in order to increase the electromechanical coupling factor. For example, a piezo-on-silicon monolithic filter with a size of 200 μm × 100 μm, fabricated with a stacked 5 μm-thick silicon device layer and 500 nm-thick ZnO piezoelectric transducer layer, operating in its 63rd mode at 1.1 GHz , will have a motional impedance of 86 Ω. However, if the thickness of silicon device layer could be further reduced to 2 μm, the motional resistance of this device could be reduced to 46 Ω, thus allowing its

direct integration to 50 Ω circuitry. Potentially the performance of such devices would be on par with FBAR filters. Given such filter consists of one single MEMS resonator, a considerable lower size and greatly reduced the fabrication cost can be realized.

Now, if the MEMS filter technology developed by this work is compared with the present-day SAW technology, it has already exhibited a comparable performance in terms of insertion loss, shape factor, group delay, bandwidth, linearly, and impedance matching. Furthermore, the small footprints of the MEMS filters do not limit its performance. It is worth mentioning that the cutoff slope of a typical SAW device is a function of the device length, which would cause a trade-off between the required performance for certain applications and the package size limitation imposed by the RFIC industry.

Table 5.8 shows the performance parameters for SAW, BAW, capacitively-transduced filters and for the fabricated piezoelectrically-transduced filters in this work. As can be noted, filters based on piezoelectrically-transduced contour-mode resonators can achieve equal or better performance that the commercially available solutions in terms of operational frequency, bandwidth, insertion loss, linearity and size.

Table 5.8 – Performance comparison for SAW, BAW, capacitive and piezoelectric filters based on contour-mode resonators

Technology	Operational Frequency	BW	Motional Resistance	Insertion loss	Polarization Voltage	IIP3	Size
SAW	40 MHz- 5 GHz	0.1 - 5 %	< 1 kΩ	Low	No needed	> 30 dBm	< 0.2 mm^2
BAW	800 MHz - 10 GHz	1 - 10 %	< 50 Ω	Low	No needed	> 30 dBm	> 1 mm^2
Piezoelectric Contour-Mode Filters	10 MHz - 10 GHz	0.05- 5 %	< 1 kΩ	Low	No needed	> 30 dBm	< 0.1 mm^2
Capacitive Contour-Mode Filters	10 MHz - 10 GHz	0.05- 5 %	> 10 kΩ	High	1-20 V	< 19 dBm	< 0.05 mm2

Chapter 6

Conclusion and Future Work

6.1 Summary and Contributions to the RF-MEMS Field

This dissertation research has investigated the design and implementation of bandpass MEMS filters operating in the VHF and UHF bands with low insertion loss by employing piezoelectrically-transduced contour-mode resonators. Two different types of resonators were explored: Resonators made only of a thin film piezoelectric ZnO film embedded between metallic electrodes, and piezo-on-silicon resonators in which a major part of the structure is made of low acoustic loss acoustic single crystalline silicon.

The devices presented in this dissertation have their resonance frequencies determined by the in-plane dimensions of the micromechanical structures and are excited into vibrations by the transverse (d_{31}) piezoelectric coefficient, allowing the fabrication resonators and filters operating at multiple frequencies on the same substrate. Resonators with low motional impedances and high quality factor at frequencies up to 900 MHz have been demonstrated, which can also serve as a frequency reference devices for the existing transceivers operating in the UHF and VHF bands.

Three different filter coupling topologies based on mechanical, electrical and acoustical coupling techniques have been explored in order to synthesize narrow-band and wide-band filters (i.e., 0.1% - 3%) with low insertion loss, excellent out-of-band and spurious-mode rejection, high linearity and small group delay variation. The filters developed in this work not only exhibited comparable performance to that of the

dominant SAW technology in terms of all aforementioned major filter specifications, but also significantly outperform the current state-of-the-art filters in some of the aspects. For instance, the typical size of a MEMS filter studied by this work is 10 times smaller than its SAW counterpart. It is worth mentioning that the MEMS filters implemented by this work have been successfully matched to 50 Ω electronic using a either termination resistance or L-matching circuit.

Narrow-band piezoelectrically-transduced monolithic filters operating at 481.56 MHz and 549.5 MHz have achieved low motional resistance on the order of 300 Ω, which allows their direct integration with a 377 Ω antenna without the need of external matching components. The incorporation of low acoustic loss material such as single crystalline silicon as the resonator structural material, improves both the linearity and the quality factor of the piezoelectrically-transduced resonators, thereby enabling the implementation of filters with passband as narrow as 200 kHz while meeting the key requirements for GSM/EDGE applications.

In addition, a robust and high-yield microfabrication process for thin-film ZnO and ZnO-on-SOI resonators and filters have been successfully developed. The process is entirely compatible with standard CMOS foundry processing with a low thermal budget with temperature well under 400ºC, which facilitates future monolithic integration between MEMS filters CMOS electronics on the same chip to fulfill single chip transceivers.

6.2 Future Work

The filters implemented in this work have already exhibited similar performance to that of the commercial devices for frequencies below 600 MHz. Nevertheless, there is

still room for improvements for filter synthesis at gigahertz frequencies in terms of insertion loss, bandwidth, and out-of-band rejection. For instance, ladder and lattice filter configurations should be pursued to demonstrate the versatility of filters based on piezoelectrically-transduced contour-mode resonators to achieve wider bandwidth (>5%).

The achieved insertion losses of the MEMS filters in this work are far from being perfect as compared to the best-achievable results from FBAR and BAW technologies. The key limiting factor for the implementation of filters with even lower insertion losses is the moderate quality factor of the sputter-deposited ZnO piezoelectric layer. Although the inclusion of single crystalline silicon as part of the device layer mitigate this problem to some extent, a much better performance could be anticipated if AlN is used as the piezoelectric layer instead of ZnO. Moreover, AlN would cause a less severe loading effect to the silicon resonator body due to their comparable acoustic velocity. With the use of this technology along with AlN piezoelectric layer, filters operating between 1 and 5 GHz can be fabricated, by employing interdigitated electrodes with fingers pitch sizes still above of 1 μm. Moreover, the use of AlN would reduce parasitic feedthrough between the filter input and output ports (at least for frequencies below <1 GHz) due to its high resistivity. Furthermore, the implementation of substrate isolation schemes such as integrated faraday cage and substrate impedance engineering can further mitigate the substrate crosstalk and enhance the out-of-band rejection of piezoelectrically-transduced MEMS filters.

Aside from single crystalline silicon, the use of high acoustic velocity nanocrystalline diamond (NCD) as the structural material along with the thin-film piezoelectric transducer layer stacked on top of resonator body is yet to be explored.

Given that the resonance frequency of contour-mode micromechanical resonators is proportional to the acoustic velocity, chemical vapor deposited nanocrystalline diamond provides the largest boost towards even higher operation frequencies. Although capacitively-transduced contour-mode disk resonators with diamond structural layer have been demonstrated with terrific *Q's* on the order of 10^4 at gigahertz frequencies [58], their motional resistances were on the order of 1 MΩ, which makes it difficult to directly integrate with 50 Ω electronics. On the other hand, the preliminary results for piezo-on-diamond resonators were promising but also far from its ideal performance [33] due to the relatively poor quality of the nanocrystalline diamond layer. It is worth mentioning that the quality and piezoelectric coefficient of the piezoelectric films highly depends on its smoothness and crystalline orientation. If piezo-on-diamond resonators and filters are going to be pursued as possible future work, improved fabrication methods should be employed to provide a smooth nanocrystalline diamond structure layer along with highly c-axis oriented piezoelectric films.

Additionally, the ZnO-on-SOI resonators and filters investigated in the present work have exhibited a temperature coefficient of frequency on par with FBAR and SAW devices. Nonetheless, as the wireless communication applications evolve exponentially, the frequency bands are going to packed ever closer to each other for spectrum efficiency. It will be very critical to develop a simple and viable temperature compensation scheme to for reducing the frequency temperature dependence of such devices without sacrificing their others key performance metrics such as quality factor, insertions loss, and so on.

References

[1] H. C. Nathanson, W. E. Newell, R. A. Wickstrom, and J. R. Davis, "The resonant gate transistor," *IEEE Trans. Electron Devices*, vol. ED-14, pp. 117–133, 1967

[2] W. Hayward and R. Bingham, "Direct Conversion; A Neglected Technique," QST, Nov, 1968, pp 15-17.

[3] M. Brandolini, P. Rossi, D. Manstretta, and F. Svelto, "Toward multistandard mobile terminals - Fully integrated receivers requirements and architectures," *IEEE Transactions on Microwave Theory and Techniques*, vol. 53, pp. 1026-1038, 2005.

[4] D. Jakonis, K. Folkesson, J. Dabrowski, P. Eriksson, and C. Svensson, "A 2.4-GHz RF sampling receiver front-end in 0.18-mu m CMOS," *IEEE Journal of Solid-State Circuits*, vol. 40, pp. 1265-1277, 2005.

[5] Magoon, R.; Molnar, A.; Zachan, J.; Hatcher, G.; Rhee, W.; , "A single-chip quad-band (850/900/1800/1900 MHz) direct conversion GSM/GPRS RF transceiver with integrated VCOs and fractional-n synthesizer," *Solid-State Circuits, IEEE Journal of* , vol.37, no.12, pp. 1710- 1720, Dec 2002

[6] *RF MEMS switches are reliable: a comprehensive technology overview*. (2010). retrieved April 4, 2012, from: http://www.memsjournal.com/2010/07/rf-mems-switches-are-reliable-a-comprehensive-technology-overview.html

[7] *SiTime Ships 20 Million Units of MEMS First™ CMOS Oscillators and Clock Generators.* (2010). Retrieved April 4, 2012, from: http://www.sitime.com/news

[8] *Discera Releases World's Highest Performance Multiple Output MEMS Oscillators.* (2011). Retrieved April 4, 2012, from: http://www.discera.com/news

[9] *RF MEMS switches are reliable: a comprehensive technology overview***.** (2010). Retrieved April 4, 2012, from: http://www.memsjournal.com

[10] R. T. Howe and R. S. Muller, "Resonant microbridge vapor sensor,"*IEEE Trans. Electron devices*, ED-33, 1986, pp.499-596.

[11] Tang, W.C.; Nguyen, T.-C.H.; Howe, R.T.; , "Laterally driven polysilicon resonant microstructures," *Micro Electro Mechanical Systems, 1989, Proceedings, An Investigation of Micro Structures, Sensors, Actuators, Machines and Robots. IEEE*, pp.53-59, 20-22 Feb 1989

[12] C. T.-C. Nguyen and R. T. Howe, “Polysilicon microresonators for signal processing,” *Digest of Papers, Government Microcircuit and Applications Conference,* San Diego, CA, Aug. 15, 1994, pp. 195-198

[13] Kun Wang; Nguyen, C.T.-C.; , "High-order medium frequency micromechanical electronic filters," *Microelectromechanical Systems, Journal of* , vol.8, no.4, pp.534-556, Dec 1999

[14] Kun Wang; Ark-Chew Wong; Nguyen, C.T.-C.; , "VHF free-free beam high-Q micromechanical resonators," *Microelectromechanical Systems, Journal of* , vol.9, no.3, pp.347-360, Sep 2000

[15] A. Wong and C. Nguyen, "Micromechanical mixer-filters ("mixlers")," *IEEE/ASME J. Microelectromechanical Systems*, vol.13, no.1, pp. 100-112, Feb. 2004

[16] J. R. Clark, W.-T. Hsu, and C. T.-C. Nguyen, “High-Q VHF micromechanical contour-mode disk resonators,” in Tech. Digest, *IEEE Int. Electron Devices Meeting*, San Francisco, CA, Dec. 11–13, 2000, pp. 399–402

[17] J. Wang, Z. Ren, and C. T.-C. Nguyen, “1.156-GHz self-aligned vibrating micromechanical disk resonator,” *IEEE Transactions on Ultrasonics, Ferroelectrics, and Frequency Control*, vol.51, no.12, pp. 1607-1628, Dec. 2004

[18] M. A. Abdelmoneum, M. U. Demirci, and C. T. C. Nguyen, "Stemless wine-glass-mode disk micromechanical resonators," in *Micro Electro Mechanical Systems, 2003. MEMS-03 Kyoto. IEEE The Sixteenth Annual International Conference on*, 2003, pp. 698-701

[19] Sheng-Shian Li; Yu-Wei Lin; Yuan Xie; Zeying Ren; Nguyen, C.T.-C.; , "Micromechanical "hollow-disk" ring resonators," *Micro Electro Mechanical Systems, 2004. 17th IEEE International Conference on. (MEMS)* , pp. 821- 824, 2004

[20] M. U. Demirci and C. Nguyen, "Mechanically corner-coupled square microresonator array for reduced series motional resistance," *IEEE/ASME J. Microelectromechanical Systems*, vol. 15, no. 6, pp. 1419-1436, Dec. 2006

[21] Zhili Hao; Pourkamali, S.; Ayazi, F.; , "VHF single-crystal silicon elliptic bulk-mode capacitive disk resonators-part I: design and modeling," *Microelectromechanical Systems, Journal of* vol.13,no.6, pp. 1043- 1053, Dec. 2004

[22] Pourkamali, S.; Zhili Hao; Ayazi, F.; , "VHF single crystal silicon capacitive elliptic bulk-mode disk resonators-part II: implementation and characterization," *Microelectromechanical Systems, Journal of* , vol.13, no.6, pp. 1054- 1062, Dec. 2004

[23] Yu-Wei Lin; Sheng-Shian Li; Yuan Xie; Zeying Ren; Nguyen, C.T.C.; , "Vibrating micromechanical resonators with solid dielectric capacitive transducer gaps," *Frequency Control Symposium and Exposition, 2005. Proceedings of the 2005 IEEE International* , pp.128-134, 29-31 Aug. 2005

[24] Weinstein, D.; Bhave, S.A.; , "Internal Dielectric Transduction in Bulk-Mode Resonators," *Microelectromechanical Systems, Journal of* , vol.18, no.6, pp.1401-1408, Dec. 2009

[25] K. M. Lakin and J. S. Wang, "UHF composite bulk wave resonators, "in *Proc. IEEE Ultrason. Symp.*, 1980, pp. 834–837

[26] R. Ruby, P. Bradley, J. Larson, and Y. Oshmyansky, "PCS 1900 MHz duplexer using thin film bulk acoustic resonators (FBARs)," *Electron. Lett.*, vol.35, no.10, pp. 794–795, 1999

[27] K. M. Lakin, G. R. Kline, R. S. Ketcham, J. T. Martin, and K. T. McCarron, "Stacked crystal filters implemented with thin films," in *Proc. 43rd Annu. Symp. Freq. Contr.*, 1989, pp. 536–543

[28] G. Piazza, P.J. Stephanou, A.P. Pisano, "One and two port piezoelectric higher order contour-mode MEMS resonators for mechanical signal processing", *Solid-State Electronics,* vol.51, pp. 1596–1608, 2007

[29] P. J. Stephanou , G. Piazza, C. D. White, M. B.J. Wijesundara, A. P. Pisano, "Piezoelectric aluminum nitride MEMS annular dual contour mode filter", *Sensors and Actuators A-Physical,* vol.A134, 2007

[30] G. Piazza, P.J. Stephanou, A.P. Pisano, "Single-Chip Multiple-Frequency AlN MEMS Filters Based on Contour-Mode Piezoelectric Resonators", *Journal of Microelectromechanical Systems,* vol.16, no.2, pp. 319-328, April 2007

[31] Abdolvand, R.; Ayazi, F.; ,"High-frequency monolithic thin-film piezoelectric-on-substrate filters" International Journal of Microwave and Wireless Technologies, vol.1, pp 29-35, March 2009

[32] Abdolvand, R.; Lavasani, H.; Ho, G.; Ayazi, F.; , "Thin-film piezoelectric-on-silicon resonators for high-frequency reference oscillator applications," *Ultrasonics, Ferroelectrics and Frequency Control, IEEE Transactions on* , vol.55, no.12, pp.2596-2606, December 2008

[33] Abdolvand, R., "Thin-film piezoelectric-on-substrate resonators and narrowband filters". Ph.D. diss., Georgia Institute of Technology ,2008

[34] M. J. Madou, Fundamentals of Microfabrication 2E. Boca Raton, FL: CRC Press, 2002, p. 560.

[35] Gautschi, G (2002). *Piezoelectric Sensorics: Force, Strain, Pressure, Acceleration and Acoustic Emission Sensors, Materials and Amplifiers.* Springer.

[36] Varadan, V. K., K. J. Vinoy, and K. A. Jose. *RF MEMS and Their Applications*. John Wiley, 2003

[37] Heywang, Walter, Karl Lubitz, and Wolfram Wersing. 2008. *Piezoelectricity: evolution and future of a technology, Walter Heywang, Karl Lubitz, Wolfram Wersing*. Berlin: Springer, c2008, 2008.

[38] Olsson, R.H.; Fleming, J.G.; Wojciechowski, K.E.; Baker, M.S.; Tuck, M.R.; , "Post-CMOS Compatible Aluminum Nitride MEMS Filters and Resonant Sensors," *Frequency Control Symposium, 2007 Joint with the 21st European Frequency and Time Forum. IEEE International* , pp.412-419, May 29 2007-June 1 2007

[39] Piazza, G.; Stephanou, P.J.; Pisano, A.P.; , "Piezoelectric Aluminum Nitride Vibrating Contour-Mode MEMS Resonators," *Microelectromechanical Systems, Journal of* , vol.15, no.6, pp.1406-1418, Dec. 2006

[40] Campanella, Humberto. *Acoustic Wave and Electromechanical Resonators: Concept to Key Applications*. Artech House, 2010

[41] Frederico, S.; Hibert, C.; Fritschi, R.; Fluckiger, P.; Renaud, P.; Ionescu, A.M.; , "Silicon sacrificial layer dry etching (SSLDE) for free-standing RF MEMS architectures," *Micro Electro Mechanical Systems, 2003. MEMS-03 Kyoto. IEEE The Sixteenth Annual International Conference on* , vol., no., pp. 570- 573, 19-23 Jan. 2003

[42] Robert A. Johnson. *Mechanical filters in electronics*. Wiley series on filters. Wiley, 1983

[43] Safari, AhmadAkdogan. *Piezoelectric and acoustic materials for transducer applications*. [Electronic resource]. (2008)

[44] S. Park, B. Seo, G. Yoon, *Two-step deposition process of piezoelectric ZnO films and its application for thin bulk acoustic resonators*, Journal of Vacuum Science and Technology A, 18(5), 2432, (2000)

[45] J. Molarius, J. Kaitila, T. Pensala, M. Ylilammi, *Piezoelectric ZnO films by R.F sputtering*, Journal of Materials Science: Materials in Electronics, 14, 431, (2003)

[46] Piazza, Gianluca. "Piezoelectric aluminum nitride vibrating RF MEMS for radio front-end technology". Ph.D. diss., University of California, Berkeley ,2005

[47] Zhili Hao, Ahmet Erbil, Farrokh Ayazi, *An analytical model for support loss in micromachined beam resonators with in-plane flexural vibrations*, Sensors and Actuators A: Physical, Volume 109, Issues 1–2, 1 December 2003, Pages 156-164

[48] Wang, Jing, "*Self-aligned radial contour mode micromechanical disk resonators for wireless communications*". Ph.D. diss., University of Michigan, 2006.

[49] C. Zener, "Internal friction in solids, I: theory of internal friction in reeds," *Phys. Rev*., vol. 52, pp. 230–235, Aug. 1937.

[50] Abdolvand, R.; Johari, H.; Ho, G.K.; Erbil, A.; Ayazi, F.; , "Quality factor in trench-refilled polysilicon beam resonators," *Microelectromechanical Systems, Journal of* , vol.15, no.3, pp. 471- 478, June 2006

[51] K. F. Graff, *Wave Motion in Elastic Solids*. New York: Dover Publications,Inc.,1991.

[52] Wei Pang; Hongyu Yu; Hao Zhang; Eun Sok Kim; , "Temperature-compensated film bulk acoustic resonator above 2 GHz," *Electron Device Letters, IEEE* , vol.26, no.6, pp. 369- 371, June 2005

[53] Abdolvand, R., "*Thin-film piezoelectric-on-substrate resonators and narrowband filters*". Ph.D. diss., Georgia Institute of Technology ,2008.

[54] Yanagitani, T.; Kiuchi, M.; Matsukawa, M.; Watanabe, Y.;,"P1J-1 Temperature Characteristics of Pure Shear Mode FBARs Consisting of (1120) Textured ZnO Films," *Ultrasonics Symposium, 2006. IEEE* , pp.1459-1462, 2-6 Oct. 2006

[55] W.-T. Hsu and C. T.-C. Nguyen, "Stiffness-compensated temperature insensitive micromechanical resonators," *in Proc. IEEE Int. Conf. MEMS, 2002*, pp. 731–734.

[56] C. T.-C. Nguyen and R. T. Howe, "Microresonator frequency control and stabilization using an integrated micro oven," *Digest of Technical Papers*, the 7th International Conference on Solid-State Sensors and Actuators (Transducers'93), Yokohama, Japan, pp. 1040-1043, June 7-10, 1993.

[57] Samarao, A.K.; Ayazi, F.; , "Temperature Compensation of Silicon Resonators via Degenerate Doping," *Electron Devices, IEEE Transactions on* , vol.59, no.1, pp.87-93, Jan. 2012

[58] Wang, J. "Self-aligned radial contour mode micromechanical disk resonators for wireless communications". Ph.D. diss., University of Michigan ,2006

[59] Pourkamali, S.; Ho, G.K.; Ayazi, F.; , "Low-Impedance VHF and UHF Capacitive Silicon Bulk Acoustic-Wave Resonators—Part II: Measurement and Characterization," *Electron Devices, IEEE Transactions on* , vol.54, no.8, pp.2024-2030, Aug. 2007

[60] Clark, J.R.; Hsu, W.-T.; Abdelmoneum, M.A.; Nguyen, C.T.-C.; , "High-Q UHF micromechanical radial-contour mode disk resonators," *Microelectromechanical Systems, Journal of* , vol.14, no.6, pp. 1298- 1310, Dec. 2005

[61] A.S Sedra and P.O. Brackett, *Filter theory and design: active and passive*, Beaverton: matrix Publisher, Inc, 1978

[62] A. I. Zverev, *Handbook of Filter Synthesis*. New York: John Wiley & Sons, 1967

[63] R. Adler, "Compact electromechanical filters,' *Electronics*, VOl.20, pp.100-105, Apr.1947

[64] D.M Pozar, Microwave Engineering, 3rd ed: John Wiley & Sons, Inc., 2005.

[65] Kyuchul Chong; Xi Zhang; King-Ning Tu; Daquan Huang; Mau-Chung Chang; Ya-Hong Xie; , "Three-dimensional substrate impedance engineering based on p^-/p^+ Si substrate for mixed-signal system-on-chip (SoC)," *Electron Devices, IEEE Transactions on* , vol.52, no.11, pp. 2440- 2446, Nov. 2005

[66] Xie, Yuan. "*Micromechanical extensional wine-glass mode ring resonators for wireless communications*". Ph.D. diss., University of Michigan, 2006.

[67] Li, S.,"*Medium-scale integrated micromechanical filters for wireless communications*". Ph.D. diss., University of Michigan, 2007

[68] P. J. Stephanou, G. Piazza, C. D. White, M. B. J. Wijesundara, and A. P. Pisano, "Mechanically Coupled Contour Mode Piezoelectric Aluminum Nitride MEMS Filters," *IEEE MEMS 2006*, pp. 906-909, 2006

[69] Pourkamali, S.; Abdolvand, R.; Ayazi, F.; , "A 600 kHz electrically-coupled MEMS bandpass filter," *Micro Electro Mechanical Systems, 2003. MEMS-03 Kyoto. IEEE The Sixteenth Annual International Conference on* , vol., no., pp. 702- 705, 19-23 Jan. 2003

[70] S. Pourkamali and F. Ayazi, "Electrically coupled MEMS bandpass filters-Part I: with coupling element," *Journal of Sensors and Actuators A* 122, 2005, pp.307-316.

[71] W. D. Beaver , "Analysis of Elastically Coupled Piezoelectric Resonators", *J. Acoust. Soc. Am.* 43, 972 (1968)

[72] Lakin, K.M.; , "Fundamental properties of thin film resonators," *Frequency Control, 1991., Proceedings of the 45th Annual Symposium on* , vol., no., pp.201-206, 29-31 May 1991

[73] *TriQuint Product IF Filters (2011). Retrieved* June 17, 2012.from: www.triquint.com/products/types/filters/if/ Part Number 855271

[74] *TriQuint Product IF Filters (2011). Retrieved* June 17, 2012.from: www.triquint.com/products/types/filters/if/ Part Number 855985

[75] *TriQuint Product IF Filters (2011). Retrieved* June 17, 2012.from: www.triquint.com/products/types/filters/if/ Part Number 856447

[76] Sheng-Shian Li; Yu-Wei Lin; Zeying Ren; Nguyen, C.T.-C.; , "An MSI Micromechanical Differential Disk-Array Filter," *Solid-State Sensors, Actuators and Microsystems Conference, 2007. TRANSDUCERS 2007. International* , pp.307-311, 10-14 June 2007

[77] Stefanou, S.; Hamel, J.S.; Baine, P.; Bain, M.; Armstrong, B.M.; Gamble, H.S.; Kraft, M.; Kemhadjian, H.A.; , "Ultralow silicon substrate noise crosstalk using metal Faraday cages in an SOI technology," *Electron Devices, IEEE Transactions on* , vol.51, no.3, pp. 486- 491, March 2004

[78] Kyuchul Chong; Xi Zhang; King-Ning Tu; Daquan Huang; Mau-Chung Chang; Ya-Hong Xie; , "Three-dimensional substrate impedance engineering based on p^-/p^+ Si substrate for mixed-signal system-on-chip (SoC)," *Electron Devices, IEEE Transactions on* , vol.52, no.11, pp. 2440- 2446, Nov. 2005

[79] "Theory of Intermodulation Distortion Measurement", *Application Note 5C-043*, Maury Microwave Corporation, July 1999, retrieved April 4, 2012, from: http://www.maurymw.com/support/pdfs/5C-043.pdf

[80] Y. Satoh, O. Kate, T. Miyashita, and H. Ohmori, "RF SAW Filters," *International Symposium on Acoustic Wave Devices for Future Mobile Communication Systems*, pp. 125-132, Chiba, Japan, 2001.

[81] Zuo, C., "Aluminum nitride MEMs and CMOS IC co-design for multi-frequency reconfigurable wireless communications". Ph.D. diss., University of Pennsylvania ,2010

[82] R. Navid, J. R. Clark, M. Demirci, and C. T.-C. Nguyen, "Third-Order Intermodulation Distortion in Capacitively-Driven CC-Beam Micromechanical Resonators," 14*th IEEE International Conference on Micro Electro Mechanical Systems (MEMS 2001)*, pp. 228-231, Interlaken, Switzerland, 2001.

[83] Alastalo, A.T.; Kaajakari, V.; , "Intermodulation in capacitively coupled microelectromechanical filters," *Electron Device Letters, IEEE* , vol.26, no.5, pp. 289- 291, May 2005

[84] Lin, Yu-wei, Sheng-shian Li, Zeying Ren, and Clark T Nguyen. 2005. "Third-order intermodulation distortion in capacitively-driven VHF micromechanical resonators". *IEEE Ultrasonics Symposium 2005*, no. 2: 1592-1595.

[85] Zuo, C.,"Aluminum nitride MEMs and CMOS IC co-design for multi-frequency reconfigurable wireless communications". Ph.D. diss., University of Pennsylvania ,2010

[86] Xiangwei Zhu; Yuanling Li; Shaowei Yong; Zhaowen Zhuang; , "A Novel Definition and Measurement Method of Group Delay and Its Application," *Instrumentation and Measurement, IEEE Transactions on* , vol.58, no.1, pp.229-233, Jan. 2009

[87] "Agilent PNA Microwave Network Analyzers", *Application Note 1408-2*, Agilent technologies, January 28, 2004, retrieved June 4, 2012, from: http://cp.literature.agilent.com/litweb/pdf/5988-9619EN.pdf

[88] Kranac,R. "Linear Distortion, Part 1" Communications technology", July 2005

[89] https://www.mems-exchange.org/MEMS/what-is.html

[90] Sheng-Shian Li; Yu-Wei Lin; Yuan Xie; Zeying Ren; Nguyen, C.T.-C.; , "Micromechanical "hollow-disk" ring resonators," *Micro Electro Mechanical Systems, 2004. 17th IEEE International Conference on. (MEMS)* , pp. 821- 824, 2004

[91] Ruby, R.; , "A decade of FBAR success and what is needed for another successful decade," *Piezoelectricity, Acoustic Waves and Device Applications (SPAWDA), 2011 Symposium on* , pp.365-369, 9-11 Dec. 201

Appendices

Appendix A: Permissions

Copyright Clearance Center RightsLink®

Home | Account Info | Help

IEEE Requesting permission to reuse content from an IEEE publication

Title:	Micromechanical mixer-filters ('mixlers')
Author:	Ark-Chew Wong; Nguyen, C.T.-C.
Publication:	Microelectromechanical Systems, IEEE/ASME Journal of
Publisher:	IEEE
Date:	Feb. 2004

Copyright © 2004, IEEE

Logged in as:
Julio Dewdney
Account #:
3000566713
LOGOUT

Thesis / Dissertation Reuse

The IEEE does not require individuals working on a thesis to obtain a formal reuse license, however, you may print out this statement to be used as a permission grant:

Requirements to be followed when using any portion (e.g., figure, graph, table, or textual material) of an IEEE copyrighted paper in a thesis:

1) In the case of textual material (e.g., using short quotes or referring to the work within these papers) users must give full credit to the original source (author, paper, publication) followed by the IEEE copyright line © 2011 IEEE.
2) In the case of illustrations or tabular material, we require that the copyright line © [Year of original publication] IEEE appear prominently with each reprinted figure and/or table.
3) If a substantial portion of the original paper is to be used, and if you are not the senior author, also obtain the senior author's approval.

Requirements to be followed when using an entire IEEE copyrighted paper in a thesis:

1) The following IEEE copyright/ credit notice should be placed prominently in the references: © [year of original publication] IEEE. Reprinted, with permission, from [author names, paper title, IEEE publication title, and month/year of publication]
2) Only the accepted version of an IEEE copyrighted paper can be used when posting the paper o your thesis on-line.
3) In placing the thesis on the author's university website, please display the following message ir a prominent place on the website: In reference to IEEE copyrighted material which is used with permission in this thesis, the IEEE does not endorse any of [university/educational entity's name goes here]'s products or services. Internal or personal use of this material is permitted. If interested in reprinting/republishing IEEE copyrighted material for advertising or promotional purposes or for creating new collective works for resale or redistribution, please go to http://www.ieee.org/publications_standards/publications/rights/rights_link.html to learn how to obtain a License from RightsLink.

If applicable, University Microfilms and/or ProQuest Library, or the Archives of Canada may supply single copies of the dissertation.

Appendix A (Continued)

Thesis / Dissertation Reuse

The IEEE does not require individuals working on a thesis to obtain a formal reuse license, however, you may print out this statement to be used as a permission grant:

Requirements to be followed when using any portion (e.g., figure, graph, table, or textual material) of an IEEE copyrighted paper in a thesis:

1) In the case of textual material (e.g., using short quotes or referring to the work within these papers) users must give full credit to the original source (author, paper, publication) followed by the IEEE copyright line © 2011 IEEE.
2) In the case of illustrations or tabular material, we require that the copyright line © [Year of original publication] IEEE appear prominently with each reprinted figure and/or table.
3) If a substantial portion of the original paper is to be used, and if you are not the senior author, also obtain the senior author's approval.

Requirements to be followed when using an entire IEEE copyrighted paper in a thesis:

1) The following IEEE copyright/ credit notice should be placed prominently in the references: © [year of original publication] IEEE. Reprinted, with permission, from [author names, paper title, IEEE publication title, and month/year of publication]
2) Only the accepted version of an IEEE copyrighted paper can be used when posting the paper or your thesis on-line.
3) In placing the thesis on the author's university website, please display the following message in a prominent place on the website: In reference to IEEE copyrighted material which is used with permission in this thesis, the IEEE does not endorse any of [university/educational entity's name goes here]'s products or services. Internal or personal use of this material is permitted. If interested in reprinting/republishing IEEE copyrighted material for advertising or promotional purposes or for creating new collective works for resale or redistribution, please go to http://www.ieee.org/publications_standards/publications/rights/rights_link.html to learn how to obtain a License from RightsLink.

If applicable, University Microfilms and/or ProQuest Library, or the Archives of Canada may supply single copies of the dissertation.

Appendix A (Continued)

Copyright Clearance Center RightsLink®

Home | Account Info | Help

IEEE Requesting permission to reuse content from an IEEE publication

Title:	1.156-GHz self-aligned vibrating micromechanical disk resonator
Author:	Jing Wang; Ren, Z.; Nguyen, C.T.-C.
Publication:	Ultrasonics, Ferroelectrics and Frequency Control, IEEE Transactions on
Publisher:	IEEE
Date:	Dec. 2004

Copyright © 2004, IEEE

Logged in as:
Julio Dewdney
Account #:
3000566713
LOGOUT

Thesis / Dissertation Reuse

The IEEE does not require individuals working on a thesis to obtain a formal reuse license, however, you may print out this statement to be used as a permission grant:

Requirements to be followed when using any portion (e.g., figure, graph, table, or textual material) of an IEEE copyrighted paper in a thesis:

1) In the case of textual material (e.g., using short quotes or referring to the work within these papers) users must give full credit to the original source (author, paper, publication) followed by the IEEE copyright line © 2011 IEEE.
2) In the case of illustrations or tabular material, we require that the copyright line © [Year of original publication] IEEE appear prominently with each reprinted figure and/or table.
3) If a substantial portion of the original paper is to be used, and if you are not the senior author, also obtain the senior author's approval.

Requirements to be followed when using an entire IEEE copyrighted paper in a thesis:

1) The following IEEE copyright/ credit notice should be placed prominently in the references: © [year of original publication] IEEE. Reprinted, with permission, from [author names, paper title, IEEE publication title, and month/year of publication]
2) Only the accepted version of an IEEE copyrighted paper can be used when posting the paper or your thesis on-line.
3) In placing the thesis on the author's university website, please display the following message in a prominent place on the website: In reference to IEEE copyrighted material which is used with permission in this thesis, the IEEE does not endorse any of [university/educational entity's name goes here]'s products or services. Internal or personal use of this material is permitted. If interested in reprinting/republishing IEEE copyrighted material for advertising or promotional purposes or for creating new collective works for resale or redistribution, please go to http://www.ieee.org/publications_standards/publications/rights/rights_link.html to learn how to obtain a License from RightsLink.

If applicable, University Microfilms and/or ProQuest Library, or the Archives of Canada may supply single copies of the dissertation.

Appendix A (Continued)

RightsLink®

Home | Account Info | Help

Title: Internal Dielectric Transduction in Bulk-Mode Resonators
Author: Weinstein, D.; Bhave, S.A.
Publication: Microelectromechanical Systems, IEEE/ASME Journal of
Publisher: IEEE
Date: Dec. 2009

Logged in as:
Julio Dewdney
Account #:
3000566713
LOGOUT

Thesis / Dissertation Reuse

The IEEE does not require individuals working on a thesis to obtain a formal reuse license, however, you may print out this statement to be used as a permission grant:

Requirements to be followed when using any portion (e.g., figure, graph, table, or textual material) of an IEEE copyrighted paper in a thesis:

1) In the case of textual material (e.g., using short quotes or referring to the work within these papers) users must give full credit to the original source (author, paper, publication) followed by the IEEE copyright line © 2011 IEEE.
2) In the case of illustrations or tabular material, we require that the copyright line © [Year of original publication] IEEE appear prominently with each reprinted figure and/or table.
3) If a substantial portion of the original paper is to be used, and if you are not the senior author, also obtain the senior author's approval.

Requirements to be followed when using an entire IEEE copyrighted paper in a thesis:

1) The following IEEE copyright/ credit notice should be placed prominently in the references: © [year of original publication] IEEE. Reprinted, with permission, from [author names, paper title, IEEE publication title, and month/year of publication]
2) Only the accepted version of an IEEE copyrighted paper can be used when posting the paper or your thesis on-line.
3) In placing the thesis on the author's university website, please display the following message in a prominent place on the website: In reference to IEEE copyrighted material which is used with permission in this thesis, the IEEE does not endorse any of [university/educational entity's name goes here]'s products or services. Internal or personal use of this material is permitted. If interested in reprinting/republishing IEEE copyrighted material for advertising or promotional purposes or for creating new collective works for resale or redistribution, please go to http://www.ieee.org/publications_standards/publications/rights/rights_link.html to learn how to obtain a License from RightsLink.

If applicable, University Microfilms and/or ProQuest Library, or the Archives of Canada may supply single copies of the dissertation.

Appendix A (Continued)

Copyright Clearance Center RightsLink®

Home | Account Info | Help

IEEE Requesting permission to reuse content from an IEEE publication

Title: Single-Chip Multiple-Frequency ALN MEMS Filters Based on Contour-Mode Piezoelectric Resonators

Author: Piazza, G.; Stephanou, P.J.; Pisano, A.P.

Publication: Microelectromechanical Systems, IEEE/ASME Journal of

Publisher: IEEE

Date: April 2007

Copyright © 2007, IEEE

Logged in as:
Julio Dewdney
Account #:
3000566713

LOGOUT

Thesis / Dissertation Reuse

The IEEE does not require individuals working on a thesis to obtain a formal reuse license, however, you may print out this statement to be used as a permission grant:

Requirements to be followed when using any portion (e.g., figure, graph, table, or textual material) of an IEEE copyrighted paper in a thesis:

1) In the case of textual material (e.g., using short quotes or referring to the work within these papers) users must give full credit to the original source (author, paper, publication) followed by the IEEE copyright line © 2011 IEEE.
2) In the case of illustrations or tabular material, we require that the copyright line © [Year of original publication] IEEE appear prominently with each reprinted figure and/or table.
3) If a substantial portion of the original paper is to be used, and if you are not the senior author, also obtain the senior author's approval.

Requirements to be followed when using an entire IEEE copyrighted paper in a thesis:

1) The following IEEE copyright/ credit notice should be placed prominently in the references: © [year of original publication] IEEE. Reprinted, with permission, from [author names, paper title, IEEE publication title, and month/year of publication]
2) Only the accepted version of an IEEE copyrighted paper can be used when posting the paper or your thesis on-line.
3) In placing the thesis on the author's university website, please display the following message in a prominent place on the website: In reference to IEEE copyrighted material which is used with permission in this thesis, the IEEE does not endorse any of [university/educational entity's name goes here]'s products or services. Internal or personal use of this material is permitted. If interested in reprinting/republishing IEEE copyrighted material for advertising or promotional purposes or for creating new collective works for resale or redistribution, please go to http://www.ieee.org/publications_standards/publications/rights/rights_link.html to learn how to obtain a License from RightsLink.

If applicable, University Microfilms and/or ProQuest Library, or the Archives of Canada may supply single copies of the dissertation.

Appendix A (Continued)

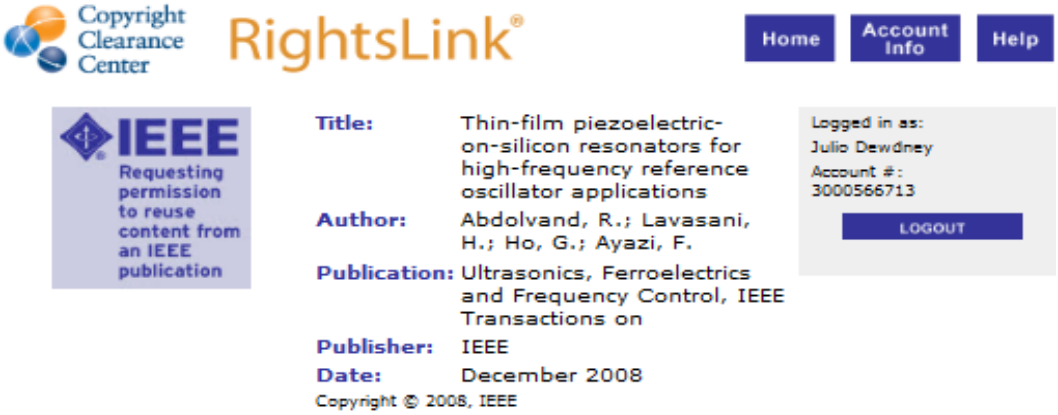

Copyright Clearance Center RightsLink®

Home | Account Info | Help

IEEE Requesting permission to reuse content from an IEEE publication

Title: Thin-film piezoelectric-on-silicon resonators for high-frequency reference oscillator applications

Author: Abdolvand, R.; Lavasani, H.; Ho, G.; Ayazi, F.

Publication: Ultrasonics, Ferroelectrics and Frequency Control, IEEE Transactions on

Publisher: IEEE

Date: December 2008

Copyright © 2008, IEEE

Logged in as: Julio Dewdney
Account #: 3000566713
LOGOUT

Thesis / Dissertation Reuse

The IEEE does not require individuals working on a thesis to obtain a formal reuse license, however, you may print out this statement to be used as a permission grant:

Requirements to be followed when using any portion (e.g., figure, graph, table, or textual material) of an IEEE copyrighted paper in a thesis:

1) In the case of textual material (e.g., using short quotes or referring to the work within these papers) users must give full credit to the original source (author, paper, publication) followed by the IEEE copyright line © 2011 IEEE.
2) In the case of illustrations or tabular material, we require that the copyright line © [Year of original publication] IEEE appear prominently with each reprinted figure and/or table.
3) If a substantial portion of the original paper is to be used, and if you are not the senior author, also obtain the senior author's approval.

Requirements to be followed when using an entire IEEE copyrighted paper in a thesis:

1) The following IEEE copyright/ credit notice should be placed prominently in the references: © [year of original publication] IEEE. Reprinted, with permission, from [author names, paper title, IEEE publication title, and month/year of publication]
2) Only the accepted version of an IEEE copyrighted paper can be used when posting the paper or your thesis on-line.
3) In placing the thesis on the author's university website, please display the following message in a prominent place on the website: In reference to IEEE copyrighted material which is used with permission in this thesis, the IEEE does not endorse any of [university/educational entity's name goes here]'s products or services. Internal or personal use of this material is permitted. If interested in reprinting/republishing IEEE copyrighted material for advertising or promotional purposes or for creating new collective works for resale or redistribution, please go to http://www.ieee.org/publications_standards/publications/rights/rights_link.html to learn how to obtain a License from RightsLink.

If applicable, University Microfilms and/or ProQuest Library, or the Archives of Canada may supply single copies of the dissertation.

Appendix A (Continued)

Copyright Clearance Center RightsLink®

Home | Account Info | Help

IEEE Requesting permission to reuse content from an IEEE publication

Title:	A 600 kHz electrically-coupled MEMS bandpass filter
Conference Proceedings:	Micro Electro Mechanical Systems, 2003. MEMS-03 Kyoto. IEEE The Sixteenth Annual International Conference on
Author:	Pourkamali, S.; Abdolvand, R.; Ayazi, F.
Publisher:	IEEE
Date:	19-23 Jan. 2003

Copyright © 2003, IEEE

Logged in as:
Julio Dewdney
Account #:
3000566713
LOGOUT

Thesis / Dissertation Reuse

The IEEE does not require individuals working on a thesis to obtain a formal reuse license, however, you may print out this statement to be used as a permission grant:

Requirements to be followed when using any portion (e.g., figure, graph, table, or textual material) of an IEEE copyrighted paper in a thesis:

1) In the case of textual material (e.g., using short quotes or referring to the work within these papers) users must give full credit to the original source (author, paper, publication) followed by the IEEE copyright line © 2011 IEEE.
2) In the case of illustrations or tabular material, we require that the copyright line © [Year of original publication] IEEE appear prominently with each reprinted figure and/or table.
3) If a substantial portion of the original paper is to be used, and if you are not the senior author, also obtain the senior author's approval.

Requirements to be followed when using an entire IEEE copyrighted paper in a thesis:

1) The following IEEE copyright/ credit notice should be placed prominently in the references: © [year of original publication] IEEE. Reprinted, with permission, from [author names, paper title, IEEE publication title, and month/year of publication]
2) Only the accepted version of an IEEE copyrighted paper can be used when posting the paper or your thesis on-line.
3) In placing the thesis on the author's university website, please display the following message in a prominent place on the website: In reference to IEEE copyrighted material which is used with permission in this thesis, the IEEE does not endorse any of [university/educational entity's name goes here]'s products or services. Internal or personal use of this material is permitted. If interested in reprinting/republishing IEEE copyrighted material for advertising or promotional purposes or for creating new collective works for resale or redistribution, please go to http://www.ieee.org/publications_standards/publications/rights/rights_link.html to learn how to obtain a License from RightsLink.

If applicable, University Microfilms and/or ProQuest Library, or the Archives of Canada may supply single copies of the dissertation.

Appendix B: Detailed Fabrication Process for ZnO Resonators and Filters

A. Sample Cleaning

A.1. Label(scribe) the back of all sampled with series and sample number
A.2. RCA clean
A.3. Solvent clean

B. Bottom Electrode (Mask 1)

B.1. Lithography 3000PY - NR9
Spin: Laurell Spinner
3000PY - NR9: 40 sec @ 3000 RPM
Softbake: 1 min @ 150°C
Exposure: 18 sec @ 20 mW/cm^2, hard contact
Hardbake: 1 min @ 100°C
Develop: 17 sec in RD6

B.2. Descum
Equipment: Plasma Therm
O_2: 50 sccm
Pressure: 300 mTorr
Power: 100 watts
Time: 1 min

B.3. Titanium Deposition
Equipment: AJA Sputtering
Power: 100 watts RF
Pressure: 5 mTorr
Flow rate: Ar 12 sccm
Time: 16 min (~30 nm)

B.4. Platinum Deposition
Equipment: AJA Sputtering
Power: 100 watts DC
Pressure: 5 mTorr
Flow rate: Ar 12 sccm
Time: 11 min (~125 nm)

B.5. Lift-off
Submerge wafer in acetone overnight
Sonication if is needed
Solvent clean
Descum

Appendix B (Continued)

C. ZnO Deposition
Equipment: AJA Sputtering
Power: 100 watts RF
O_2: Ar 6:6 sccm
Pressure: 5 mTorr
Temperature: 300˚C
Time: 256 min (500 nm)
Annealing: 300˚C for 30 min

D. Open Vias Bottom Electrode (Mask 2)

D.1. Lithography S1813 ~1.3 µm
Equipment: Laura Spinner
Spin: Laurell Spinner
HMDS: 10 sec @ 700 RPM
1813: 30 sec @ 4000 RPM
Softbake time: 1 min @ 115°C
Exposure time: 4 sec @ 25 mW
Develop time: 70 sec in MF319
Descum

D.2. ZnO Wet Etch
Solution: 1: 200 HCl: H_2O
Submerge wafer in solution for 50 sec
Rinse wafer with water and dry
Submerge wafer in acetone for 1 hr
Solvent clean

E. Top Electrode (Mask 3)

E.1. Lithography 3000PY-NR9
Spin: Laurell Spinner
3000PY-NR9: 40 sec @ 3000 RPM
Softbake: 1 min @ 150°C
Exposure: 11 sec @ 20 mW/cm^2, hard contact
Hardbake: 1 min @ 100°C
Develop: 17 sec in RD6
Descum

Appendix B (Continued)

E.2. Titanium Deposition
Equipment: AJA Sputtering
Power: 100 watts RF
Pressure: 5 mTorr
Flow rate: Ar 6 sccm
Time: 16 min (~30 nm)

E.3. Platinum Deposition
Equipment: AJA Sputtering
Power: 100 watts DC
Pressure: 5 mTorr
Flow rate: Ar 6 sccm
Time: 11 min (~125 nm)

E.4. Lift-off
Submerge sample in acetone overnight
Sonication if is needed
Solvent clean
Descum

F. Gold Pads Contact (Mask 4)

F.1. Lithography 3000PY-NR9
Spin: Laurell Spinner
3000PY-NR9: 40 sec @ 3000 RPM
Softbake: 1 min @ 150°C
Exposure: 11 sec @ 20 mW/cm^2, hard contact
Hardbake: 1 min @ 100°C
Develop: 17 sec in RD6
Descum

F.2. Chrome Deposition
Equipment: Thermal Evaporator
Thickness: 30 nm

F.3. Gold Deposition
Equipment: Thermal Evaporator
Thickness: 600 nm

F.4. Lift-off
Submerge sample in acetone overnight
Solvent clean
Descum

Appendix B (Continued)

G. Pattern Resonator Body Structure (Mask 5)

G.1. Lithography 1827 ~2.7 µm
Spin: Laurell Spinner
HMDS: 10 sec @ 700 RPM
1827: 30 sec @ 3500 RPM
Softbake: 1 min @ 115°C
Exposure: 14 sec @ 25 mW/cm^2, hard contact
Develop: 3 min in MF319
Descum

G.2. ZnO DRIE
Equipment: AMS 100, Alcatel Vacuum Technology, France
CH_4/Ar
Ar: 16 sccm
CH: 32 sccm
Power: 1800 watts
Substrate temperature: -20 °C
Time: 10 min
Etch rate: ~0.5 um/min

H. Dry Release

H.1. SF_6 Release
Equipment: AMS 100, Alcatel Vacuum Technology, France
SF_6: 300 sccm
ICP Power: 1500 watts
Substrate temperature: 25 °C
Chamber pressure: 40 mTorr
Etch rate: ~5 µm/min

H.2. Photoresist Ashing
Equipment: Plasma Therm
O_2: 50 sccm
Pressure: 300 mTorr
Power: 100 watts
Time: 30 min

Appendix C: Detailed Fabrication Process for ZnO-on-SOI Resonators and Filters

A. Sample Cleaning
   A.1. Label(scribe) the back of all sampled with series and sample number
   A.2. RCA clean
   A.3. Solvent clean

B. Pre-release Holes (Mask 1)

   B.1. Lithography S1827 ~2.7 µm
      Equipment: Laura Spinner
      Spin: Laurell Spinner
         HMDS: 10 sec @ 700 RPM
         1827: 30 sec @ 3500 RPM
      Softbake time: 1 min @ 115°C
      Exposure time: 14 sec @ 25 mW, hard contact
      Develop time: 3 min in MF319
      Descum

   B.2. Si DRIE
      Equipment: AMS 100, Alcatel Vacuum Technology, France
      SF_6: 300 sccm, 3 sec
      C_4F_8: 200 sccm; O2: 20 sccm, 1.4 sec
      Power: 1800 watts
      Pulsed power: 25 ms @ 100 watts; 75 ms @ 0 watts
      Substrate temperature: -15 °C
      Etch rate: ~7 um/min

   B.3. SiO_2 Wet Etch
      Strip photoresist
      Solution: concentrated HF 49% + 3 drops of TritonX
      Submerge wafer in solution for 70 min
      Submerge wafer in methanol for 10 min
      Submerge wafer in isopropanol for 10 min
      Bake wafer in oven for 15 min at 110˚C
      Solvent clean

Appendix C (Continued)

C. Bottom Electrode (Mask 2)

C.1. Lithography 3000PY - NR9
Spin: Laurell Spinner
3000PY - NR9: 40 sec @ 3000 RPM
Softbake: 1 min @ 150°C
Exposure: 18 sec @ 20 mW/cm^2, hard contact
Hardbake: 1 min @ 100°C
Develop: 17 sec in RD6

C.2. Descum
Equipment: Plasma Therm
O_2: 50 sccm
Pressure: 300 mTorr
Power: 100 watts
Time: 1 min

C.3. Titanium Deposition
Equipment: AJA Sputtering
Power: 100 watts RF
Pressure: 5 mTorr
Flow rate: Ar 6 sccm
Time: 16 min (~30 nm)

C.4. Platinum Deposition
Equipment: AJA Sputtering
Power: 100 watts DC
Pressure: 5 mTorr
Flow rate: Ar 6 sccm
Time: 11 min (~125 nm)

C.5. Lift-off
Submerge sample in acetone overnight
Sonication if is needed
Solvent clean
Descum

Appendix C (Continued)

D. ZnO Deposition
Equipment: AJA Sputtering
Power: 100 watts RF
O_2:Ar 6:6 sccm
Pressure: 5 mTorr
Temperature: 300˚C
Time: 256 min (500 nm)
Annealing: 300˚C for 30 min

E. Open Vias Bottom Electrode (Mask #)

E.1. Lithography S1813 ~1.3 µm
Equipment: Laura Spinner
Spin: Laurell Spinner
HMDS: 10 sec @ 700 RPM
1813: 30 sec @ 4000 RPM
Softbake time: 1 min @ 115°C
Exposure time: 4 sec @ 25 mW, hard contact
Develop time: 70 sec in MF319
Descum

E.2. ZnO Wet Etch
Solution: 1: 200 HCl: H_2O
Submerge wafer in solution for 50 sec
Rinse wafer with water and dry
Submerge wafer in acetone for 1 hr
Solvent clean

F. Top Electrode (Mask 4)

F.1. Lithography 3000PY-NR9
Spin: Laurell Spinner
3000PY-NR9: 40 sec @ 3000 RPM
Softbake: 1 min @ 150°C
Exposure: 11 sec @ 20 mW/cm^2, hard contact
Hardbake: 1 min @ 100°C
Develop: 17 sec in RD6
Descum

Appendix C (Continued)

F.2. Titanium Deposition
Equipment: AJA Sputtering
Power: 100 watts RF
Time: 16 min (~30 nm)

F.3. Platinum Deposition
Equipment: AJA Sputtering
Power: 100 watts DC
Time: 11 min (~125 nm)

F.4. Lift-off
Submerge wafer in acetone overnight
Sonication if is needed
Solvent clean
Descum

G. Gold Pads Contact (Mask 5)

G.1. Lithography 3000PY-NR9
Spin: Laurell Spinner
3000PY-NR9: 40 sec @ 3000 RPM
Softbake: 1 min @ 150°C
Exposure: 11 sec @ 20 mW/cm^2, hard contact
Hardbake: 1 min @ 100°C
Develop: 17 sec in RD6
Descum

G.2. Chrome Deposition
Equipment: Thermal Evaporator
Thickness: 30 nm

G.3. Gold Deposition
Equipment: Thermal Evaporator
Thickness: 600 nm

G.4. Lift-off
Submerge sample in acetone overnight
Solvent clean
Descum

Appendix C (Continued)

H. Pattern Resonator Body Structure (Mask 6)

H.1. Lithography 1827 ~2.7 µm
Spin: Laurell Spinner
HMDS: 10 sec @ 700 RPM
1827: 30 sec @ 3500 RPM
Softbake: 1 min @ 115°C
Exposure: 14 sec @ 25 mW/cm^2, hard contact
Develop: 3 min in MF319
Descum

H.2. ZnO DRIE
Equipment: AMS 100, Alcatel Vacuum Technology, France
CH_4/Ar
Ar: 16 sccm
CH: 32 sccm
Power: 1800 watts
Substrate temperature: -20 °C
Time: 10 min
Etch rate: ~0.5 um/min

H.3. Si DRIE
Equipment: AMS 100, Alcatel Vacuum Technology, France
SF_6: 300 sccm, 3 sec
C_4F_8: 200 sccm; O2: 20 sccm, 1.4 sec
Power: 1800 watts
Pulsed power: 25 ms @ 100 watts; 75 ms @ 0 watts
Substrate temperature: -15 °C
Etch rate: ~7 um/min

H.4. Photoresist Ashing
Equipment: Plasma Therm
O_2: 50 sccm
Pressure: 300 mTorr
Power: 100 watts
Time: 30 min

About the Author

Julio Mario Dewdney Montero received his B.S. degree (Honors) from Universidad del Norte (University of North), Barranquilla, Colombia, in 2004; his M.S. degree in electrical engineering from the University of South Florida, Tampa, in 2009, and is currently working towards his Ph.D. degree in electrical engineering at the University of South Florida. He is currently with the RF-MEMS Transducers Group (a division of the WAMI Center), Electrical Engineering Department, and University of South Florida. His areas of research are RF and MEMS. His current research involves the design, fabrication and measurement of piezoelectrically transduced MEMS resonators and filter for wireless communications.